Stress Wave Source Characterization: Impact, Fracture, and Sliding Friction

by

Gregory Christofer McLaskey

A dissertation submitted in partial satisfaction of the

requirements for the degree of

Doctor of Philosophy

in

Engineering - Civil and Environmental Engineering

in the

Graduate Division

of the

University of California, Berkeley

Committee in charge:

Professor Steven D. Glaser, Chair
Professor James W. Rector III
Professor Douglas S. Dreger

Spring 2011

Abstract

Stress Wave Source Characterization: Impact, Fracture, and Sliding Friction

by

Gregory Christofer McLaskey

Doctor of Philosophy in Civil and Environmental Engineering

University of California, Berkeley

Professor Steven D. Glaser, Chair

Rapidly varying forces, such as those associated with impact, rapid crack propagation, and fault rupture, are sources of stress waves which propagate through a solid body. This dissertation investigates how properties of a stress wave source can be identified or constrained using measurements recorded at an array of sensor sites located far from the source. This methodology is often called the method of acoustic emission and is useful for structural health monitoring and the noninvasive study of material behavior such as friction and fracture. In this dissertation, laboratory measurements of 1-300 mm wavelength stress waves are obtained by means of piezoelectric sensors which detect high frequency (10 kHz- 3MHz) motions of a specimen's surface, picometers to nanometers in amplitude. Then, stress wave source characterization techniques are used to study ball impact, drying shrinkage cracking in concrete, and the micromechanics of stick-slip friction of Poly(methyl methacrylate) (PMMA) and rock/rock interfaces.

In order to quantitatively relate recorded signals obtained with an array of sensors to a particular stress wave source, wave propagation effects and sensor distortions must be accounted for. This is achieved by modeling the physics of wave propagation and transduction as linear transfer functions. Wave propagation effects are precisely modeled by an elastodynamic Green's function, sensor distortion is characterized by an instrument response function, and the stress wave source is represented with a force moment tensor. These transfer function models are verified though calibration experiments which employ two different mechanical calibration sources: ball impact and glass capillary fracture. The suitability of the ball impact source model, based on Hertzian contact theory, is experimentally validated for small (~1 mm) balls impacting massive plates composed of four different materials: aluminum, steel, glass, and PMMA.

Using this transfer function approach and the two mechanical calibration sources, four types of piezoelectric sensors were calibrated: three commercially available sensors and the Glaser-type conical piezoelectric sensor, which was developed in the Glaser laboratory. The distorting effects of each sensor are modeled using autoregressive-moving average (ARMA) models, and because vital phase information is robustly incorporated into these models, they are useful for simulating or removing sensor-induced distortions, so that a displacement time history can be retrieved from recorded signals. The Glaser-type sensor was found to be very well modeled as a unidirectional displacement sensor which detects stress wave disturbances down to about 1 picometer in amplitude.

Finally, the merits of a fully calibrated experimental system are demonstrated in a study of stress wave sources arising from sliding friction, and the relationship between those sources and earthquakes. A laboratory friction apparatus was built for this work which allows the micro-mechanisms of friction to be studied with stress wave analysis. Using an array of 14 Glaser-type sensors, and precise models of wave propagation effects and the sensor distortions, the physical origins of the stress wave sources are explored. Force-time functions and focal mechanisms are determined for discrete events found amid the "noise" of friction. These localized events are interpreted to be the rupture of micrometer-sized contacts, known as asperities. By comparing stress wave sources from stick-slip experiments on plastic/plastic and rock/rock interfaces, systematic differences were found. The rock interface produces very rapid (<1 microsecond) implosive forces indicative of brittle asperity failure and fault gouge formation, while rupture on the plastic interface releases only shear force and produces a source more similar to earthquakes commonly recorded in the field. The difference between the mechanisms is attributed to the vast differences in the hardness and melting temperatures of the two materials, which affect the distribution of asperities as well as their failure behavior. With proper scaling, the strong link between material properties and laboratory earthquakes will aid in our understanding of fault mechanics and the generation of earthquakes and seismic tremor.

Table of Contents

Acknowledgements

I would like to thank Professor Steven Glaser for freedom, criticism, and an outstanding laboratory for experimental research. Special thanks to Christian Grosse for showing me the ropes of the Glaser lab and lots of encouragement along the way, Roland Burgman for opening the doors to his active tectonics group, and Lane Johnson for many insightful discussions. Thanks to Albert To, who built the sensors that made the initial experiments possible. Also thanks to Paulo Monteiro, Boza Stojadinovic, James Rector, Doug Dreger, Brian Bonner, Larry Hutchings, Mario Maglioco, and Branko Kerkez, and Yassi Hafezi.

Financial assistance has been provided in part by National Science Foundation grant CMS-0624985 and the National Science Foundation Graduate Fellowship program.

This thesis is dedicated to the five people in my life so far who have been major contributors to my intellectual and academic success. The principle attribute that these five people share is a tremendous faith in my capabilities and potential. Because these five expected great things from me, my own standards were raised. The first two are my parents, to whom I am forever grateful for giving me encouragement, opportunity, and discipline, without imposing too many preconceived plans for my likes, dislikes, and future directions. The third is my fifth grade teacher, Cathy Bordi. Cathy had a seemingly blind and unconditional faith--a faith that I am somehow special and am destined to do great things. I think that this has been a motivating and reassuring force in my life. The fourth is my undergraduate advisor at Cornell University: Mary Sansalone. Mary was my fairy godmother. She took me under her wing and introduced me to research. Her guidance sent me to graduate school, and helped me obtain an NSF graduate fellowship. The last is my graduate advisor: Steve Glaser. Steve has given me the opportunity and the freedom to explore and to achieve.

Chapter 1

Introduction

1.1 Context and goals

This dissertation investigates a branch of mechanics known as elastodynamics. It describes the analysis of solid bodies subjected to specific, localized, and rapidly varying forces or stresses such as those associated with impact, explosions, rapid crack propagation, and fault rupture. These rapidly varying forces are the source of transient elastic waves which propagate outward from the location of the source. While these waves have been given many different names in different contexts, including stress waves, seismic waves, elastic waves, sound waves, acoustic emission, etc., in this dissertation, they are referred to as stress waves.

The basic laws of rigid-body Newtonian dynamics (f=ma), that students learn in introductory physics classes work well for problems such as a bat hitting a ball or thrust applied to a rocket. These are cases in which forces act on solid bodies over time durations which are long compared to the time it takes for sound waves to traverse the body. This dissertation addresses a class of problems where applied forces are varied so rapidly that the dynamics cannot be accurately accounted for by considering only the general motion or even the vibrational or resonant behavior (eigenmodes) of the solid body. To solve problems of this nature, the full theory of wave propagation in a 3D solid elastic body must be considered.

The specific aim of this dissertation is to obtain a better understanding of stress wave sources, and how properties of the source can be identified or constrained using measurements of stress waves recorded at an array of sensor sites located far from the source. Problems of this nature exist at many different scales, ranging from global seismic arrays used to study earthquakes to laboratory sensor arrays which span less than a meter. The current work is at the small scale: laboratory measurements of stress waves which excite motions that are picometers to nanometers in amplitude and operate at wavelengths ranging from 1-300 mm. Because of its many similarities to conventional seismology, this work is sometimes referred to as nanoseismology.

The methodology described in this work is a form of noninvasive testing because the remote observation of stress waves does not interfere with the physics of the source. The methods are particularly useful for structural health monitoring and nondestructive testing common to civil and mechanical engineering disciplines. In many other research situations, stress wave analysis is one of the only tools available to better understand complicated physical and mechanical behavior, either because the source occurs at an inaccessible location--such as deep below the surface of the earth--or because the rapid dynamics of the source process precludes most other methods. Three classes of stress wave sources are the topics of study of this thesis: (1) forces produced during the impact of tiny balls onto massive bodies, (2) the rapid reorganization of stress which occurs during the sudden fracture of a material, and (3) the sudden rupture of an interface held together by friction.

In this work, stress waves are observed via signals recorded with piezoelectric sensors. These instruments are sensitive to high frequency motions of a specimen's surface. These motions are caused by stress waves. In order to relate recorded signals obtained with an array of sensors to a particular stress wave source, the problem is cast into a mathematical and conceptual framework which establishes the operating assumptions and mathematical rules used to solve

problems. This dissertation work utilizes a linear transfer function framework, which is consistent with linear systems theory (e.g. Oppenheim and Schafer, 1999). Within this framework, the effects of wave propagation can be characterized by an elastodynamic Green's function, sensor distortion can be characterized by an instrument response function, and the stress wave source is represented with a force moment tensor (Stump and Johnson, 1977).

This chapter introduces the topics and major results of each subsequent chapter and describes how they align with the broader goals of the thesis. A more general introduction and review can be found within each chapter.

1.2 Summary and Glaser-type sensors

Chapter 2 describes the conceptual and mathematical formulation of the transfer function framework. Use of this framework is demonstrated through a sensor calibration study useful for nondestructive testing (NDT) techniques. While the chapter introduces the concepts of stress wave sources, Green's functions, and instrument response in the context of a sensor calibration problem, this methodology is the foundation of the quantitative stress wave analysis techniques which make the results of later chapters possible. In Chapter 2, the stress wave sources and wave propagation effects are precisely modeled so that an unknown sensor response function can be determined. In later chapters, knowledge of the sensor response function is utilized, so that unknown sources can be precisely characterized.

For the purpose of example and case study, Chapter 2 compares the characteristics of four different sensors: three commercially available sensors and the Glaser-type conical piezoelectric sensor, which was developed in the Glaser laboratory. Chapter 2 also demonstrates how a sensor's response function can be simulated or removed from arbitrary signals, so that interpretations of the stress waves are not distorted by the "lens" through which they are observed. For the remainder of the dissertation, an array of the Glaser-type sensors is employed. These displacement sensors are shown to be extremely sensitive and introduce minimal distortion. They detect waves down to a few pm in amplitude in the frequency range of ~8 kHz to over 2 MHz. The sensors are sometimes referred as nanoseismic sensors due their analogous role to that of seismic instruments and the extremely small amplitude and large bandwidth of surface normal displacements they are capable of recording. Their small size (14 mm diameter threaded body, 30 mm long) permits a dense population of sensors to be installed on laboratory-sized samples.

A basic diagram of the Glaser-type sensor design is depicted in Figure 1.1. The base of the truncated conical PZT-5a (lead-zirconium-titanate composition) sensing element is soldered to an irregularly shaped lead backing mass which is potted in a hardened steel canister with polyurethane rubber. The sensor is mounted onto a specimen so that only the truncated tip of the conical piezoelectric element (covered by a thin electrode) is in contact with the specimen. Glaser-type sensors used in Chapters 3 and 4 have a tip diameter of 1.75 mm, while the Glaser-type sensors used in Chapters 2 and 5 have a tip diameter of 0.5 mm. Normal displacements of the surface of the specimen cause the PZT cone to be compressed between the surface of the specimen and the backing mass. This compression (or tension relative to the sensor's preload) causes the PZT element to strain which causes a measurable voltage between the two ends of the cone. This voltage is amplified with a JFET located inside the hardened steel canister to avoid signal loss due to parasitic capacitance.

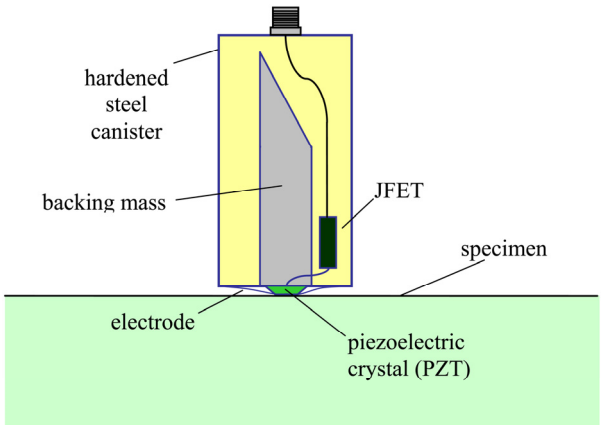

Figure 1.1. A schematic diagram of the sensor design. The active element is a piezoelectric crystal in the shape of a truncated cone which is soldered to a backing mass and potted in a hardened steel can with polyurethane rubber. Normal displacements of the specimen sandwich the piezoelectric crystal between the specimen and the backing mass and produce measurable changes in voltage.

Chapter 3 investigates the stress waves generated by the impact of a small ball onto a massive plate. Because the ball-impact forcing function was used as one of the calibration sources in Chapter 2, a systematic study of ball impact as a source of stress waves is needed. The precise determination of the amplitude and frequency content of stress waves radiated from impact has traditionally relied on equations derived from Hertzian contact theory. But this theory is both purely elastic and quasistatic in nature; it neglects to consider both radiated elastic waves and anelastic effects, such as plasticity and viscoelasticity. Chapter 3 describes the experimental validation of the Hertzian impact model, and the calibration of the Glaser-type sensors on four different target materials: aluminum, steel, glass, and Poly(methyl methacrylate) (PMMA). This chapter describes the experimental methods and analysis techniques used to verify the Reed (1985) correction to Hunter's (1957) theory, and evaluates some of the limits of this theory and how they relate to the physics and mechanics of impact.

By measuring stress waves radiated from impact as well as the approach and rebound velocities of the bouncing ball, both the energy dissipated in the collision and the ball's momentum change during the collision were calculated. This study illustrated very clearly that recorded stress waves are directly proportional to the ball's change in momentum, but show no direct relationship to energy dissipated during impact. This offers a nice parallel to earthquake studies which have found that seismic moment is a source parameter which is readily estimated from recordings of seismic waves, but energy dissipated during an earthquake remains elusive.

Another result to come from Chapter 3 is that the sensitivity of the sensor was found to vary when coupled to different materials. These details are taken into account for the analysis of stress wave sources from friction, in Chapter 5.

Chapter 4 describes how stress wave analysis can be used to study micro cracking in concrete. Concrete is known to attenuate and scatter propagating stress waves, especially at high frequencies. These wave propagation effects complicate the stress wave analysis problem and make the precise characterization of stress wave sources particularly challenging. Consequently, this chapter focuses on the problem of solving for the location of stress wave sources in space and time based on estimates of wave arrivals from an array of sensors. Source location is particularly important because further analysis of source characteristics relies on accurate localization. This chapter describes some of the common sources of error associated with the

source location technique, how errors can be modeled, and the amplification of errors due to array geometry and incorrect velocity models.

Chapter 5 examines stress wave sources arising from sliding friction, and the relationship between those sources and earthquakes. Past studies of friction have shown that "true" contact between two nominally flat surfaces consists of an ensemble of μm-scale contacts known as asperities. This chapter first reviews these types of surface interactions, describes how asperity behavior gives rise to some commonly observed friction laws, and considers some of the methods by which asperity behavior has been studied in the past. By using the Glaser-type sensors and the analysis framework described in Chapter 2, many of the common challenges associated with the study of friction mechanisms are overcome. A special laboratory friction apparatus was built for this work which allows the study of friction micro-mechanisms via stress wave analysis. The apparatus accommodates large plate specimens in which the wave propagation can be readily characterized. In fact, the test specimens used in the friction experiments are the same as those used in the calibration tests described in Chapters 2 and 3. As a result, the friction apparatus is absolutely calibrated in situ.

The experiments performed on the laboratory friction apparatus compare and contrast the friction behavior of two different materials: PMMA and rock. In addition to describing the general characteristics of stress waves produced during stick-slip, the directionality, time history, and absolute amplitudes of stress wave sources from friction are characterized. This in-depth analysis of friction sources demonstrates that sources located on a reflective interface must be modeled differently than those located on an acoustically transparent interface.

Many of the stress wave sources arising from friction are extremely discrete in space and occur rapidly in time (~1 μs), therefore they are considered to be due to the rupture of micrometer-sized asperities. Systematic differences in the characteristics of stress wave sources from the PMMA and rock are then linked to differences in asperity populations and rupture behavior, which are dictated by the differences in hardness and melting temperature. Chapter 5 also describes some general observations of the influence of surface roughness and fault healing on the generation of stress waves during stick slip, and how these seismically observable changes might reflect changes in the asperity populations which comprise the interface. These results raise further questions of scaling and how macroscopically observed material properties affect the strength and failure characteristics of asperity populations.

Chapter 2

Transfer Function Analysis Framework and Sensor Calibration

2.1. Introduction

Stress wave nondestructive testing (NDT) techniques, such as impact-echo (Sansalone and Streed, 1997), ultrasonic, and acoustic emission methods, use recorded signals to gain information about a material or structure. These signals are a function of source effects, wave propagation effects, and sensor effects, described schematically in Figure 2.1. To isolate and better understand source or propagation effects, the effects of the sensor on the recorded signal must be characterized. Specifically, we would like to know the precise physical quantity (displacement, velocity, etc.) to which the sensor output is most closely related and quantify any distortion that the sensor imparts to the signal. This characterization of the sensor's effects is referred to as sensor calibration.

In many cases, NDT researchers do not need to calibrate their sensing instruments, but sometimes researchers wish to quantitatively evaluate their results so that measurements can be linked to physically meaningful and independently measurable quantities. With absolute sensor calibration, results from one test can be compared to those of other tests performed using different recording instruments or different techniques. Absolute sensor calibration will enable researchers to quantitatively compare their findings with others, advance our collective understanding of the physics and mechanics, and lead to improved, traceable NDT techniques.

As illustrated in Figure 2.1, the sequence of events which lead to the recording of a stress wave signal can be separated into a number of distinct processes. For example, in a typical stress wave NDT test, a rapid reorganization of stress—perhaps due to a pulsing piezoelectric transducer, a ball impact, or the sudden propagation of a microcrack growing in the specimen—causes transient stress waves to propagate outward from the source. These stress waves cause a mechanical disturbance—some vibration or surface motion—which is detected by a sensor. The sensor converts the mechanical disturbance into an electrical signal, which is then analyzed or digitized and saved.

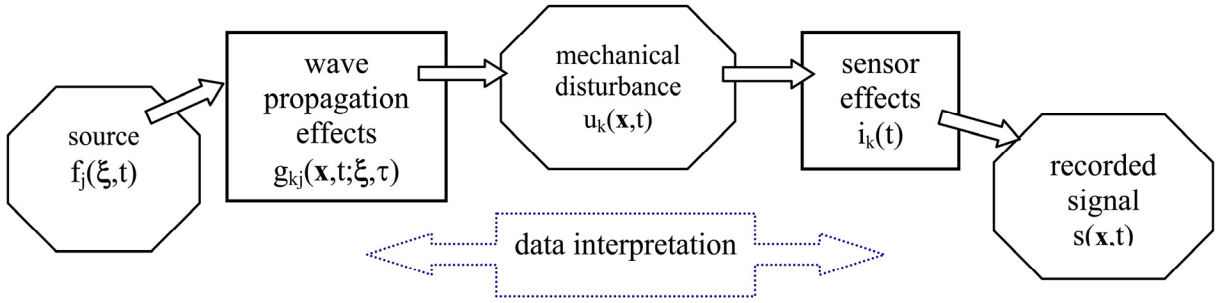

Figure 2.1. Block diagram of the sequence of events linking the source to the sensor output.

In order to calibrate a sensor, we must compare the sensor's output, $s(\mathbf{x},t)$, to the precise mechanical disturbance (e.g. the displacement, velocity, acceleration, strain) which caused the sensor's response. We must isolate the sensor's effects by calculating or measuring both the input to and the output from the *sensor effects* box, shown in Figure 2.1. This is accomplished in one of two ways: a mechanical disturbance, $u_k(\mathbf{x},t)$, can be measured with an independently

calibrated sensor (a reference sensor), or $u_k(\mathbf{x},t)$ can be calculated from theory. In many cases a reference sensor is not available, is not sensitive enough, or must be calibrated itself. Therefore, this chapter describes the procedure for sensor calibration against theoretical calculations.

The mathematical and conceptual framework upon which the current calibration approach relies is described in Section 2.2. Section 2.3 describes calibration sources and focuses on two different mechanical sources of stress waves used for calibration: ball impact and glass capillary fracture. Section 2.4 describes the characterization of wave propagation effects, using the elastodynamic Green's function. The estimation of the instrument response function in the frequency domain is then demonstrated in Section 2.5. Lastly, a convenient method for modeling the instrument response function in the time domain is described. These models can be used to simulate the sensor's distorting effects, or to remove the sensor effects from recorded signals.

For the purposes of case study and example, we tested four different types of acoustic emission sensors on a 50 mm thick steel plate, using a transfer function approach (Hsu et al., 1977; Eitzen and Breckenridge, 1987). Though attention is focused on AE sensors in particular, the methodology is valid for the wide variety of sensors common to the stress wave NDT methods (impact-echo, ultrasonic techniques, and the method of acoustic emission) which operate in the frequency range of ~10 kHz to ~4 MHz. The four sensors are the Glaser-type conical piezoelectric sensor, (e.g. Proctor, 1982; McLaskey and Glaser, 2009), the Physical Acoustics (PAC) PAC R15 and PAC NANO30, (e.g. Indrissi et al., 2003; Erson et al., 2006; Kappatos et al., 2009), and the DigitalWave B1025, (e.g. Prosser et al., 1999; Surgeon and Wevers, 1999; Weaver and Lobkis, 2003; Banjeree et al., 2007). The Glaser-type sensor is a laboratory-standard, wide-band displacement sensor, and the other three are widely used commercial sensors. The PAC R15 is a general purpose 150 kHz resonant sensor. The PAC NANO30 is described as a miniature sensor with nominal operating frequency of 270-970 kHz. The DigitalWave B1025 is a wideband sensor with a nominal operating bandwidth from 100 kHz to 3 MHz.

An alternative category of calibration, reciprocity calibration, utilizes the "reversible" nature of most piezoelectric sensors: they can be used as both a transmitter and receiver (Hsu and Breckenridge 1981; Eitzen and Breckenridge, 1987). In this method, two identical sensors are either directly coupled to one another ("face to face" method), or the two identical sensors are coupled to a common medium. The "face to face" method is not advised because this method does not take into account aperture and orientation effects and because sensors often behave differently when coupled to different materials, as described in Chapter 3 and Eitzen and Breckenridge (1987). Therefore, the sensor response observed when coupled to another sensor will be different than when coupled to a specimen. In the case of a common medium, a mechanical transfer function or Green's function for the transmission must be known, therefore the principle advantage of this method is that a well characterized calibration source is not needed. Reciprocity calibration does not work with newer sensors with built-in matching preamp, e.g. DigitalWave B1025LD, PAC-R15-AST.

2.2. Theoretical framework

The physics of wave propagation and transduction are extremely complicated. Instead of attempting to account for every detail, analysis of the stress wave NDT problem is cast into a simplified and idealized framework. This framework establishes the operating assumptions or rules by which mathematical and conceptual models operate. The analysis procedures and

calibration schemes are based on a transfer function framework (Hsu et al., 1977; Eitzen and Breckenridge, 1987) which relies on a Green's function formalism (e.g. Stump and Johnson, 1977; Aki and Richards, 1980). While this framework relies on some assumptions, stated below, it acts as a starting point from which problems can be posed and models can be tested.

Though all sensors have a finite aperture or sensing area over which physical measurements are averaged in some way, it is initially assumed that each sensor is essentially a point receiver, and that recorded signals are proportional to the wave field sampled at a single location, denoted **x**. Any distortions due to sensor aperture are simply treated as errors which cause the sensor response to diverge from the ideal case of a point receiver. Likewise, the calibration sources described in Section 2.3 are also assumed to act at point locations. The point-source and point-receiver assumptions simply imply that the source and sensor act on regions which are small compared to the wavelengths of interest. In many cases this is a valid assumption. These assumptions allow us to use a single Green's function for calibration and analysis. Alternatively, To and Glaser (2005) demonstrated the technique of integrating over multiple Green's functions for finite source or finite sensor problems.

The transfer function framework relies on the assumption that both the wave propagation effects and the sensor effects (the two boxes in Figure 2.1) can be modeled as linear, time invariant systems (e.g., Oppenheim and Shafer, 1999). In the context of NDT, this means that the materials and sensors behave the same today as they will tomorrow, and that signal amplitudes are directly proportional to source amplitudes if the frequency content and location of the source does not change. Under these assumptions, wave propagation effects can be mathematically described as a convolution with the appropriate Green's function, and the sensor effects can be described as a convolution with the sensor's instrument response function. Because a linear transfer function approach is employed, nonlinear details such as attenuation, scattering, and instrument saturation must be treated as exceptions to these rules.

The propagation of elastic waves is assumed to be well modeled by the elastodynamic equations of motion for an elastic continuum (Graff, 1975, Eq. 5.1.2; Aki and Richards, 1980 Eq. 4.1). Solutions to these equations can be found in the form of a Green's function, $g_{kj}(\mathbf{x},t;\boldsymbol{\xi},\tau)$, which describes the displacement in the k direction at point x at time t due to a unit impulsive force at location ξ in the direction j at time τ (Aki and Richards, 1980, Eq. 2.36). If the location ξ at which the dynamic force field acts is replaced by a point ξ_0, the Green's function can be expanded in a Taylor series about this point (Stump and Johnson, 1977). By taking only the first term of this series, the displacement at the sensor location can be expressed as

$$u_k(\mathbf{x},t) = f_j(\boldsymbol{\xi}_0,\tau) \otimes g_{kj}(\mathbf{x},t;\boldsymbol{\xi}_0,\tau). \qquad (2.1)$$

In this and subsequent equations, $\otimes$ represents convolution in time and $f_j(\boldsymbol{\xi}_0,\tau)$ is the source function, acting in the j direction, which is the sum of all forces in $\boldsymbol{\xi}$ that the source imposes on the test specimen.

Following Figure 2.1, the signal recorded from a sensor at location **x** can be expressed as

$$s(\mathbf{x},t) = u_k(\mathbf{x},t) \otimes i_k(t) = f_j(\boldsymbol{\xi}_0,\tau) \otimes g_{kj}(\mathbf{x},t;\boldsymbol{\xi}_0,\tau) \otimes i_k(t). \qquad (2.2)$$

Here, $i_k(t)$ is the instrument response function in the k direction which is to be determined in a calibration test. In the above formulation, knowledge of the Green's function, $g_{kj}(\mathbf{x},t;\boldsymbol{\xi},\tau)$, and instrument response function, $i_k(t)$, are sufficient to completely characterize the wave propagation and sensor effects, respectively.

In a calibration test, the sensor output, $s(\mathbf{x},t)$, must be compared to a theoretically calculated mechanical disturbance. In this work, recorded signals are compared to calculated displacement time history (Eq. 2.1). Aternatively, velocity, acceleration, and strain could be substituted, and can be derived from spatial or temporal derivatives of $u_k(\mathbf{x},t)$. Referred to as the 'theoretical signal', $u_k(\mathbf{x},t)$ is the specimen displacement in the i direction which should theoretically exist at the sensor location $\mathbf{x}$ on the calibration test specimen due to the forcing function $f_j(\xi,\tau)$ of the calibration source. The instrument response function $i_k(t)$ can be found by deconvolving Equation 2.1 from Equation 2.2:

$$i_k(t) = s(\mathbf{x},t) \otimes u_k(\mathbf{x},t)^{-1} = s(t) \otimes f_j(\boldsymbol{\xi},\tau)^{-1} \otimes g_{kj}(\mathbf{x},t;\boldsymbol{\xi},\tau)^{-1}. \tag{2.3}$$

This is most easily achieved in the frequency domain:

$$I_k(\omega) = \frac{S(\mathbf{x},\omega)}{U_k(\mathbf{x},\omega)} = \frac{S(\mathbf{x},\omega)}{F_j(\xi,\varpi)G_{kj}(\mathbf{x},\omega;\xi,\varpi)}, \tag{2.4}$$

where $I_k(\omega)$, $S(\mathbf{x},\omega)$, $U_k(\mathbf{x},\omega)$, $F_j(\boldsymbol{\xi},\varpi)$, and $G_{kj}(\mathbf{x},\omega;\boldsymbol{\xi},\varpi)$ are the temporal Fourier transforms of $i_k(t)$, $s(\mathbf{x},t)$, $u_k(\mathbf{x},t)$, $f_j(\boldsymbol{\xi},\tau)$, and $g_{kj}(\mathbf{x},t;\boldsymbol{\xi},\tau)$, respectively. To calculate $I(\omega)$ in this way, an experiment-theory pair ($s(t)$ and $u_k(\mathbf{x},t)$) must be obtained, so an experiment must be designed such that motions felt by the sensor under consideration are very well modeled by the theoretical signal, $u_k(\mathbf{x},t)$. This is achieved by employing a calibration source which is well modeled by a known forcing function, $f_j(\boldsymbol{\xi},\tau)$, and conducting the experiment on a specimen for which the wave propagation effects can be well modeled by a known or easily computed Green's function $g_{kj}(\mathbf{x},t;\boldsymbol{\xi},\tau)$.

2.3. Calibration sources

In order to characterize a sensor's effects and determine $i_k(t)$, a known source, $f_j(\boldsymbol{\xi},\tau)$, must be employed, which produces vibrations of known amplitude and shape. An ideal calibration source imposes a unidirectional force, acts on a region which is small in size (in order to satisfy the point source approximation), introduces waves with a broad range of frequencies into the test specimen, and has a smooth frequency spectrum over the entire frequency range for which the calibration is to be valid. Example sources can be found in Breckenridge et al. (1990).

Mechanical sources such as pencil lead break (Hsu, 1977), capillary fracture (Breckenridge et al., 1975), and impact (Goldsmith, 2001; McLaskey and Glaser, 2009), are ideal because they are intuitively simple, and the forces they introduce to a specimen are directly linked to physically meaningful, directly measurable quantities. These sources are impulsive or step-like, so they are very broadband in frequency, and their short temporal duration results in ideal waveforms for straightforward identification of the various wave phases (P waves, S waves, etc). Two different, well characterized, mechanical sources were used for absolute sensor calibration: glass capillary fracture, and ball impact, which is discussed in detail in Chapter 3.

Alternatively, electromechanical sources generated from capacitive and piezoelectric transducers offer excellent repeatability and are easily automated. The difficulty with electromechanical sources is that the precise electromechanical properties of the transducer are complicated and are typically unknown to the user. In order to precisely model the forces that the transducer imposes on the specimen, the source transducer itself must be well characterized: the instrument response, coupling effects, and radiation pattern must all be considered. Piezoelectric transducers are most often resonant and are therefore incapable of producing short duration pulses or steps without ringing or distortion (To and Glaser, 2005). Consequently, transducer sources are to be used only for relative calibration.

Thermo-mechanical sources excite stress waves in a material by rapid localized heating of a specimen via a pulsed laser, electric arc, or some other form of electromagnetic radiation (Scruby and Drain, 1990). These sources hold many of the same advantages as electromechanical sources—repeatability and easy automation—but suffer from the same drawback: because of their extremely complicated physics, they have not yet been characterized to the level of the two mechanical sources described below.

2.3.1 Glass capillary fracture

When conducting a calibration test using a glass capillary fracture, a short (~ 2 mm) length of thin walled glass capillary tube is laid on its side and slowly loaded in the direction perpendicular to the specimen face until it fractures. The glass capillary is loaded with a 2 mm diameter metal cylinder which is oriented with its axis parallel to the surface of the test block but perpendicular to the axis of the capillary tube. Capillary diameter is typically 100 to 400 μm, and under these conditions it typically breaks at a force of 5 - 25 N. When the capillary fractures, the surface unloads very rapidly. The force time history, f(t), that the capillary fracture imposes on the test specimen is very nearly equal to a step function with a rise time (unload time), $t_{rise} < 200$ ns (Breckenridge et al., 1975, 1990). This source has been used by many researchers because the force at which the fracture occurs, f_{amp}, is equal to the amplitude of the step, and can be independently measured for absolute calibration. The capillary-break forcing function can be modeled as

$$\begin{aligned} f(t) &= f_{amp}(1-\cos(\pi t/t_{rise}))/2 && 0 \le |t| \le t_{rise}, \\ f(t) &= 0 && t < 0, \\ f(t) &= f_{amp} && t > t_{rise}. \end{aligned} \qquad (2.5)$$

Typically, t_{rise} is very small and results in a frequency bandwidth much greater than that of the calibrated sensor, therefore the exact value of t_{rise} and the precise form of Equation 2.5 are unimportant.

2.3.2 Ball impact

For a ball impact calibration test, a small (~1 mm) diameter ball is dropped onto the test specimen. In these tests, the ball is typically dropped through a small hole in a platform of known height (from fingers or from a fine sponge) down a tall, clear plastic tube ~ 400 mm in diameter. The platform improves repeatability, and the tube prevents the ball from being lost on subsequent bounces. The impact imposes an impulse-like force. The precise forcing function,

f(t), that the ball imparts to the test specimen can be calculated from Hertzian theory, and is shown in Chapter 3 to be well modeled by

$$f(t) = f_{max}\sin(\pi t/t_c)^{3/2} \qquad 0 \le |t| \le t_c, \qquad (2.6)$$
$$f(t) = 0 \qquad \text{otherwise,}$$

where

$$t_c = 4.53(4\rho_1\pi(\delta_1+\delta_2)/3)^{2/5}R_1 v_0^{-1/5} \qquad (2.7)$$

is the time the ball spends in contact with the specimen, and the maximum force

$$f_{max} = 1.917\rho_1^{3/5}(\delta_1+\delta_2)^{-2/5}R_1^{2}v_0^{6/5}. \qquad (2.8)$$

In preceding equations, $\delta_i=(1-\mu_i^2)/(\pi E_i)$, and E and μ are the Young's modulus and Poisson's ratio, respectively. Subscript 1 refers to the material of the ball and subscript 2 refers to the material of the test specimen. Equation 2.6 is only strictly valid if the ball bounces back to the same height as it was dropped, but as a an approximation, if the ball bounces back to only half its original height, then the peak force $f_{max1/2} \sim= 0.75f_{max}$. By using balls of various sizes and different drop heights, the ball source offers variability in amplitude and frequency content with which to test the linearity and bandwidth of a transducer. The validity of Equation 2.6 is verified in Chapter 3.

Three different types of balls were used for the calibration tests described in this paper: a 1.00 mm diameter glass ball, a 0.79 mm diameter steel ball, and a 0.40 mm diameter ruby ball, pictured in Figure 2.2. Forcing functions, calculated from Equation 2.6, for the impact of these three balls when dropped 310 mm onto a 50 mm thick steel plate, are shown in Figure 2.2a compared with the forcing function for a glass capillary fracture (Eq. 2.5) with measured f_{amp} = 14 N and t_{rise} assumed to be 200 ns. The ruby ball produces a pulse ~1 μs in duration; the steel and glass balls produce pulses with a nearly identical ~2.3 μs duration, but different amplitudes.

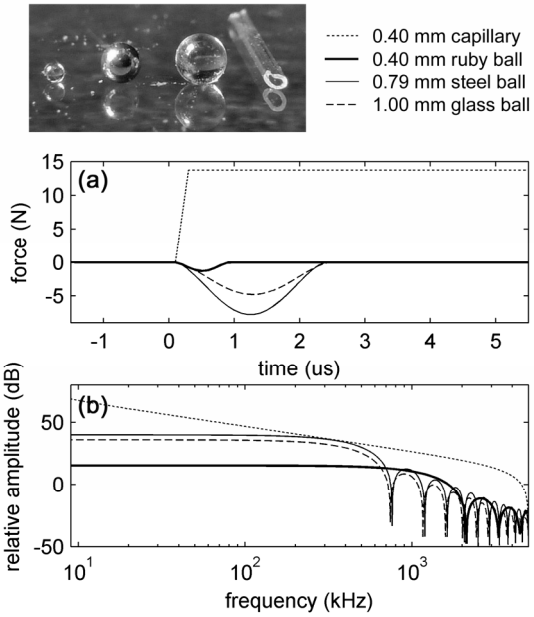

Figure 2.2. Force time functions (a) and corresponding frequency spectra (b) (estimated from Equations 2.5 and 2.6) for a glass capillary fracture calibration source and the impact of balls of various sizes and materials dropped 310 mm onto the surface of a 50 mm thick steel plate.

The amplitude of the Fourier transform of these source functions are shown in Figure 2.2b. As shown, the spectrum of the ball source is flat at low frequencies and consists of a series of lobes which are separated by zeros at higher frequencies. The zeros in the spectrum of the ball source make the calculation of $i_k(t)$ at these high frequencies particularly challenging, therefore calibrations which use the ball source are typically only assumed to be valid for frequencies below 0.85 $f_{zero,1} \approx 1.5/t_c$, where $f_{zero,1}$ is the frequency of the first zero.

2.4. Test geometry and Green's functions

An ideal test specimen for primary, i.e. absolute, calibration is one for which wave propagation can be well modeled. The geometry should be simple and the specimen made from a material which allows high frequency stress waves to propagate without excess attenuation or scattering. Greens functions can be calculated analytically for only a few geometries such as an infinite whole space and a half space (White, 1965; Johnson, 1974; Aki and Richards, 1980). For other specimen geometries, numerical models such as finite element or finite difference codes can be employed, but the calculation of Green's functions in this way is difficult because high frequencies require small grid spacing and low frequencies require a long-time duration. Green's functions used in this study were calculated by a computer program (Hsu, 1985) which uses a generalized ray theory approach. These Green's functions were then verified against theoretical solutions (Pekeris, 1955; Knopoff, 1958; Johnson, 1974) and finite element models (McLaskey and Glaser, 2009).

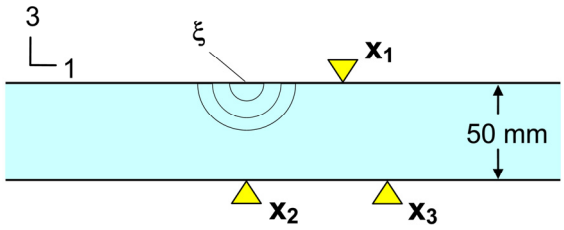

Figure 2.3. Experimental setup for the calibration tests on a thick plate. Three different sensor test positions relative to the location of the source, $\boldsymbol{\xi}$, are shown.

In the general case, a sensor responds differently to displacements in different directions, but the vast majority of NDT sensors are sensitive only to surface normal motion (the 3 direction in Figure 2.3), therefore it is assumed that $i_1(t) = 0$, $i_2(t) = 0$, and $i_3(t) = i(t)$. The sensor response is calibrated against the surface normal component of displacement, $u_3(\mathbf{x},t)$. Additionally, both the ball impact and capillary fracture calibration sources impose forces which act at location ξ, in the 3 direction, therefore only the Green's function g_{33} is needed, and Equations 2.3-2.4 reduce to the scalar equations:

$$i(t) = i_3(t) = s(\mathbf{x},t) \otimes u_3(\mathbf{x},t)^{-1} = s(t) \otimes f_3(\boldsymbol{\xi},\tau)^{-1} \otimes g_{33}(\mathbf{x},t;\boldsymbol{\xi},\tau)^{-1}. \tag{2.9}$$

$$I(w) = I_3(w) = \frac{S(\mathbf{x},w)}{U_3(\mathbf{x},w)} = \frac{S(\mathbf{x},w)}{F_3(\mathbf{x},v)G_{33}(\mathbf{x},w;\mathbf{x},v)}, \tag{2.10}$$

If, instead, a researcher wished to calibrate a shear sensor that is sensitive to motions in the 1 direction, he or she would need the Green's function g_{13}.

The calibration tests described below were performed on a 50 mm thick steel plate, 610 mm square. Three sensor positions relative to the location of the calibration source are shown in Figure 2.3. Position 1 ($\mathbf{x_1}$) is a surface location on the same side of the test block as the source and 45 mm away. Position 2 ($\mathbf{x_2}$) is the epicentral location, directly beneath the source. At this location, all displacements are in the plate normal direction and the aperture effect is minimized. The largest signal to noise ratio is typically achieved in Position 1 due to the presence of the very large amplitude Rayleigh wave, and the spectrum of the Position 1 Green's function is typically smoother than those of Positions 2 and 3, as shown in Figure 2.4d. The g_{33} Green's function for Position 2 is insensitive to small changes in the source or sensor locations. Position 3 ($\mathbf{x_3}$) is an off-epicenter location for which the wave displacements are at an oblique angle from the surface normal. Sensors in Position 3 will see both a P wave and a large S wave.

True Green's functions have units of pm/N/s and graphical presentation lacks intuitive meaning. Figure 2.4 instead shows calculated ground displacements for the three sensor positions, obtained from the convolution of the Green's functions $g_{33}(\mathbf{x_1},t;\xi,\tau)$, $g_{33}(\mathbf{x_2},t;\xi,\tau)$, and $g_{33}(\mathbf{x_3},t;\xi,\tau)$ with the force time function from the 400 μm ruby ball impact shown in Figure 2.2.

2.5. Instrument response in the frequency domain.

Once a well-characterized calibration source and suitable Green's functions for a particular sensor location have been found, one can obtain an experiment-theory input-output signal pair, $s(\mathbf{x},t)$ and $u_3(\mathbf{x},t)$, and use Equation 2.10 to directly estimate the instrument response. Examples of $s(\mathbf{x_1},t)$ and $u_3(\mathbf{x_1},t)$ are shown in Figure 2.5 for Position 1 on the 50 mm thick steel test plate. The theoretical signal, $u_3(\mathbf{x_1},t)$, is calculated from Equation 2.1, using $g_{33}(\mathbf{x_1},t;\xi,\tau)$. In this case, a glass capillary fracture source was used, therefore $f_3(\xi,\tau)$ was calculated from Equation 2.5. In other tests, the ball impact source was used and $f_3(\xi,\tau)$ was calculated from Equation 2.6.

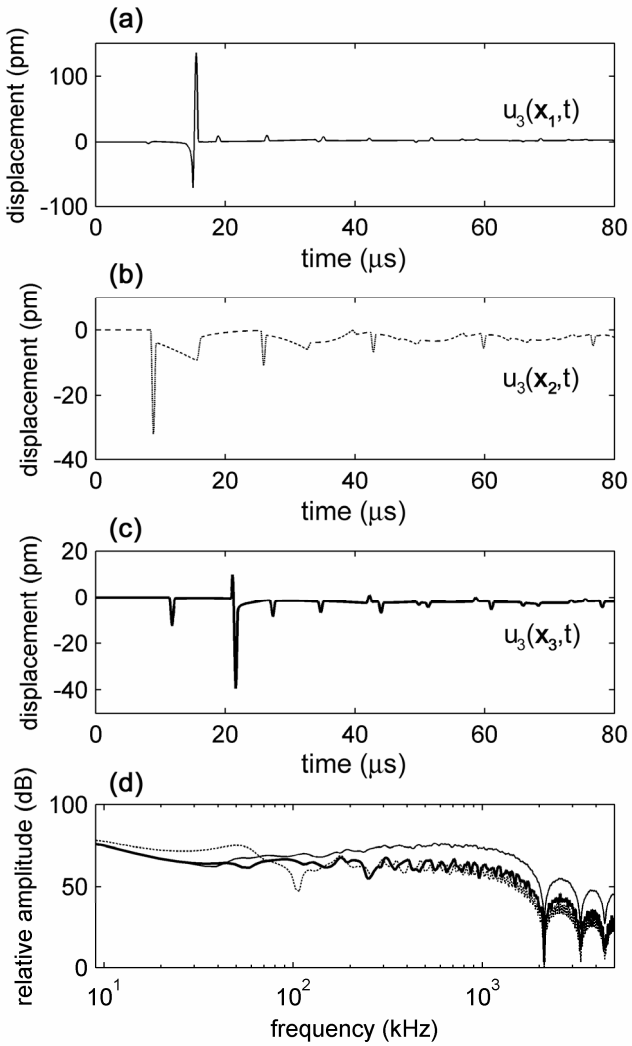

Figure 2.4. The theoretical displacement time histories in the plate normal direction. These synthetic signals are calculated by convolving the source function for a 0.40 mm ruby ball dropped 310 mm onto a 50 mm thick steel plate with the appropriate Green's functions for three different sensor positions. The sensor positions (relative to the source location) are shown in Figure 2.3. **a**, Displacements felt at Position 1, which is 45 mm away from the source and on the same side of the plate as the source, include a small amplitude P-wave which arrives before a large amplitude Rayleigh wave and small amplitude PP, PS, PPPP, PPPS, etc. reflections. **b**, displacements felt at Position 2, which is located directly beneath the source, through the thickness of the plate, are characterized by a large amplitude initial P-wave arrival, a ramp in displacement resulting from the near-field component of the displacement field, and a number of evenly spaced reflections (PPP, PPPPP, PPPPPPP, etc.) through the thickness of the plate. **c,** displacements felt at Position 3, which is offset 64 mm from Position 2, are characterized by a moderate-sized P wave and a strong S wave immediately preceded by converted evanescent wave which has opposite polarity. **d**, The amplitude of the Fourier transform of these three synthetic signals. The zeros in the spectra at approximately 2.2, 3.3, and 4.4 MHz are the result of the 0.40 mm ruby ball source function which is common to all three signals, while variations in the roughness of the spectra are due to the different Green's functions.

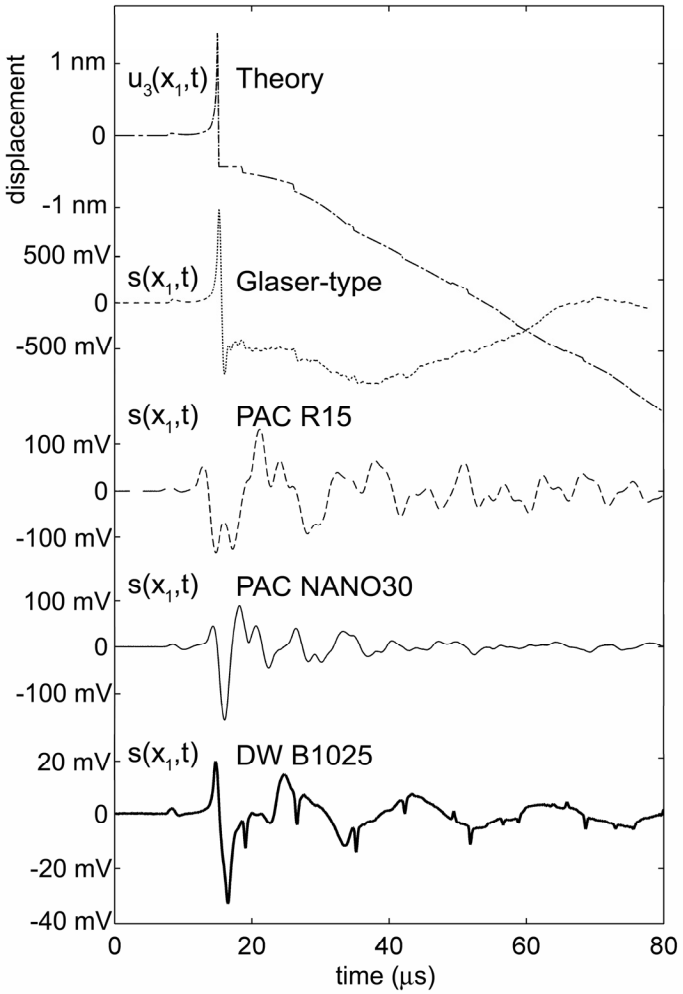

Figure 2.5. Experiment-theory pairs from a calibration test in sensor Position 1 on a 50 mm thick steel plate, which utilizes the fracture of a 0.40 mm glass capillary as a calibration source. The top trace is the theoretical signal calculated from Equation 2.1. The second through fifth traces are recorded signals from each of the four sensors tested: Glaser-type, PAC R15, PAC NANO30, and DW B1025, respectively. The sharp peak and step-like offset present in the trace of the Glaser-type sensor coincident with the Rayleigh wave at about 16 μs illustrates this sensor's ability to capture broad-band signals. The sharp, pulse-like reflections present in the trace of the DW B1025 sensor, which are coincident with the step-shaped reflections of theoretical signal, demonstrate that this sensor does a good job of damping out any waves reflected within the sensor, keeping the "coda" of the signal clean for the identification of later-arriving reflections.

Once an experiment-theory pair ($s(\mathbf{x},t)$ and $u_3(\mathbf{x},t)$) has been obtained, each signal is Fourier transformed in an identical fashion, and spectral ratios are taken. Figure 2.6 (a) shows the amplitude of the Fourier transform (FT) of the signals shown in Figure 2.5. All signals were digitized at 10 MHz, windowed with a 400 μs Blackman Harris window centered on the first wave arrival, and Fourier transformed with the fast Fourier transform (FFT) algorithm. Following Equation 2.10, $S(\mathbf{x},\omega)$ is divided by $U_3(\mathbf{x},\omega)$ at each Fourier frequency to obtain $\hat{I}(\omega)$, which is an estimate of the true instrument response spectrum, $I(\omega)$. Since the sensors are calibrated against a theoretical displacement time history, $|\hat{I}(\omega)|$ is an estimate of the displacement response spectra. The amplitude and phase of $\hat{I}(\omega)$ are shown in Figure 2.6c and 2.6d, respectively, for the Glaser and NANO30 sensors. As shown, the sensitivity of the PAC

sensor has a peak at about 150 kHz, while the Glaser-type sensor has a near-flat response from 20 kHz to 1 MHz.

The calibration is not valid in any frequency range where the signal to noise ratio (SNR) approaches 1. As an illustrative example of how SNR affects calibration bandwidth, noise spectra are included in Figure 2.6b-c. The noise signal, n(t), is a 400 μs segment of the recorded signal taken before the first wave arrival and windowed with the Blackman Harris window. The amplitude of the FT of the noise signals (which are unique for each sensor and data acquisition setup) are shown in Figure 2.6b for the Glaser and NANO30 sensors. Noise spectra are obtained by dividing the FT of n(t) by $U_3(\mathbf{x},\omega)$, and are shown in Figure 2.6c. For this capillary fracture test, the SNR drops to 1 at about 1.8 MHz for the NANO30 sensor and at about 4 MHz for the Glaser-type sensor. When the SNR drops to 1, calibration results are certainly not valid. Figure 2.6c illustrates one of the benefits of the absolute calibration scheme: because the recorded signal was in units of Volts and the theoretical signal was in units of nm, the instrument response function has units of V/nm rather than mere "amplitude." Finally, the phase of $\hat{I}(\omega)$ for the two sensors is shown in Figure 2.6d. For the Glaser-type sensor, the phase does not vary more than about one radian over nearly two decades of frequency. The PAC NANO30 sensor shows more rapid fluctuations in phase associated with peaks and troughs in the amplitude response of the sensor, likely due to resonances in the structure of the sensor. For both sensors, the phase of $\hat{I}(\omega)$ becomes erratic and diverges when the SNR becomes small. This is because phase is undefined when the amplitude is effectively zero.

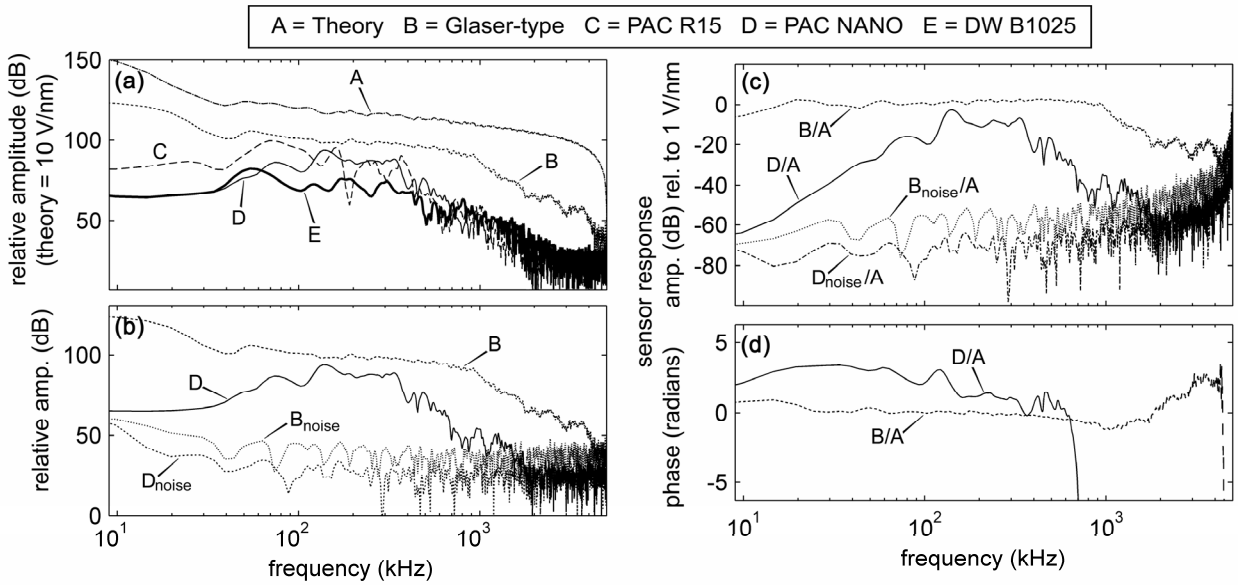

Figure 2.6. Spectra for the calculation of instrument response function in the frequency domain. (a) The amplitude of the FT of the five signals shown in Figure 2.5, (b) the amplitude of the FT of the Glaser-type and PAC NANO30 signal shown alongside the amplitude of the FT of the noise for these two sensors, (c) amplitude of $\hat{I}(\omega)$, obtained via spectral ratios, for the Glaser-type and PAC NANO30 sensors are compared to and the amplitude of the respective noise spectra, and (d) the phase of $\hat{I}(\omega)$.

2.5.1. Accuracy of source models, directionality, and aperture effect

The accuracy of the source models is explored by comparing $\hat{I}(\omega)$ obtained from calibration tests which utilize different calibration sources. The effects of directionality and the finite aperture of the sensors can be seen from a comparison of $\hat{I}(\omega)$ obtained from tests with different sensor positions. Note that a different Green's function must be used for each different sensor position. Figure 2.7 compares $|\hat{I}(\omega)|$ made using two different calibration sources and two different sensor positions. The spikes in $|\hat{I}(\omega)|$ from the ball drop source, at approximately 2.2, 3.3, and 4.4 MHz, are due to the presence of zeros in the spectrum of the 0.40 mm diameter ruby ball impact source model at those frequencies. The ball impact and capillary fracture source models yield $|\hat{I}(\omega)|$ that are in very good agreement at lower frequencies; at higher frequencies (above 500 kHz) the results from the two gradually diverge, indicating increasing uncertainty of the source models in the MHz range. For the Glaser-type sensor, there is little difference between $|\hat{I}(\omega)|$ obtained from tests in Position 1 and Position 2. In contrast, the PAC R15, PAC NAN030, and the DW B1025 sensors have decreased high frequency sensitivity when tested in Position 1 compared to Position 2. This difference in sensitivity is most likely due to directionality effects such as the aperture effect (Eitzen and Breckenridge, 1981). At high frequencies, the wavelengths of recorded waves are comparable to the area of contact, or aperture, of these sensors. This can cause the sensor to average over more than one wavelength, decreasing the recorded wave amplitude. The aperture effect is maximized in Position 1, where waves arrive tangential to the sensor face, and minimized in Position 2, where the waves arrive normal to the sensor face. The aperture effect is most evident on the DW B1025 and PAC R15 sensors because the diameter of their piezoelectric elements is large compared to those of PAC NANO30 and Glaser-Type sensors. The nominal area of contact of the DW B1025 sensor is 8 mm, which is equal to the wavelength of S waves in steel at 400 kHz. At this frequency, the aperture effect is expected to become important for the DW B1025 sensor. Similarly, aperture effects are expected to become important for the PAC R15 (nominal aperture of 16 mm) at 200 kHz, for the PAC NANO30 sensor (5.5 mm diameter) at 550 KHz, and for the Glaser-type sensor (0.5 mm diameter) at 6.4 MHz. In materials with a lower wave speed, such as plastic, the wavelengths at a fixed frequency are somewhat smaller than in steel, therefore the aperture effect will be more significant and will affect a lower frequency band.

While the described methodology relies on a number of idealizations, the close match between the results of ball drop and capillary source calibrations (Figure 2.7), demonstrates the validity of the source models described in Equations 2.5 and 2.6. Figure 2.7a shows that the Glaser-type sensor is indeed sensitive to only one component of displacement, because the instrument response is unchanged when waves arrive from different directions. For the other sensors, directionality effects are non negligible at high frequencies, but these deviations can be quantified and accounted for. The Glaser-type sensor has a nearly flat response spectrum, therefore it is best described as a displacement sensor. The DW B1025 sensor has a nearly linear displacement response spectrum with a slope of 1 (20 dB per order of magnitude in frequency) between 0.1 and 1 MHz, therefore it is best described as a velocity sensor over this frequency band. A reference line which indicates a flat velocity response spectrum is shown in Figure 2.7d. The PAC sensors are sensitive to a combination of displacement, velocity, and acceleration which varies with frequency.

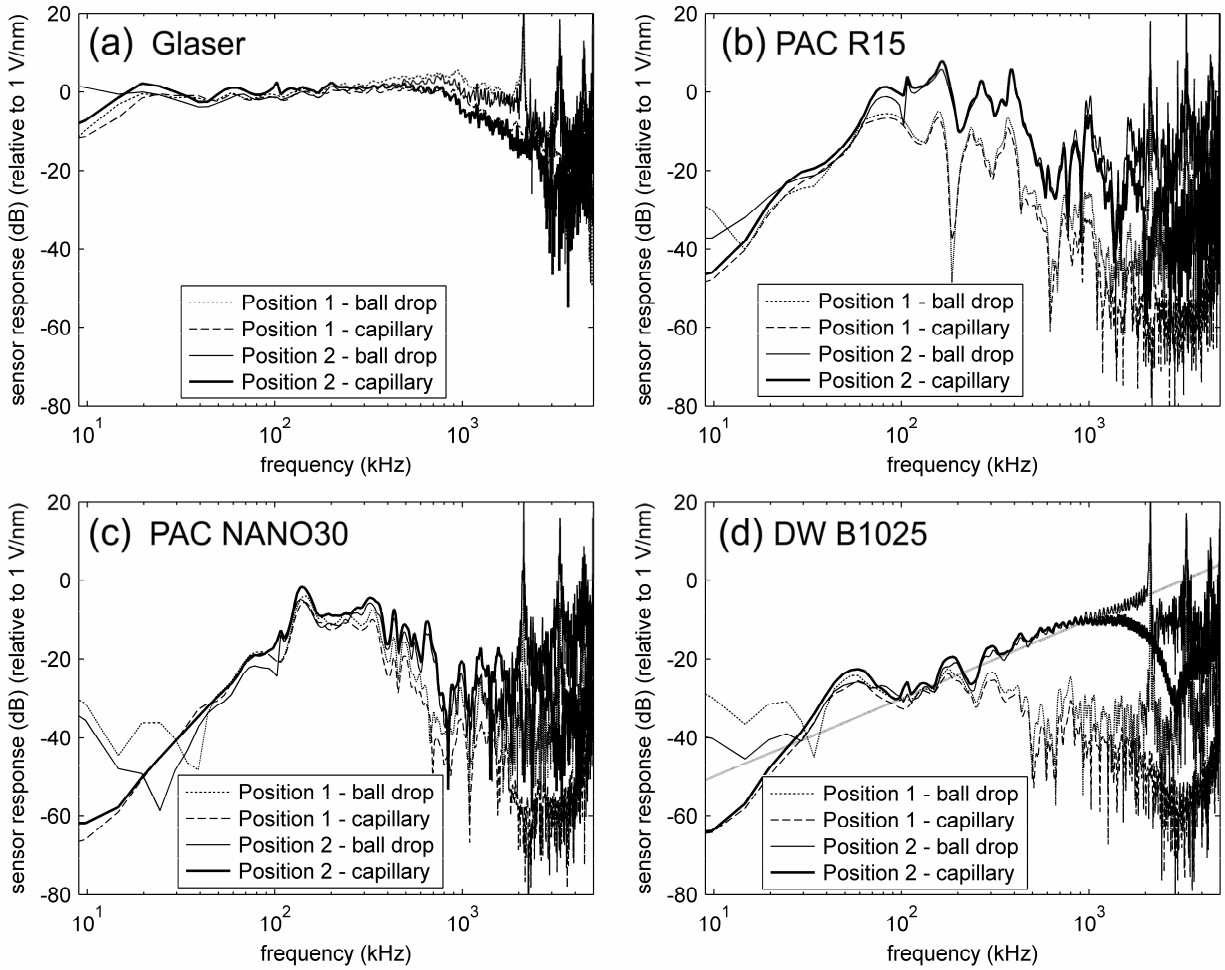

Figure 2.7. Calibrations using different combinations of sensor positions ($\mathbf{x}_1$ and $\mathbf{x}_2$) and calibration sources (0.40 mm ruby ball impact and 0.40 mm glass capillary fracture), for the four different sensors tested. Differences between curves from tests using the different sensor positions indicates aperture effects. The similarity between curves from tests using different sources verifies the accuracy of two source models. The reference line shown in (d) indicates a flat velocity response spectrum.

2.6. Time domain modeling of instrument response

The frequency domain methodology described in Section 2.5 requires only spectral division (Eq. 2.10), but in that approach, important phase information can be easily lost or distorted due to the influence of noise and windowing. Alternatively, when calculating the sensor response in the time domain (Eq. 2.9), phase information is more robustly incorporated into the solution. Phase information is crucial for the simulation or removal of sensor distortion from time domain signals, so that physically meaningful measurements can be obtained. The main challenges of the time domain approach are the practical issues involved in deconvolution (e.g., Michaels, 1982). In order to circumvent many of these problems, the instrument response function is not found from direct inversion (Eq. 2.9). Instead, the sensor response is approximated with a time domain model (see, for example, Shumway and Stoffer, 2006); $u_3(\mathbf{x},t)$ and $s(\mathbf{x},t)$ are used as the input and output, respectively, to estimate the model parameters. For brevity, only one type of model is considered: the commonly-used autoregressive moving

average (ARMA) model (Ljung, 1987; Marple and Lawrence, 1987; Shumway and Stoffer, 2006) of the form:

$$s(\mathbf{x},t) = \sum_{k=0}^{n} b_k u_3(\mathbf{x},t-kT) - \sum_{j=1}^{m} a_j s(\mathbf{x},t-jT) \qquad (2.11)$$

where T is the sampling period (T = 100 ns, for the examples in this study), and a and b are arrays containing the autoregressive and moving average (convolutional) model parameters, respectively.

A time domain model is a tool for representing a system or process (transfer function) which maps one signal (in this case $u_3(\mathbf{x},t)$) into another signal ($s(\mathbf{x},t)$). The purpose of the current ARMA model is to numerically simulate the distorting effect that the sensor has on $u_3(\mathbf{x},t)$ and to allow it to be efficiently removed from an arbitrary $s(\mathbf{x},t)$. The ARMA model itself will have a response function, referred to here as the ARMA response spectrum in the frequency domain. The ARMA model has many fewer parameters than the number of data points in $u_3(\mathbf{x},t)$ and $s(\mathbf{x},t)$, so the parameters can be estimated using a least squares formulation. Many criteria exist by which the user can determine the near-optimal number of parameters (m and n, in Equation 2.11) to be included in the ARMA model (i.e. Akaike's information criterion), but ultimately it is a tradeoff between under-parameterization, which can decrease the sensitivity of the model to noise and small errors in the Green's function estimates, and over-parameterization, which allows a more complicated model, and can provide a better fit between the ARMA response spectrum and the instrument response spectrum, $\hat{I}(\omega)$. A sensor which has a flat or smoothly varying response spectrum will require only a simple model with few model parameters, while a sensor with a very rough or jagged spectrum will require a more complicated model and more parameters (larger m and n) for the same quality of fit between the ARMA response spectrum and $\hat{I}(\omega)$.

The system identification toolbox of the commercial software *MATLAB* (Ljung, 2006) is employed for the determination of ARMA model parameters for each of the four sensors tested. An example of ARMA-model building and validation is shown in Figure 2.8 for the PAC R15 sensor calibrated in Position 2, using the impact of a 0.40 mm ruby ball dropped 310 mm onto the steel test plate as a calibration source. First, an input-output pair ($u_3(\mathbf{x},t)$ and $s(\mathbf{x},t)$) is obtained from the calibration test. Here, we denote these signals as $u^{build}(t)$ and $s^{build}(t)$. Then, to illustrate the effect of different model complexity, four different ARMA models (m = n = 16, 50, 160, 220) were derived from this pair. The "arx" command in *MATLAB* computes least squares estimates of a and b vectors, given $u^{build}(t)$ and $s^{build}(t)$. (For simplicity, only models where m = n were chosen.) The amplitude of the ARMA response spectra for each of the four models are shown in Figure 2.8a. As shown, when the number of parameters of the ARMA model is increased, the ARMA response spectrum becomes more detailed and more closely matches $|\hat{I}(\omega)|$ (Figure 8a, dashed lines) which was estimated from $u^{build}(t)$ and $s^{build}(t)$ following the methodology of Section 2.5.

Once the model parameters have been determined, the ARMA model can be used in a forward sense (as a filter) to simulate the distorting effects of the sensor on an arbitrary displacement time history. This is accomplished by substituting an arbitrary displacement time history in for $u_3(\mathbf{x},t)$ in Equation 2.11, or by means of the "filter" command in *MATLAB* or equivalent software. Alternatively, the ARMA model can be used in an inverse sense to remove

the effects of the sensor from an arbitrary recorded signal, s(**x**,t), and obtain an estimate, û(t), of the displacement time history, u_3(**x**,t), felt by the sensor. The ARMA response spectrum is intended to match Î(ω), therefore deconvolving the ARMA response function from any recorded signal will essentially remove the effects of the sensor from that signal. This deconvolution method, which is aided by an ARMA model, is preferable for removing sensor distortion over other methods (e.g. inverse Fourier transforming the result of Equation 2.10 or calculating $g_{33}(\mathbf{x},\omega;\boldsymbol{\xi},\varpi)^{-1}$), since S(**x**,ω) is divided by the relatively smooth ARMA spectrum rather than by Î(ω), which can have precipitous zeroes. Here, it is assumed that I(ω) is a relatively smooth function and that we have intelligently chosen the ARMA model order so that the ARMA spectrum is detailed enough to capture the general features of I(ω) but still smoothes over the fine details of Î(ω), which are assumed to be the result of noise from s^{build}(t). To accomplish the ARMA deconvolution, we divide S(**x**,ω) by the ARMA response spectrum, calculated using *MATLAB* "freqz" command, and apply an inverse FT to the result.

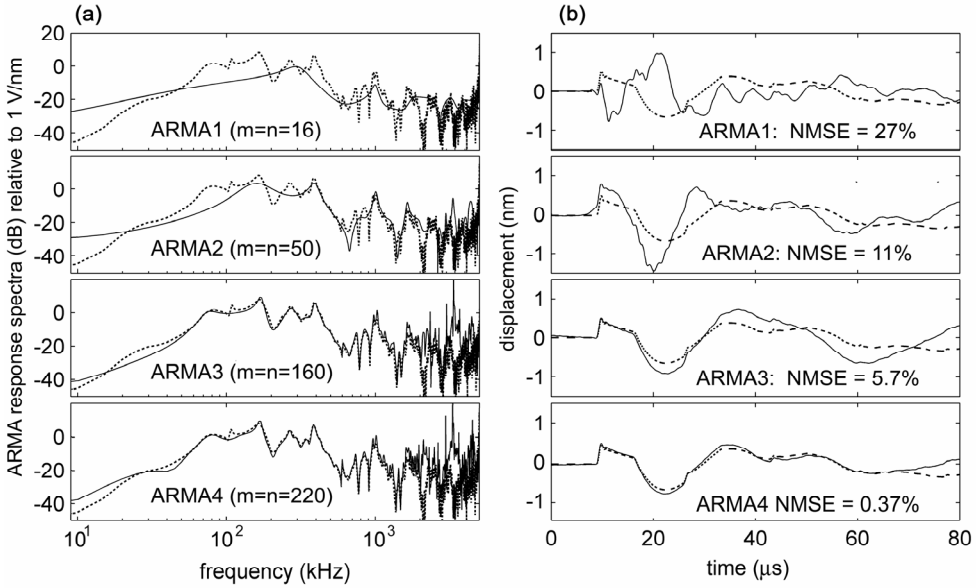

Figure 2.8. ARMA model building and validation for the PAC R15 sensor. (b), The ARMA response spectra (solid lines) are compared to |Î(ω)| (dashed lines) for four ARMA models with m = n = 16, 50, 160, and 220 parameters. A larger number of parameters yields a more detailed ARMA response spectrum. (a) Estimates of displacement time history obtained by deconvolving the ARMA response spectrum from s^{val}(t) are compared to u^{val}(t) for each of the four ARMA models of increasing complexity. Signals shown in **a** have been band passed between 15kHz and 1 MHz.

Finally, the models are validated with a second input-output pair, denoted u^{val}(t) and s^{val}(t), obtained from a second calibration test, this time using a glass capillary fracture as a source. Figure 2.8b shows a comparison between the theoretical displacement time history, u^{val}(t) (dashed lines), and displacement time history estimates, û(t), (solid lines), obtained by deconvolving the ARMA response spectrum from s^{val}(t). As the number of parameters of the ARMA model increases, û(t) more closely matches u^{val}(t). In this case, the ARMA model with m = n = 16 does a poor job of capturing the complicated response of the PAC R15 sensor. Some improvements are made by increasing the parameters to m = n = 50. The third model (m = n = 160) does an excellent job of capturing all but the low frequency effects of the PAC R15 sensor, while the fourth model (m = n = 220) shows modest improvements over the third. The goal is to

intelligently choose the ARMA model with the lowest number of parameters whose response spectrum adequately matches I(ω).

Model error can be quantified with the normalized mean square error (Baise et al., 2001),

$$NMSE = \frac{1}{p}\sum_{i=1}^{p}\frac{\left(\hat{u}(t+iT)-u^{val}(t+iT)\right)^2}{u_{\max}{}^2}, \qquad (2.12)$$

where u_{max} is the maximum of $u^{val}(t)$. The four models for the PAC R15 sensor, described in Figure 2.8, produced NMSE of 27%, 11%, 5.7%, and 0.37% for the m = n = 16, 50, 160, and 220 models, respectively. In contrast, the smoothness of the spectrum of the Glaser-type sensor required an ARMA model of only m=n=20 parameters to achieve a NMSE of 0.46%. The effects of this model for the Glaser type sensor is shown in Figure 2.9.

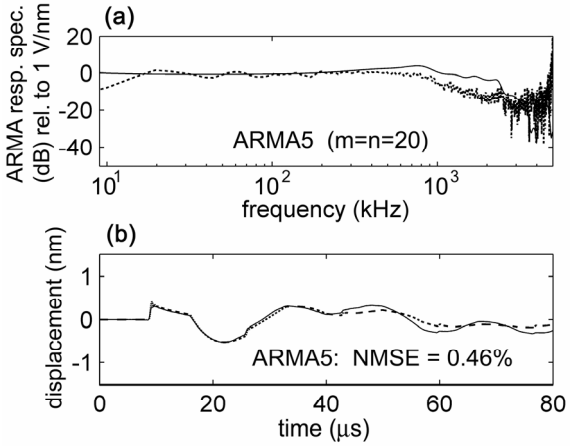

Figure 2.9. An example of an ARMA model (m=n=20) intended to mimic the Glaser-type sensor. The model was built with an input-output pair obtained from a calibration test in Position 2, using the impact of a 0.40 mm ruby ball dropped 310 mm onto the steel test plate, and it is validated using an input-output pair obtained from a glass capillary test in the same position.

2.7. Conclusions

This chapter describes how calibration sources and wave propagation effects can be modeled so that the instrument response can be estimated from simple but powerful experiments. The framework and methodology are useful for gaining physical measurements from recorded signals, and are also practical for the NDT researcher. Unique to this method, two different calibration sources are employed so that the accuracy of both source models can be attained. Additionally, two different source-sensor orientations were used, each with unique Green's functions. This allows the effects of directionality to be evaluated. Results from these calibration studies highlight the differences between the four sensors tested and illustrate some of the ways in which real sensor response deviates from the ideal case. For example, the DW B1025 sensor is well described as a velocity sensor in the 80 kHz to 1 MHz frequency band, but, when waves arrive from low incidence angles, the effect of the 8 mm aperture of the sensor can cause considerable distortions at frequencies above about 300 kHz. In contrast, the Glaser-type sensor

is well described as a displacement sensor in the 20 kHz to 1 MHz frequency band, and the 0.5 mm sensor contact area introduces negligible aperture effects. The response of the two PAC sensors is not easily linked to a single physical quantity such as surface velocity or displacement. Instead, theses sensors respond to a frequency-dependent mixture of displacement, velocity, and acceleration, which is considerably more complicated to model.

The theoretical framework described in this chapter is valid for any frequency band. Experimental constraints are what limit the calibration range to ~50 kHz - ~2.0 MHz range. At high frequencies, a very strong source is needed to achieve a high SNR because the sensors described tend to lose sensitivity in the MHz range. At low frequencies, long time windows are needed so that many periods are captured within the recorded signal. Long-time Green's functions require the inclusion of reflections from the side edges of the plate, and these additions make the Green's functions more complicated and more sensitive to small errors in geometry and wave velocities. In this study, Green's functions were calculated for an infinite plate geometry, so the 610 mm square steel test plate restricts time windows to 400 μs. Consequently, there is high uncertainty in spectral estimates below about 50 kHz, where less than 20 periods were captured in the time window.

The frequency domain methods described in Section 2.5 are convenient for estimating the instrument response spectrum, so that the flatness or resonant frequencies of a sensor can be determined, and different sensors can be compared or classified, but the time domain models of Section 2.6 are more useful for the simulation or removal of sensor effects, because indispensable phase information is “hard-wired” into the solution. The determination of a model which captures the salient features of a sensor's instrument response allows us to obtain physical quantities (i.e. surface displacements) from recorded signals. Building a suitable time domain model to mimic a particular sensor's effects is somewhat of an art. Nevertheless, this study demonstrates that it is possible to build, validate, and quantify the suitability of a given model from the results of simple calibration experiments, even for the more complicated PAC R15 sensor. The calibration techniques described in this chapter allow researchers to ascertain the strengths and limitations of instrumentation and the physical meaning of recorded signals--necessary steps toward building reliable and standardized NDT techniques.

Chapter 3

Experimental Study of Hertzian Impact

3.1 Introduction

The normal impact of a ball on a massive body has been extensively used as a source of stress waves for non-destructive testing techniques such as impact echo and acoustic emission (e.g. Sansalone and Street, 1997; Breckenridge et al., 1990; Lange and Ustinov, 1983). Ball impact is in some cases preferable to sources such as pencil lead fracture (Hsu, 1977) or pulsed laser (Scruby and Drain, 1990) because the stress wave signature that it imparts can be calculated from Hertzian contact theory (Hunter, 1957; Reed, 1985). Hertz's contact model (1882) is both elastic and quasistatic in nature; it neglects to consider both radiated elastic waves and anelastic effects, such as plasticity and viscoelasticity. Hertz law has been used beyond the limits of its validity on the basis that it accurately predicts those impact parameters which can be experimentally verified (Davies, 1949; Goldsmith, 1960). As test methods become more precise, and theoretical and numerical studies more detailed, there is a need to experimentally validate the Hertzian impact model and to quantitatively evaluate its limits.

This chapter focuses on the measurement of two impact parameters: the force time history, or force pulse, that the ball imposes on the massive body, and the coefficient of restitution (e)—defined as the ratio of the magnitudes of the rebound and approach velocities of the ball. The force pulse describes the ball's change in momentum over time, shown to be intimately related to the stress waves radiated from the collision, while e is a measure of the total kinetic energy lost to non-conservative processes such as radiated stress waves, plastic deformation, and viscoelasticity (Falcon et al. 1998). In particular, the applicability of different Hertzian derivations of the force pulse published by Hunter (1957) and Reed (1985) is examined.

A well-parameterized experimental campaign was undertaken verify the suitability of Hertzian impact as a calibration source. Impact-generated vibrations were recorded with Glaser-type displacement sensors calibrated as in chapter 2. By carefully accounting for wave propagation effects, estimates of the force pulse were obtained and compared to the Herztian-derived pulse. We experimentally verify the Reed (1985) correction to Hunter's (1957) estimation of the force pulse by measuring the locations of zeros in the spectral content of measured waves. The validity of Hertzian theory is also assessed for cases in which plastic deformation and surface effects absorb some of the ball's kinetic energy during the collision. Our methodology is similar to that of previous researchers (Davies, 1949; Crook, 1952; Goldsmith and Lyman, 1960; Chang and Sun, 1989; Buttle and Scruby, 1990) but employs a more exact treatment of wave propagation effects, and takes into careful consideration the response function of the sensors used to record the stress waves.

3.2 Methods

A schematic of the test setup is shown in Figure 3.1. As depicted, the collision of a ball (a) at location (b) on a massive plate (c) of thickness h is the source of the radiating stress waves (d) which are detected by an array of sensors (e). The signals recorded and analyzed are a function of the source, the test block and array geometry, and the sensors themselves. Under the Green's function formalism presented in Chapter 2, the stress wave source is represented by a

force function, the propagation effects are represented by the Green's function for a particular plate material and source-sensor orientation, and the effects of the sensor are represented by the sensor's instrument response function.

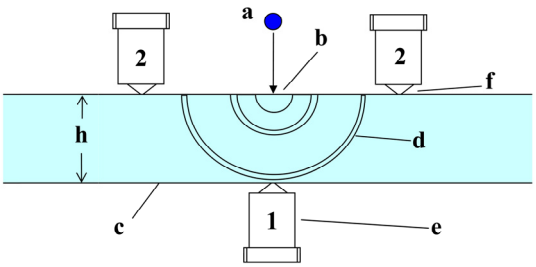

Figure 3.1. Schematic diagram of the test setup which includes a massive plate, (a), and a ball, (b), colliding at the source location, (c), which generates radiated stress waves, (d), detected by an array of sensors, (e), each of which employs a conical piezoelectric sensing element, (f). One sensor is located directly opposite and on the underside of the source location (Position 1), and two more are located 45 mm from the source on the loaded surface of the plate (Position 2).

As was shown in Chapter 2, these Glaser-type sensors are sensitive only to surface normal displacments. Additionally, for the ball drop and capillary fracture sources considered, $f_j(\xi_0,\tau)$ is assumed to act only in the plate-normal direction. Under these reasonable assumptions, Equation 2.1 reduces to the scalar equation:

$$u_3(\mathbf{x},t) = f_3(\xi_0,\tau) \otimes g_{33}(\mathbf{x},t;\xi_0,\tau). \qquad (3.1)$$

where the coordinate system is chosen so that "3" denotes the plate normal direction.

3.2.1. Test plates and Green's functions

For these experiments, the test blocks are plates of homogeneous materials. Material properties, geometry, and P-wave travel times of the four plates used in this study are shown in Table I.
For times less than t_{max} (see Table 3.1), the plate can be considered infinite; therefore Green's functions were calculated using a generalized ray theory code for infinite plates (similar to Ceranoglu & Pao, 1981). This solution was checked by the theoretical calculations of Knopoff (1958) at the epicentral location, and Pekeris (1955) on the same surface for times preceding the arrival of the first P wave reflection, and by finite element models (McLaskey & Glaser, 2009).

Material	**ρ** (kg m^{-3})	**c_p** (mm μs^{-1})	**c_s** (mm μs^{-1})	**h** (mm)	**w** (mm)	**t_w** (μs)	**t_{max}** (μs)
Steel	7850	5.90	3.23	50.1	610	8.49	100
Aluminum	2700	6.35	3.17	32.4	610	5.09	96
Glass	2480	5.90	3.50	24.4	760	4.14	125
PMMA	1190	2.81	1.40	50.1	940	17.83	220

Table 3.1. Plate properties: density (ρ), P-wave velocity (c_p), S-wave velocity (c_s), plate thickness (h), side length (w), time taken for P-waves to traverse the thickness of the plate ($t_w = h/c_p$), and time required for P waves to reflect off the plate edge and return to the center ($t_{max} = w/c_p$).

The sensor array, shown in Figure 3.1, is configured such that one sensor is located directly opposite and on the underside of the source location (Position 1), and two more are

located 45 mm from the source on the loaded surface of the plate (Position 2). The Green's functions for sensor Positions 1 and 2 on the steel plate, shown in Figure 3.2 (a) and (b), respectively, are plotted against $t_n = t/ t_w$ where t_w is the P-wave travel time through the plate thickness. The corresponding power spectra are shown in Figure 3.2 (c). The spikes at $t_n = 1, 3, 5$, etc. in Figure 3.2 (a) correspond to the multiple reflections of the P-wave through the thickness of the plate.

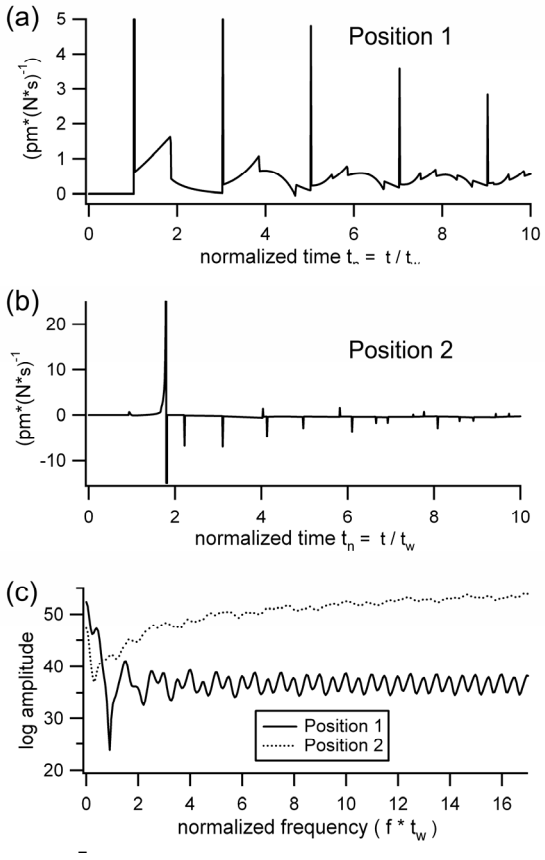

Figure 3.2. Green's functions for sensor Position 1, (a), and sensor Position 2, (b), and their corresponding amplitude spectra, (c). Sensor positions are sketched in Figure 3.1.

The plates in this study are considered "thick" because, for nearly all collisions considered, the contact duration t_c is less than twice t_w. Therefore, from the ball's perspective, the plate is infinitely thick and plate effects such as those studied by Zener (1941) and the effects of the plate supports could be neglected.

Damping (intrinsic attenuation) in each of the plate materials were estimated following the methods of To and Glaser (2005). In the glass, aluminum, and steel, Q was too high to be precisely measured for the frequency range (20 kHz - 1 MHz) and propagation distances (<1 m) under consideration. Only the polymethylmethacrylate (PMMA) plate produced non-negligible damping (Q = 80). This damping term was included in PMMA Green's function calculations.

3.2.2. The source function and Hertzian impact

While a number of different seismic sources have been explored for calibrating sensors of this type (Breckenridge et al., 1990), two dissimilar sources were chosen for this work: glass

capillary fracture and ball impact. The fracture of a 2 mm length of 0.25 mm outer diameter, 0.153 mm inner diameter, borosilicate glass capillary was used as the source. This source produces a forcing function which is approximated by a step function with a rise time of less than 200 ns (Breckenridge et al., 1975). The amplitude of the step is equal to the force at which the fracture occurs (usually between about 2 and 20 N), which was independently measured for absolute calibration. A small amount of variability (approximately 4 dB/MHz from 0.5-1.5 MHz) was measured in the shape of the frequency spectra of this source, likely due to variability of fracture strength of a particular glass tube.

A complete derivation of Hertzian impact theory can be found in Goldsmith (2000), Johnson (1985), and Love (1927); we present only an abbreviated formulation of the equations useful for this study. The force pulse that an impacting ball imparts to a massive body was derived by Hunter (1957) by applying a quasistatic formulation and Newton's second law. His solution is very well approximated by a "half sine" pulse of the form

$$\begin{aligned} f_H(t) &= f_{H\max}\sin(\pi t / t_c) && 0 \le |t| \le t_c \\ f_H(t) &= 0 && \text{otherwise} \end{aligned}, \tag{3.2}$$

where the contact time

$$t_c = 4.53\left(4\rho_1\pi(\delta_1+\delta_2)/3\right)^{2/5} R_1 v_0^{-1/5}. \tag{3.3}$$

For Equations 3.2 and 3.3, $\delta_i = (1-\nu_i^2)/(\pi E_i)$, E is the Young's modulus, and ν is the Poisson's ratio. Subscript 1 refers to the material of the ball and subscript 2 refers to the material of the plate. The constant $f_{H\max}$ depends on the material properties of the ball and the massive body as well as R_1, v_0, and ρ_1, which are the radius, approach velocity, and density of the ball, respectively. Time t = 0 is the initiation of contact.

Reed (1985), made a correction to Hunter's calculation by using the force deformation relation $f = k_1\alpha^{3/2}$ instead of Newton's second law. (The constant k_1 depends on the geometry and material properties of the two bodies.) The result is a formulation:

$$\begin{aligned} f(t) &= f_{\max}\sin(\pi t / t_c)^{3/2} && 0 \le |t| \le t_c \\ f(t) &= 0 && \text{otherwise} \end{aligned}, \tag{3.4}$$

where the maximum force is

$$f_{\max} = 1.917\rho_1^{3/5}\left(\delta_1+\delta_2\right)^{-2/5} R_1^2 v_0^{6/5}. \tag{3.5}$$

This force pulse is inserted into Equation 3.1 to produce theoretical estimates of displacements, and it is central to estimates of the amount of energy contained in radiated stress waves (Hunter, 1957; Hutchings, 1979, Reed, 1985).

The two variations of the Hertz-derived force pulse are shown in Figure 3.3: the "half sine" pulse used by Hunter (Eq. 3.2), and the "$\sin^{3/2}$" pulse used by Reed (Eq. 3.4) (all normalized in amplitude). The magnitudes of the Fourier transforms of these pulses are plotted in Figure 3.3 (b) as a function of normalized frequency: $f_{norm} = f * t_c$. The shape of the spectral content of this source consists of a series of lobes separated by zeros, or frequencies void of spectral amplitude. The zero frequency which separates the main lobe from n^{th} side lobe can be expressed as $f_{zero,n} = A_n / t_c$ where A_n is a dimensionless number which depends on the shape of the pulse. $A_n = n+0.5$ for the "half sine" pulse, and $A_n = n+0.75$ for the "$\sin^{3/2}$" pulse.

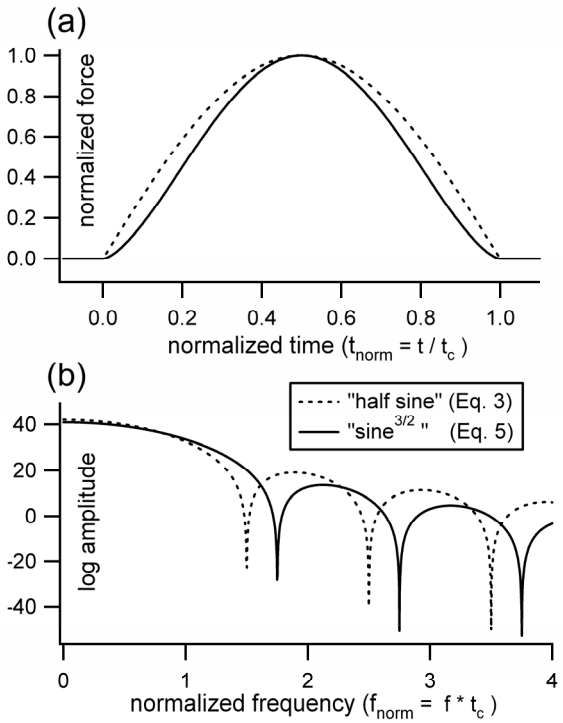

Figure 3.3. Two different formulations of the force pulse, both based on Hertzian contact theory. The "half sine" pulse was used by Hunter (1957) and is defined in Equation 3.2. The "$\sin^{3/2}$" pulse was used by Reed (1985) and is defined in Equation 3.4). Subtle differences in the shape of the pulses (a), are manifested as differences in the spectral content (b). The differences in the locations of zeros in the spectral content are used for quantitative evaluation.

3.2.3. Sensors and the instrument response function

Piezoelectric sensors were used because of their superior sensitivity compared to capacitive transducers (Breckenridge and Greenspan, 1981) and optical methods (Boltz and Fortunko, 1995) and because of the relative ease with which they can be mounted to a specimen as part of a sensor array. While most piezoelectric transducers take advantage of some mechanical resonance to gain high sensitivity at the expense of loss of bandwidth and signal distortion, the sensors used in this study, which are manufactured in our laboratory, are based on a design developed in the late 1970s intended to provide a more faithful transduction of surface displacement (Proctor, 1982; Greenspan, 1987).

The sensors contain a PZT-5a (lead-zirconium-titanate composition) truncated cone sensing element. The one part of the sensor in contact with the specimen is the 1.75 mm diameter truncated tip of the conical PZT element which is covered by a thin brass shim (which completes the electrical circuit, and enhances the mechanical bond with the specimen). The sensor is pressed onto the surface of the specimen with a mounting force of about 10 N. Sensitivity greater than many resonant sensors is made possible by the incorporation of an impedance matching JFET driver circuit located adjacent to the base of the PZT cone. This avoids signal loss due to parasitic capacitance. More details on the sensor design are described in Glaser et al., (1998).

Conical piezoelectric sensors are reported to have an extremely flat response between 100 kHz and 1MHz (e.g. Scruby et al., 1986; Proctor, 1982), but because these are contact sensors, the actual response is a function of the impedance match between the sensor and

specimen (Breckenridge et al., 1975), causing difficulties in the sensor's absolute calibration. Until now, the calibration of a sensor coupled to a number of different materials has been only briefly studied (Eitzen and Breckenridge, 1987). Following the transfer function approach of Chapter 2, the sensor output, s(t), is expressed as the linear convolution of the surface displacement and the sensor's instrument response function:

$$s(t) = u_3(t) \otimes i(t) . \tag{3.6}$$

where $u_3(t)$ is the displacement normal to the surface of the specimen at the sensor location x which would exist in the absence of the sensor (estimated from Equation 3.1). The complex transfer function of the transducer $I(\omega) = S(\omega)U_3(\omega)^{-1}$ can be found from inversion of the Fourier transform of Equation 3.6. The sensor response $I(\omega) = \beta \cdot I_{norm}(\omega))$, where $I_{norm}(\omega)$ is the shape of the frequency response, and β is the absolute sensitivity given a specific $I_{norm}(\omega)$.

Once the transducer response function and Green's function of the plate material/source-sensor orientation have been determined, these effects can be removed from recorded signals through inversion. This inverse problem is solved in the frequency domain by directly dividing Fourier frequencies, or in the time domain using a least squares deconvolution strategy (Michaels, 1982; Yilmaz, 1987). Both methods were used in this study, and the accuracy of the inversion is discussed in Section 3.4.2.

3.3 Experiments

Three collections of experiments were performed on the four plates described in Table I. For all tests, the setup was identical to that shown in Figure 3.1, except that the ball source was in some cases replaced by a capillary fracture. The glass and PMMA plates were left in "as received" condition while the steel and aluminum plates were polished to a mirror finish. The output from each sensor was recorded at 10 MHz and 14-bit dynamic range. For spectral estimates, recorded signals were windowed with a Blackman-Harris window centered on the first wave arrival and transformed using a fast Fourier transform algorithm. The length of the window varied for different plate materials but was always less than $2*t_{max}$.

For the calibration tests, five capillary fracture tests were performed on each plate specimen and the force at which fracture occurred was independently measured with a force sensor. Five ball-drop tests using small (0.40 mm and 0.50 mm diameter) ruby balls were also performed. To separate sensor response from source-receiver geometry, one of the sensors in Position 2 was switched with the sensor in Position 1, and the sets of five capillary tests and five ball drops were repeated.

In the second collection of experiments, sets of ball-drop tests were performed using hardened steel balls and ruby balls of 1.00 mm and 2.38 mm in diameter and glass balls of 1.00 mm and 2.5 mm in diameter, at three different drop heights: 0.068 m, 0.127 m, and 0.315 m. For each test, a ball was dropped from a platform of known height, allowed to fall through the air, strike the plate, rebound, and then strike the plate again; this procedure was repeated ten times for each of the selected combinations of drop height, ball size, and ball/plate materials. Signals were recorded for 1.6 ms surrounding the first arrival of the elastic waves produced by the initial collision of the ball on the plate, and for 105 ms surrounding the expected time of the second bounce of the ball on the plate. The incoming velocity of the initial collision was calculated from

the known height of the ball drop while the rebound velocity of the same collision was calculated from the time between successive bounces (Bernstein, 1977; Falcon et al., 1998).

For the third set of tests, 1.0, 2.38 and 2.5 mm balls were dropped from a wide range of heights (1 mm to 1 m) and allowed to bounce repeatedly (tens of times in succession). Stress wave information over the entire time period was recorded at a reduced sampling rate (500 kHz), and the first wave arrival (determined to +/- 2 μs) from each successive impact was used for *e* calculations (following Bernstein, 1977; and Falcon et al., 1998).

3.4 Results

3.4.1 F_{zero} results

The frequencies associated with the zeros in the power spectrum of recorded signals ($f_{zero,1}$, $f_{zero,2}$, and $f_{zero,3}$) were estimated from local minima found in the magnitude of the Fourier transform of signals recorded from the sensors in Position 2. (Position 2 produced a higher signal to noise ration than Position 1.) An example of an impact signal, produced from the collision of a 1.00 mm steel ball dropped 325 mm onto the aluminum plate, is presented in Figure 3.4 (a) along with the surface normal displacements predicted by theory (Equation 3.4 inserted into Equation 3.1). Based on this rough comparison of the two signals, we can estimate that the transducer sensitivity is approximately 250 mV/nm, and the noise is approximately +/- 0.25 mV (+/- 1 pm). The magnitude of the Fourier transform of the recorded signals and theoretical displacements are plotted in Figure 3.4 (b) along with the power spectrum of an exemplary noise signal from the experimental setup.

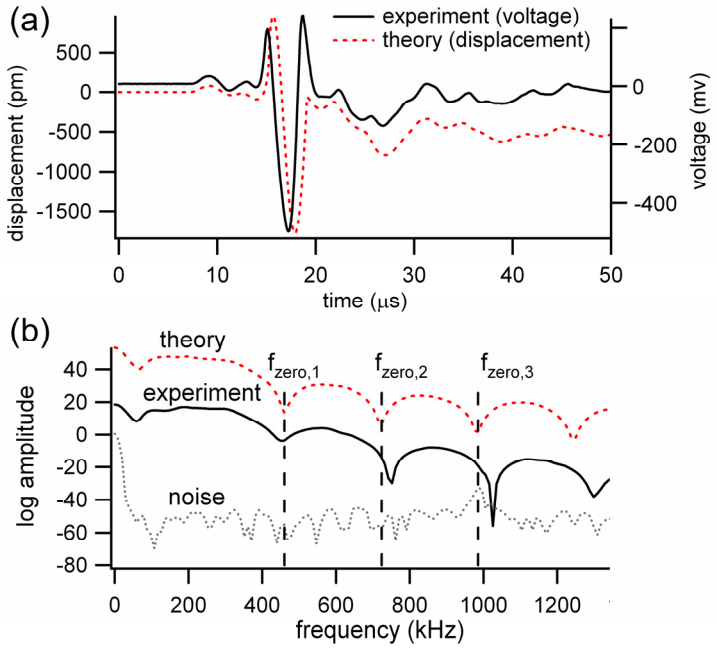

Figure 3.4. Comparison between theory (using the "$\sin^{3/2}$" Hertzian force pulse, Eq. 3.4) and experiment for a 1.00 mm steel ball dropped 315 mm onto a thick aluminum plate. Subtle differences between experiment and theory can be identified by the different locations of zeros in the frequency spectra in (b).

The results for $f_{zero,1}$, $f_{zero,2}$, and $f_{zero,3}$ for all material combinations are plotted in Figure 3.5 on a nondimensionalized frequency scale which is normalized to t_c, found from Equation 3.3. The expected f_{zero} locations for the "$\sin^{3/2}$" force pulse are shown as vertical dashed lines for reference. The observed f_{zero} locations strongly favor the "$\sin^{3/2}$" force pulse formulation over the "half sine" pulse described in Section 3.2.2, thus validating the Reed (1985) correction to Hunter's (1957) theory. This quantitative evaluation of the force pulse does not rely on an accurate calibration of the sensors. Note that the results for ruby and steel balls colliding with the steel and aluminum plates produce slightly low $f_{zero,1}$, and slightly high $f_{zero,2}$, and $f_{zero,3}$, while the collisions on glass and PMMA plates are more consistent with theory (these deviations are discussed in Section 3.5.2).

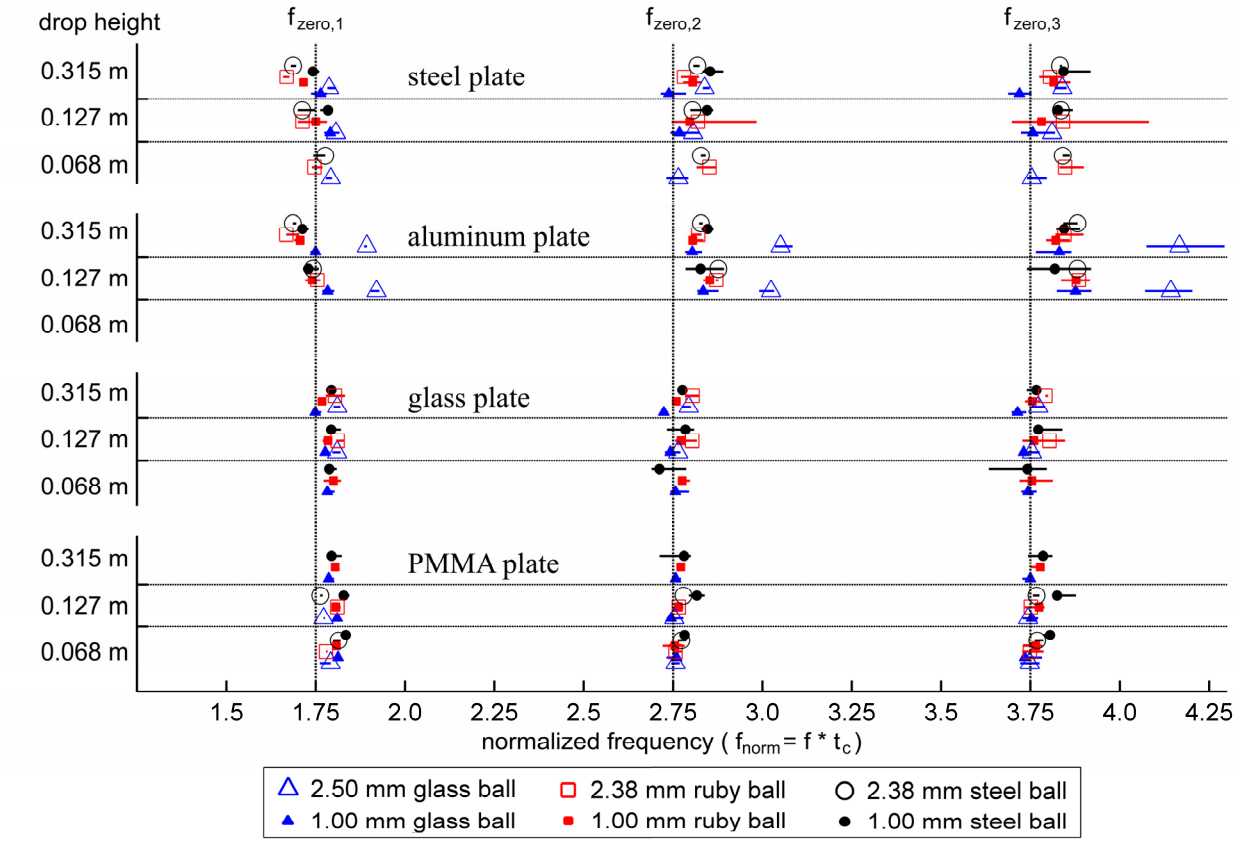

Figure 3.5. The frequencies of the first three zeros ($f_{zero,1}$, $f_{zero,2}$, and $f_{zero,3}$), found from local minima in the power spectra of recorded signals, are plotted against a nondimensionalized frequency parameter. The vertical grid lines correspond to expected f_{zero} frequencies based on a $\sin^{3/2}$ force pulse formulation derived from Hertz theory (Equation 3.4). The symbol locations indicate the median frequency for each set of ten ball-drop tests while the horizontal error bar extends from the first to the third quartiles of the set of ten tests.

3.4.2 Calibration tests

Calibration experiments were performed on all four of the plate materials, and the instrument response function, $I(\omega)$, of the Glaser-type sensor was estimated by following the sensor calibration procedures described in Chapter 2. The amplitude and phase of estimates of $I(\omega)$ of are shown in Figure 3.6 for both ball drop and glass capillary fracture calibration tests on

each test plate. The results from the four different plate materials are offset for clarity, and are shown only in frequency ranges for which a signal to noise ratio of at least 20 dB was attained.

Subtle variation was observed in instrument response between different sensors, but in all cases the underlying amplitude and phase spectra of the instrument response were found to be smooth and flat enough to make its removal via deconvolution a relatively straightforward affair. The results presented in Figure 3.6 show that the general shape of the instrument response ($I_{norm}(\omega)$) is unchanged (to within +/-3 dB) when coupled to the four different plate materials. The sensor calibration results from Position 1 are shown for PMMA (because aperture effects were non-negligible in Position 2), while the results for Position 2 are shown for the other three materials. The roughness in both the amplitude and phase response (especially apparent in the PMMA trace) is due to a slight mismatch between the Green's function estimates and the actual impulse responses of the plates. Other than increased spectrum roughness, calibration results for steel, aluminum, and glass obtained from sensor Position 1 did not differ appreciably (no more than +/- 3dB) from those obtained from Position 2. The level of agreement between ball-source and capillary-source sensor calibrations illustrates that either of these sources can be successfully used for sensor calibration purposes, but the divergence at high frequencies between the ball and capillary test results establishes a bound on the reliability of both the capillary fracture model (step function) and the Hertzian impact model (Eq. 3.4).

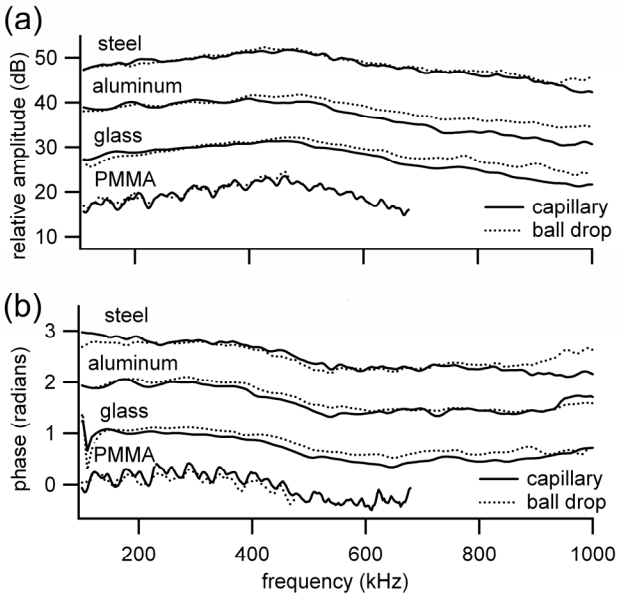

Figure 3.6. The amplitude, (a), and phase, (b), estimates of the instrument response function of one of the conical piezoelectric sensors coupled to the four different test plates (each one offset for clarity) over a frequency range of 100 kHz to 1 MHz. Each line is the average of 3 to 5 calibration tests—either ball drops or capillary fractures (outliers were removed). Note that the roughness in both the amplitude and phase (especially apparent in the PMMA trace) is due to a slight mismatch between the Green's function estimates and the actual impulse responses of the plates.

The absolute sensitivity of the sensor, β, was found to be, on average, about 15 dB less sensitive when coupled to PMMA (45 mV/nm) than when coupled to the steel, aluminum, and glass plates (250 mV/nm). This result is consistent with Eitzen and Breckenridge (1987) and is attributed to the lower acoustic impedance of PMMA. Sensor sensitivity was, on average, 200-

250 mV/nm when coupled to glass, aluminum, and steel, and about 45 mV/nm when coupled to PMMA.

In addition to being affected by acoustic impedance of specimen to which the sensor is coupled, β is also affected by the physical bond between the sensor tip and the specimen. This physical bond is in turn affected by the presence of a mounting couplant, the force at which the sensor is pressed against the test sample, and even time that the sensor remains in contact with the test specimen. Consequently, β sometimes varied by as much as a factor of 2, even on a single material.

The removal of the Green's function by inversion was much more difficult and prone to error than that of the instrument response function because the Green's function is not minimum phase, has an infinite impulse response, and its amplitude and phase spectra are not smooth (as shown in Figure 3.2 (c)). Difficulties in this inversion process are well known (e.g. Ching et al., 2004; Micheals et al., 1981), and errors are manifested as "overshoots" and "aftershocks" to the calculated force pulses such as those shown in Figure 3.8b.

3.4.3 Impulse and force pulse

The impulse P that the ball imparts to the plate (equal to the ball's change in momentum) is defined as the time integral of the force pulse

$$P = \int f_3(t)dt = m_1 \left| v_f - v_0 \right| \tag{3.7}$$

where v_0 is the incoming velocity, v_f is the rebound velocity, and m_1 is the mass of the ball. The force pulse can be found from the inversion of recorded signals, but to circumvent the aforementioned difficulties involved in the removal of the Green's function through deconvolution, the following approximation is made. For force pulses $f_3(t)$ which are of short duration compared to t_w, the impulse can be well approximated by integrating Equation 3.1 over time:

$$\int f_3(t)dt \cong \gamma^{-1} \int_{t_n=0}^{t_n=3} u_3(t)dt \,, \tag{3.8}$$

where

$$\gamma = \int_{t_n=0}^{t_n=3} g_{33}(t)dt \tag{3.9}$$

is a constant which depends only on the Green's function for a given plate material, sensor location and $t_n = t/t_w$. In Equation 3.8, displacements $u_3(t)$ are estimated by removing the instrument response $i(t)$ from recorded signals.

In Figure 3.7, the impulse that the ball delivers to the plate, is graphed against the ball's change in momentum. The impulse is calculated from radiated stress wave measurements (Eq. 3.8), while the ball's changing in momentum is calculated from v_0 and v_f estimated from the timing of ball bounces (Eq. 3.7). Each group of points corresponds to a set of ten ball drops performed under the same conditions. Figure 3.7b shows the same data at greater magnification. There is a linear proportionality between impulse calculated from stress waves and change in

momentum observed from incoming and rebound velocities of the ball. The slope of the resulting trend line is equal to the sensor sensitivity β relative to the sensitivity assumed for the impulse calculation (which was 1 V/nm). All of the data lies within +/- 0.5 dB of the β = -14 dB and β = -29 dB lines shown, even for abnormally low *e* collisions such as that shown in Figure 3.7b inset. This comparison serves a means of double checking the absolute sensor sensitivity β over a wide range of amplitudes. (Note that the sensor is 15dB more sensitive when coupled to steel than when coupled to PMMA.)

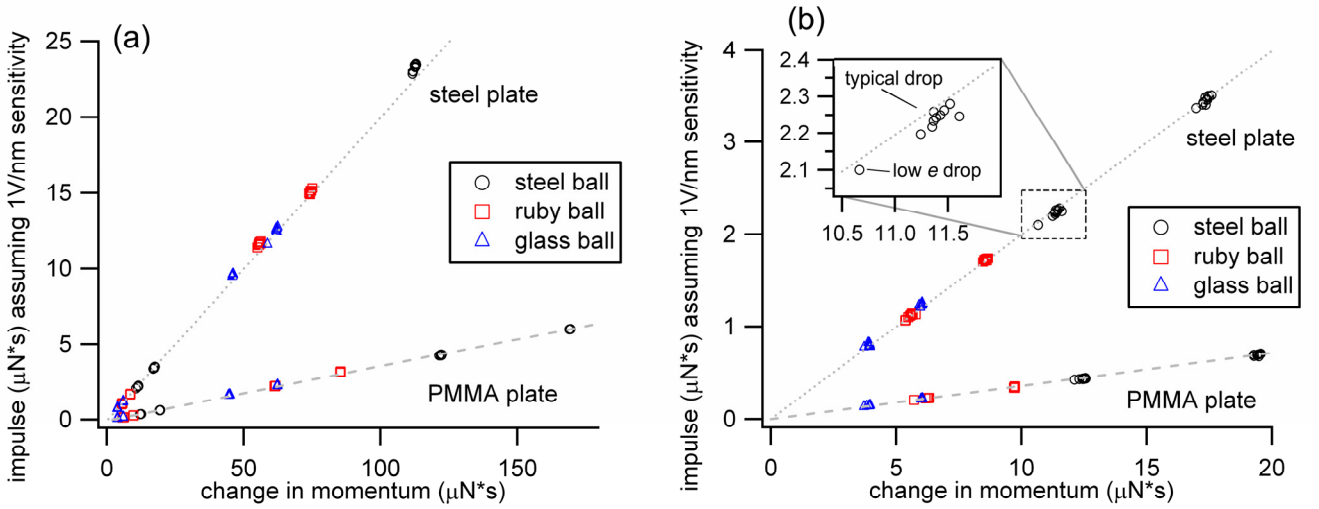

Figure 3.7. The proportionality between stress waves and the ball's change in momentum is illustrated for 1-2.5 mm diameter balls of various materials striking thick steel and PMMA plates (a). The results for the 1 mm diamater balls are shown at greater magnification (b). The results from the ten tests of 1 mm steel balls dropped 127mm onto the steel plate are shown in more detail in the inset.

The coefficient of restitution (*e*) is defined as the ratio of the magnitudes of the rebound and approach velocities of the ball. Each set of ball drop tests showed some variability in measured *e*, but a few of the collisions showed *e* markedly lower than the others, with subtle differences in the shape of the force pulse. A well-pronounced example of this aberration is illustrated in Figure 3.8 for the case of a 1.00 mm diameter steel ball dropped 127 mm onto the steel plate, but similar results were observed for all types of ball and plate materials tested.

Figure 3.8 illustrates the differences in signals recorded for the bounces with large variability in *e*. The signals shown in Figure 3.8 correspond to the same data plotted in Figure 3.7b inset. In Figure 3.8a, the instrument response function *i(t)* has been removed from the raw experimental data and resulting displacement time histories are plotted along side synthetic data (obtained by inserting Equation 3.4 into Equation 3.1). The force pulses shown in Figure 3.7 (b) were found by removing both the instrument response function and the Green's function (shown in Figure 3.2 (a)) from the recorded signals. Of the data from the ten ball drop tests performed under these conditions, nine of them (the cluster in Figure 3.7(b) inset) are very similar to that of the "typical drop" plotted in Figure 3.8. The remaining outlier labeled "low *e* drop" is plotted for comparison. The somewhat-lower-than-average amplitude and small precursory force which precedes the first main wave arrival are typical features of these low-restitution collisions and were observed by every sensor in the array.

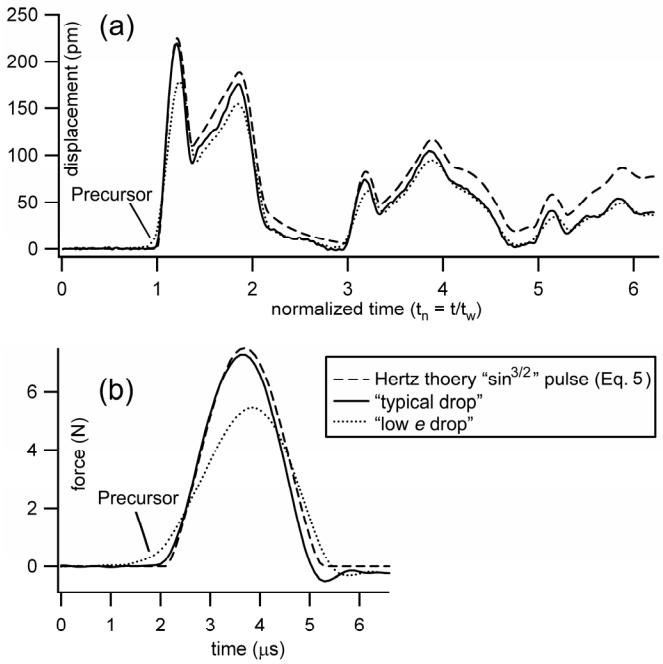

Figure 3.8. Normal displacements at sensor Position 1 (directly beneath the location of impact) due to the collision of a 1 mm steel ball dropped 127 mm onto a 50 mm thick steel plate. Small precursory forces which accompany low *e* collisions can be seen in both the wave amplitudes (a) and the force pulse (b) found from inversion.

3.4.4 Restitution tests

The results of the restitution tests for all plate materials are summarized in Figures 3.9 and 3.10. As previously described, incoming and rebound velocities of the ball were calculated from the time between successive bounces (as in Bernstein, 1977, and Falcon et al., 1998) which was determined from stress wave arrival information and contact times. In the absence of air resistance, the ball's rebound velocity after the i^{th} collision

$$v_f^i = g t_{air}^i/2 = v_0^{i+1}. \quad (3.10)$$

The total time the ball spends in the air between the i^{th} and $i+1^{th}$ collisions is

$$t_{air}^i = t_p^{i+1} - t_p^i - t_c^i. \quad (3.11)$$

In these equations, t_p^i is the arrival time of the direct P-wave radiated from the i^{th} collision, t_c^i is the contact time of the same collision, and g is acceleration due to gravity. Drag forces due to air resistance, estimated using a simple model of a sphere in a fluid (Schlichting, 1979), were also incorporated into the calculation of incoming and rebound velocities. Based on this model, errors in *e* estimates associated with air resistance are negligible for low velocities and increase to about 1% for smaller, less massive balls at higher velocities. For the presentation of Figures 9 and 10, data is grouped into logarithmically spaced bins on a velocity scale. Each symbol location denotes the median *e* from sets of at least four data points, and the vertical error bar extends from the first to the third quartiles of the data set. Note that the scale in Figure 3.9a and 3.9b is different from that in Figure 3.9c and 3.9d.

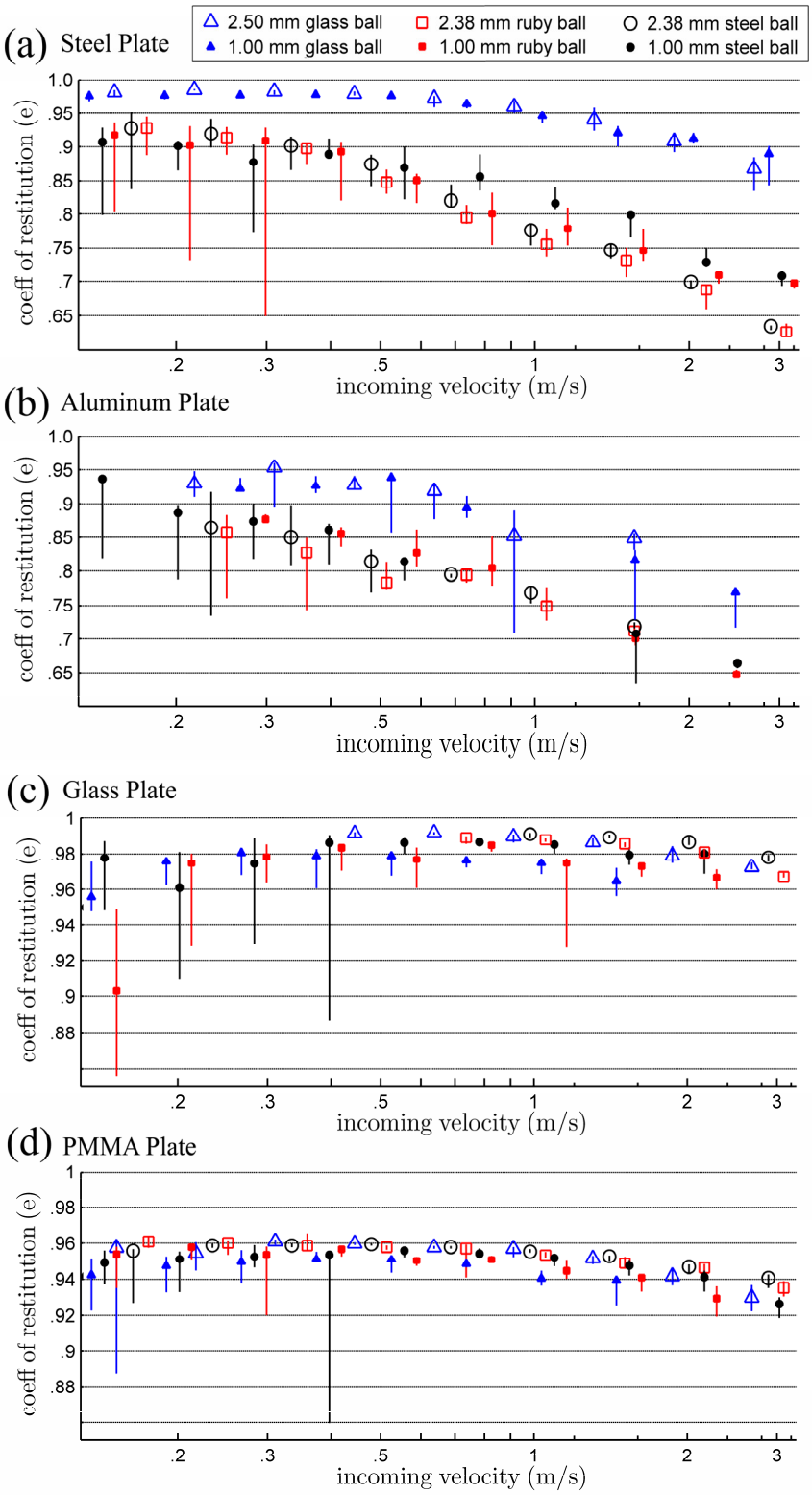

Figure 3.9. Coefficient of restitution (*e*) plotted against the log of incoming velocity for all ball and plate material combinations. Data is grouped into logarithmically spaced bins on a velocity scale. Each symbol location denotes the median *e* from sets of at least four data points, and the vertical error bar extends from the first to the third quartiles. Note that the scale in Figure 3.9 (a) and (b) is different from that in Figure 3.9 (c) and (d).

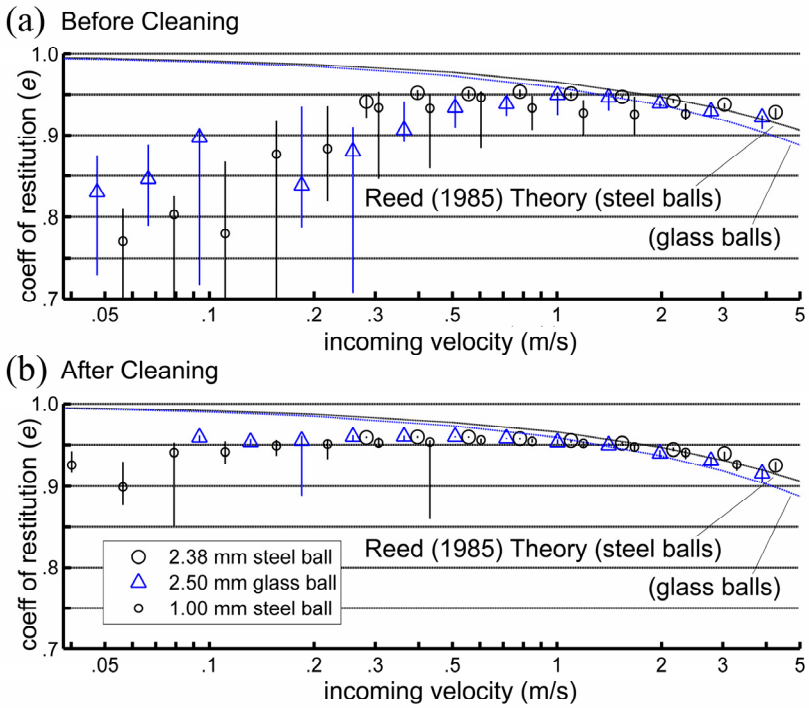

Figure 3.10. Coefficient of restitution measurements on PMMA: comparison before (a) and after (b) cleaning the balls with acetone and isopropyl alcohol.

3.5 Discussion

3.5.1 Momentum and energy

The comparison between the force pulse and *e* highlights the fundamental distinction between momentum and energy, and how each relates to radiated stress waves. The force pulse describes the ball's change in momentum, which is conserved, while *e* relates to the efficiency of kinetic energy transfer. In general, even when *e* results indicated that a large amount of the ball's kinetic energy was consumed during the collision, the stress wave signature remained largely unaffected. This reinforces the ball impact as reliable source of stress waves despite energy-related deviations from Hertzian theory. Figure 3.7 shows the direct proportionality between the ball's change in momentum and stress waves, even for low *e* collisions. Kinetic energy lost to anelastic processes—and radiated stress waves themselves—during the collision only result in a small reduction in the ball's change in momentum, and therefore, a small reduction in the amplitude of the radiated stress waves, but the measured frequency content of the waves will remain largely unchanged. For the case of the "low restitution drop" shown in Figure 3.7b inset and Figure 3.8, over half of the ball's kinetic energy was absorbed during the collision, yet the resulting stress wave signature is not drastically different from that of the Hertz-derived theory, which does not account for any energy loss at all. The only clues in the stress wave signature which indicate that an inelastic collision has taken place are the subtle changes in the ball's momentum transfer, such as the small precursory force, slight asymmetry, and approximately 20% reduction in amplitude of the force pulse.

The following example demonstrates the non-intuitive relationship between energy, momentum, and stress waves:

Consider a ball impacting a massive plate at an approach velocity of 1 m/s. In one case, the ball collides elastically and rebounds at -0.99 m/s, and 98 percent of its kinetic energy is retained. The results shown in Figure 3.7 show that radiated stress waves are proportional to force the ball imposes on the plate which is proportional to the ball's change in velocity—in this case, 1.99 m/s. In second collision, the ball, with an identical approach velocity of 1 m/s, hits a piece of dust on the surface of the plate, which absorbs some kinetic energy and causes the ball to rebound at only -0.71 m/s (50% of its kinetic energy). The radiated stress waves from this collision are proportional to 1.71 m/s. When comparing the first collision to the second, the ratio of kinetic energy consumed is 4:100 while the ratio of stress wave amplitudes is 100:86. Stronger stress waves were radiated when *less* kinetic energy was consumed.

This example emphasizes the difficulties of studying energy-related seismic-source phenomena via radiated stress waves. Impulse (change in momentum) rather than the energy of radiated stress waves is the physical quantity which best describes "strength" of the source.

For collisions at moderate velocities ($v_0 \sim 1$ m/s), the force pulse was adequately modeled by Hertzian theory even when permanent plastic deformation was observed. This observation is consistent with those of Tillet (1954) and Lifshitz and Kolsky (1964), who showed that the duration of contact, t_c, does not deviate appreciably from Hertzian theory, even for incoming velocities eight times greater than that at which plastic deformation is expected to commence. The location of zeros found in the spectral content of recorded stress waves shown in Figure 3.5 are very close to $f_{zero,n} = n+0.75$ which clearly supports the "$\sin^{3/2}$" force pulse of Equation 3.6 over the "half sine" pulse of Equation 3.2 (which would produce $f_{zero,n} = n+0.5$).

3.5.2 Plastic deformation

Local plastic deformation, tiny (~100 μm) dents left in the plate material, was optically observed for collisions on the steel and aluminum plates. The occurrence of energy-consuming plastic deformation was also characterized by a sharp decrease in *e* with increasing v_0, shown in Figure 3.9 (a) and (b). More subtle indications of gross yielding include a slight asymmetry and lower-than-expected amplitude of the force pulse and minor spectral changes in radiated stress waves such as a reduction in $f_{zero,1}$, and an increase in $f_{zero,2}$ and $f_{zero,3}$. The collisions of glass balls on the steel plate were considerably more elastic than those of ruby and steel balls on the steel plate. This result was expected from Hertz theory because the glass balls are less massive (which causes the maximum impact force to be lower) and more compliant (which causes the force to be distributed over a larger contact area). The spectral properties of the collisions of the 2.5 mm glass balls on the aluminum plate were inconsistent with previously mentioned trends.

For the collisions of all the balls on the glass and PMMA plates, measured *e* values were much closer to Hertzian-derived predictions, and the subtle indications of gross plastic deformation described in the previous paragraph were absent. Even though the yield stress of PMMA is lower than that of steel and aluminum, the compliance of this plate material produces a larger area of contact and a longer contact duration, which reduces the maximum stresses developed during the collision.

Counter to the prediction by Hutchings (1979), even when a significant amount of plastic deformation occurred during a collision (as evidence by $e \sim 0.7$), the asymmetry of the force pulse was found to be minor. The lack of asymmetry of the force pulse and its general insensitivity to plastic yielding are likely due to strain rate effects. Also mentioned in Hutchings (1977) and Goldsmith and Lyman (1960), the rate of loading and unloading during the collision

of a small ball on a massive body is so great that there simply isn't enough time for plastic deformation to fully develop, and stresses in excess of the yield stress may exist for a short period of time. The loading rate is faster for smaller balls than larger ones. This extremely rapid loading rate is thought to be the reason why higher *e* was measured for the small balls than for the large ones, for collisions between steel and ruby balls on the steel plate, as shown in Figure 3.9a.

3.5.3 Surface effect

Surface properties such as roughness (Litshitz and Kolsky, 1964) and adhesion (e.g. Johnson and Greenwood, 1997) were previously suggested as a likely cause for energy loss during impact. In the current study, a "surface effect" was manifested as a decreased average value, and increase in scatter, in *e* measurements for very low v_0. This was observed for all ball and plate material combinations. Particularly low *e* collisions were accompanied by a tiny precursory force preceding the main force pulse. A very prominent example of this is shown in Figure 3.8. The duration and strength of this curious precursory force was well correlated to the decrease in *e*. From the duration of the precursory force and the incoming velocity of the ball, the spatial extent of the surface irregularity required to make the force was estimated to be 1 to 4 μm for the largest precursory forces observed. These estimates were consistent with observations of small particles on the surface of the balls when viewed under a microscope. As presented in Figure 3.10, surface effects were diminished when the balls were cleaned with acetone and isopropyl alcohol, and then dropped with a fine sponge. Despite this reduction, surface effects are a likely cause for the departure from theory (Reed, 1985) for low v_0 collisions shown in Figure 3.10 (b).

The observed surface effects suggest that as the two colliding bodies first begin to interact, before full mechanical contact has been formed in the Hertzian sense, roughness or surface imperfections such as grease or dust which may exist between the two surfaces are loaded and deformed, and this deformation saps some small amount of the ball's kinetic energy. For bodies with an abundance of kinetic energy and small contact areas, surface effects can be ignored, but for micro particles impacting real, unclean surfaces, these effects can be significant.

3.6 Conclusions

Recordings of radiated stress waves contain information about the source, propagation medium, and sensor. A set of experiments using multiple sources (ball and capillary), sensors, source-sensor orientations, and test blocks were designed so that the contributions from each of these factors could be systematically identified. The results of this study demonstrate that the impact of a small (1 to 2.5 mm diameter) ball on a suitably massive body is a repeatable and reliable source of stress waves in solid materials, even when moderate yielding of the plate material is observed. For collisions at moderate velocities (~ 1m/s), the stress wave signature can be well modeled by a "$\sin^{3/2}$" force pulse derived from Hertz contact theory (Eq. 3.4). This study shows that the ball impact source can serve as an effective complement to glass capillary fracture due to its repeatability, predictability, and the ease at which the frequency content and amplitude of the introduced waves can be modified simply by changing the incoming velocity, size and material of the impinging ball.

Radiated stress waves were found to be linearly proportional to the change of the ball's momentum, even when simultaneous measurements of the ball's coefficient of restitution (*e*) indicated that a large amount of the ball's initial kinetic energy was consumed by non-conservative processes such as plastic deformation of the plate material. This result suggests that the impulse rather than the energy of radiated stress waves is the physical quantity which best describes "strength" of the source. This has long been known in seismology where the strength of an earthquake is judged by its seismic moment; energy remains an elusive parameter.

This study emphasizes that stress wave recordings could not be used to measure kinetic energy consumption directly. Instead, phenomena such as plasticity and surface effects were only identified by subtle changes in the calculated force pulse. Plastic yielding in the steel and aluminum plates was marked by a very slight asymmetry of the force pulse and slight changes in the spectral content of radiated stress waves, but these effects were minor, likely muted by strain rate effects. Plastic yielding may play a more important role during the collision of a larger ball with a longer duration of contact.

Variability in the coefficient of restitution was found to be a function of surface cleanliness; force-time pulses recorded from collisions with an abnormally low *e* were marked by a tiny precursory force. This measurable precursory force is the force of the ball pressing against dust or μm scale roughness of the ball or plate surfaces immediately prior to full Hertzian contact between the two bodies. This dust or μm scale roughness is inelastically deformed which results in a collision with abnormally low *e*.

The frequency response $I_{norm}(\omega)$ of the conical piezoelectric sensors used in this study was found to be unchanged (to within +/- 3dB) when coupled to the four different plate materials, with the differences easily removed by deconvolution due to the smoothness of its amplitude and phase spectra (there were no apparent poles or zeros). Consequently, measurements of high frequency surface displacements down to a few pm in amplitude could be attained. The absolute sensitivity, β, of the sensors was found to vary by a factor of two and is dependent on the mechanical bond between the sensor tip and specimen, which emphasizes the need for a repeatable calibration source such as ball impact which delivers waves of a known amplitude and frequency content into a solid body.

Chapter 4

Drying Shrinkage Cracking in Concrete

4.1 Introduction

Fresh concrete is initially saturated, but when exposed to an environment with less then 100 percent humidity, the gradual loss of physically adsorbed water from the compounds which compose the cement paste causes the paste to shrink (Mehta and Monteiro, 2006). Drying shrinkage of concrete is a known cause of both micro and macro cracking. Cracks increase the permeability of concrete, which can allow water to penetrate into the material, and can lead to sulfate attack, alkali silica reaction, or the corrosion of reinforcing steel. Also, the presence of micro cracks lowers the toughness of the concrete. Though aggregates complicate the stress state of a shrinking concrete specimen (Grasley and Lange, 2004), cracking is expected to occur in the region of tensile stresses near the outside surface of the specimen (Bisschop, 2002).

Most research on drying shrinkage cracking in concrete relies on observations via optical microscopy (Bisschop and van Mier, 2002). These studies have confirmed that the location of drying shrinkage cracking is near the surface and around aggregates, and occurs predominantly during the first few days of drying (Bisschop and van Mier 2002). The disadvantage of these optical methods is that they require cutting open the specimen. Using the analysis of stress waves radiated from crack growth, drying shrinkage cracking can be studied continuously and non-invasively (Uomoto and Kato, 1990; Shiotani et al. 2003). In this chapter, the cracking of concrete due to drying shrinkage without external restraint is studied by means of passive monitoring of stress waves, commonly known as the method of acoustic emission. We locate cracks in three dimensions over a 17-day drying period. Additionally, the sources of error in the source localization methods are identified and quantified and error ellipsoids are calculated for each of the source location estimates.

4.2 Experimental setup

This chapter describes the testing of a prismatic specimen (175 x 175 x 250 mm) of normal strength concrete with a water/cement ratio of 0.46, design strength of 27.5 MPa, and largest-sized coarse aggregate of 15 mm diameter (pea gravel). The specimen was cast into a wooden mold with PMMA inserts for improved surface smoothness. The specimen was cured for 28 hours and then demoulded and instrumented with an array of Glaser-type sensors. As shown in Chapters 2 and 3, the sensors have a very flat frequency response from 100 kHz to 1 MHz and with unidirectional sensitivity to particle displacement.

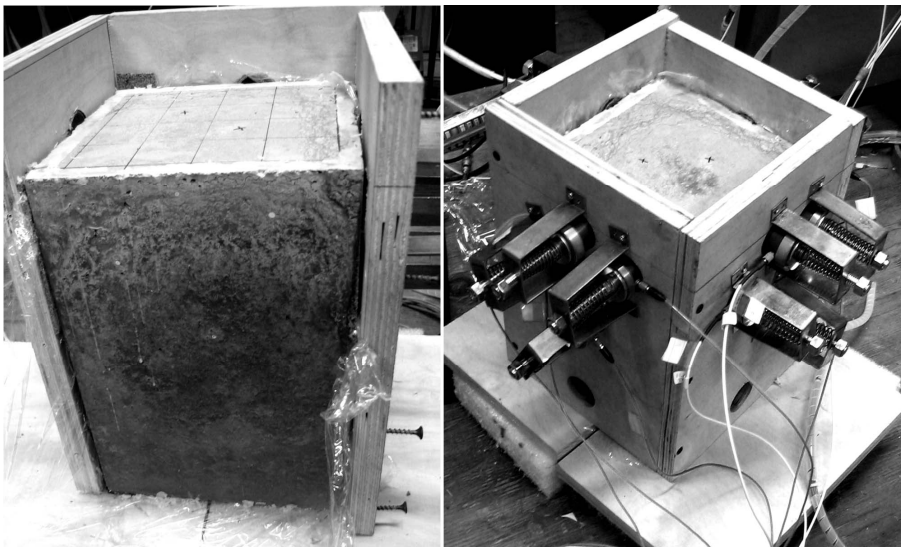

Fig. 4.1. An array of 14 sensors is pressed against the sides of a concrete specimen with springs. Over a 17 day monitoring period, the top surface of the specimen is exposed to ambient humidity while the sensor array waits for a micro crack to trigger the recording system.

The prismatic specimen, described in Figure 4.1, was instrumented with an array of fourteen sensors located on the North, East, South, and West sides of the specimen. (Sensor locations are shown in Figures 4.2-4.5.) The top side of the specimen was exposed to ambient humidity (30% relative humidity, plus or minus five percent) and the rest of the specimen was partially sealed with cellophane. Before digitization, all signals were preamplified by a DigitalWave^{TM} FM-1 signal conditioner, with a gain of 42 dB and a 20 kHz high pass filter to remove low frequency background noise. The signals were sampled at 5 MHz using a 12-bit High-Techniques Digitizer. The specimen was continuously monitored for seventeen days. Four sensors were selected as trigger sensors. If, at any time during the seventeen day monitoring period, the voltage output from any of those four sensors exceeded the arbitrary trigger level of 31 mV (corresponding to displacements on the order of 3 pm), the output from all 14 sensors was recorded with the digitizer. Signal length encompassed 800 μs of the displacement time history with a pre-trigger length of 250 μs. Each one of these triggered 'hits' was saved for offline analysis and was later classified either as an 'event' or as 'noise'.

4.3 Estimating the location of stress wave sources

An accurate estimation of the source location is extremely important because further analyses of source characteristics assume that source location is known. There are a number of methods for determining a source location, but this chapter discusses only methods which use the observed arrival time of a specific wave phase at a number of sensor locations to calculate the coordinates of the source in space and time. The chosen method uses the P-wave phase because it is typically the easiest to identify from recorded signals. The same schemes can be implemented for S waves. An alternate source location strategy, which uses beam-forming, is discussed by McLaskey and Glaser (2010).

Finding the source location in space and time based on the differences in arrival times recorded from an array of n sensors requires the solution of a series of n-1 nonlinear equations

(Mahajan and Walworth, 2001). In our tests, the stress wave source locations were estimated by minimizing the cost function:

$$\text{cost} = \sum_{i=1}^{n} \left| \sqrt{(x - \mathrm{x_i})^2 + (y - y_i)^2 + (z - z_i)^2} - c(t_i - t_0) \right|, \qquad (4.1)$$

where t_i, x_i, y_i, and z_i are the observed P-wave arrival times, and the known spatial coordinates for the i^{th} sensor, c is the assumed wave velocity, n is the number of sensors used for the determination of the source location, and x, y, z, and t_0 are the unknown source location in three spatial dimensions and time. This method assumes (1) that the source and sensor locations can be modeled as points, (2) that the ray path from source to receiver is a straight line, and (3) that P waves travel at some known and constant velocity c.

Once an estimate of the source location is made, the quantification of uncertainty and bias in the estimate must be considered. In this study, the sources of errors were divided into four main categories: picking errors, array geometry-induced errors, velocity model errors, and minimization errors. All results presented here are for the array and specimen geometry shown in Figures 4.2-4.5.

4.3.1 Picking errors

Picking errors are those which can be modeled by an inaccurate selection of the arrival time of the P-wave. Slow rise times or low signal-to-noise ratios can cause picking errors, but even if the arrival times are unambiguous, the observed arrival time may deviate from the ideal case. Equivalent picking errors may be calculated and quantified for these sources of error.

The majority of the events recorded from the drying shrinkage test have P-wave rise times of 1-3 μs which allow the arrivals to be picked to within an accuracy of about 500 ns. This provides a baseline from which other sources of picking error can be quantitatively compared. For example, the 1.5-mm aperture of the current sensor would produce an equivalent of ≤ 170 ns of error, given the P wave velocities found in concrete. In contrast, an 8-mm diameter sensor aperture can produce up to 800 ns of equivalent picking error. The increase in travel path due to a crack or void 3 mm in diameter would produce ≤ 80 ns of equivalent picking error under the geometry of our test setup. Alternatively, under the same geometry, if the average P-wave velocity deviates (due to inhomogeneities in the material, for example) from the assumed value by only 5% (200 m/s) it would produce 500 ns of equivalent error.

In order to model picking errors and gain an estimate of the uncertainty associated with each source location estimate, a random error term was added to each arrival time picked from signals recorded with the Glaser-type sensors. This error term was assumed to be a normally distributed random variable with a mean of zero and a standard deviation of 500 ns. A source location estimate was then made, drawing upon fifty different realizations of the error terms. Error ellipsoids and confidence intervals were calculated from the cluster of fifty source locations generated via this procedure.

4.3.2 Array geometry errors

While the array geometry does not introduce new errors, for certain source locations relative to the sensor array the picking errors can be amplified by array effects (Salamon and Wiebols, 1974; Ge and Hardy, 1991). This is similar to the concept of a blind spot in the sensor array. Figure 4.2(a) shows the effect of the sensor array and specimen geometry used for the

drying shrinkage test setup. In the figure, the 95% confidence error ellipsoids due to array effects are shown relative to the true location of simulated sources located on the top surface of the concrete specimen. The error ellipsoids are based on normally distributed random picking error with a mean of zero and a standard deviation of 500 ns. It was found that array geometry-induced errors are greatest near the corners of the specimen, especially the Southwest corner.

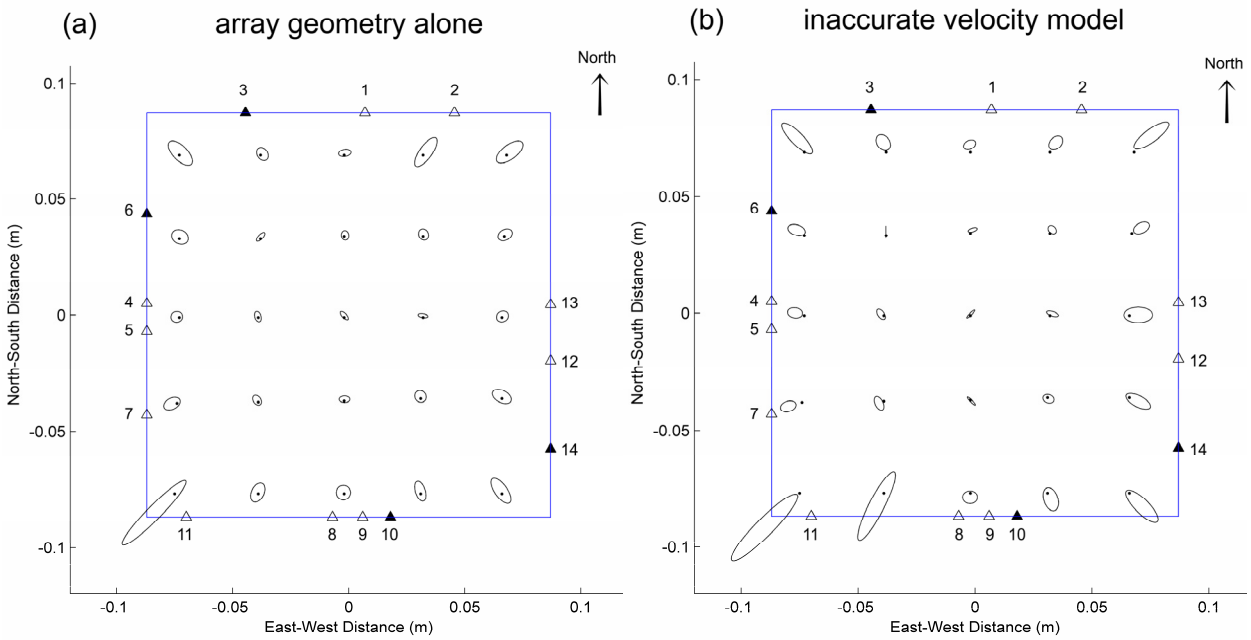

Fig. 4.2. Error ellipsoids for simulated sources located on the top surface of a specimen with identical array geometry to the drying shrinkage test setup demonstrate the amplification of picking errors due to (a) array geometry alone, and (b) bias induced by an inaccurate velocity model. The assumed P-wave velocity is 100 m/s faster than the true P-wave velocity.

4.3.3 Velocity model errors

The cost function (Eq. 4.1) used for localization assumes that the P-wave velocity is known and constant over every ray path in the concrete specimen, but in reality the P-wave velocity is unknown, difficult to measure, inhomogeneous, and is changing over time as the concrete cures and dries and cracks (Boyd and Ferraro, 2005). An incorrect velocity model will surely yield biased estimates of source location. For example, if the assumed velocity is only off by 100 m/s (about 3 percent) the source location estimate will be biased by 1-4 mm depending on the true source location relative to the sensor array. To illustrate velocity model errors, Figure 4.2(b) shows the combined effect of picking errors (same as described above), array geometry, and velocity model errors (the assumed velocity is 100 m/s faster than the true velocity). In some cases, this modest difference between the two velocity models causes an additional 10 mm of bias and a threefold increase in the uncertainty of source location estimates, even with the 14 sensor array. In general, the use of a velocity model which is too high will push location estimates further from the center of the sensor array.

4.3.4 Minimization errors

Array geometry-induced errors, picking errors, and velocity model errors can yield cost functions which lack a well-defined minima. Thus, there is a fourth category of errors, which arises due to the imprecision and bias introduced by the algorithm which minimizes the cost function. In the absence of errors, the cost function will vary smoothly over four dimensional space (three spatial dimensions and source time), but when deviations between observed and expected travel times are introduced, this function can become highly nonlinear. Iterative solution schemes often fail to find the global minimum and instead pick local minima or satisfy convergence criteria on a very flat portion of the solution surface, far from the true minimum. For this study, an iterative scheme which incorporates random jumps into the search path was used to minimize the cost function. This solution strategy was computationally expensive but very robust, out-performing conventional algorithms. By comparing different minimization schemes, imprecision was estimated to be on the order of 0.25-0.5 mm within the spatial region of interest.

4.4 Results and discussion

Over two thousand discrete stress wave sources were recorded within the prismatic specimen over the seventeen day monitoring period. About 800 events were deemed large enough to be located and rigorously analyzed. Reasonably accurate (+/- 10 mm) source locations were found for about 80 percent of those events.

4.4.1 Source locations

To account for change in P-wave velocity over time, pencil lead breaks (Hsu, 1977) were introduced at two different locations on the surface of the specimen on a daily basis. A velocity model was created based on the evolution of P-wave velocity estimated from the artificial sources and the assumption that the P wave velocity is initially increasing and then leveling off over the seventeen day period.

Figure 4.3 shows the principle axes of error ellipsoids for events which were found to be located near the center of the specimen (within the dashed lines), with 95% confidence error ellipsoid axes less then 5 mm in any direction. (Error ellipsoids were found from the method described above.) Of these 340 events, most were located a few centimeters below the drying surface. A smaller number of events were found to be much deeper (8-10 cm) in the interior of the specimen. The evolution of depth over the seventeen day monitoring period (for the same 340 events shown in Figure 4.3) is shown in Figure 4.4. The bars represent 95% confidence intervals of depth calculated via the same method used for Figure 4.3. The upper graph shows the locations found using a constant velocity model while the lower graph shows the results using a time varying velocity model.

One would expect that the drying shrinkage cracking would be spread evenly over the entire drying surface (top view, Figure 4.3) and be located within a few centimeters of the surface in front view (Figure 4.4) and side view (Figure 4.5). The relatively small number of events found in the SW corner of the specimen is likely due to the large amount of array-induced localization errors for this location, as shown in Figure 4.2. This causes any picking errors to be

amplified and will produce imprecise location estimates in this location, and the imprecise location estimates have been thrown out of this dataset. Alternatively, the larger numbers of events in the NW and SE corners of the specimen may be due in part to a triggering bias (i.e. smaller events closer to trigger sensors are recorded while similar events further from trigger sensors will be undetected). The four trigger sensors (#3,6,10,14) are shown as filled triangles in Figures 4.2-4.5.

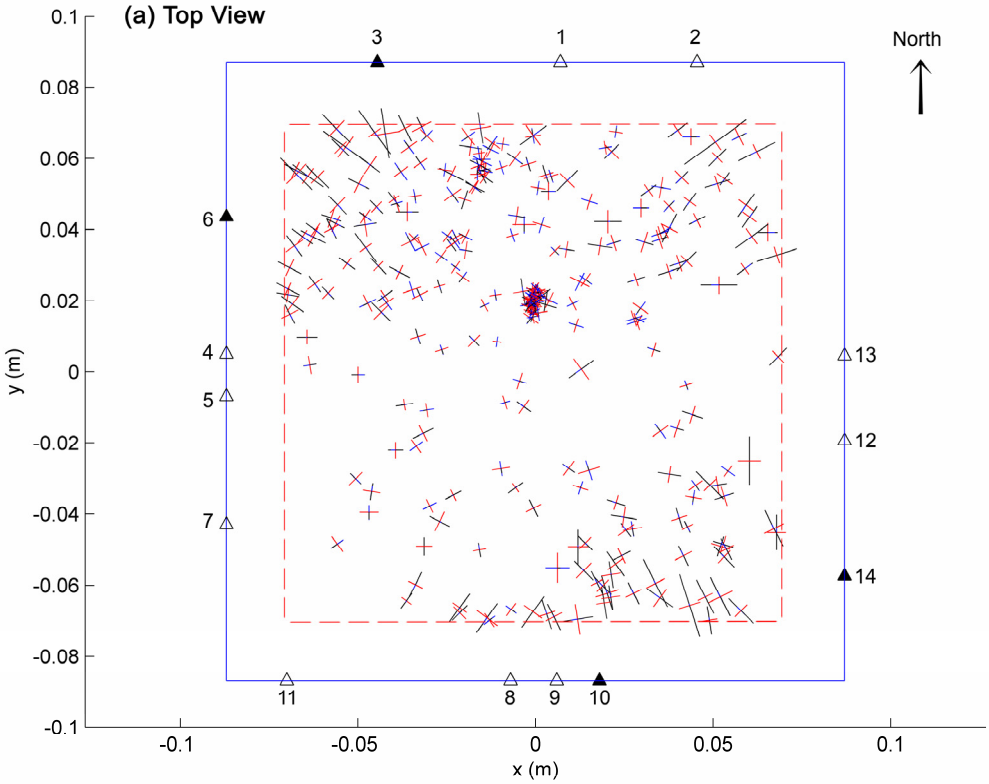

Figure 4.3. A top view of all 340 events located near the center of the specimen (within the dashed lines), with 95% confidence error ellipsoid axes less then 5 mm in any direction. The spatial distribution of estimated source locations shows many distributed events and a cluster of more than 20 events located close to the top surface, near the center of the specimen. The estimated source locations are marked by the principle axes of 95% error ellipsoids, as described in the text. Locations of the 14 sensors are represented with triangles. The four trigger sensors are filled triangles.

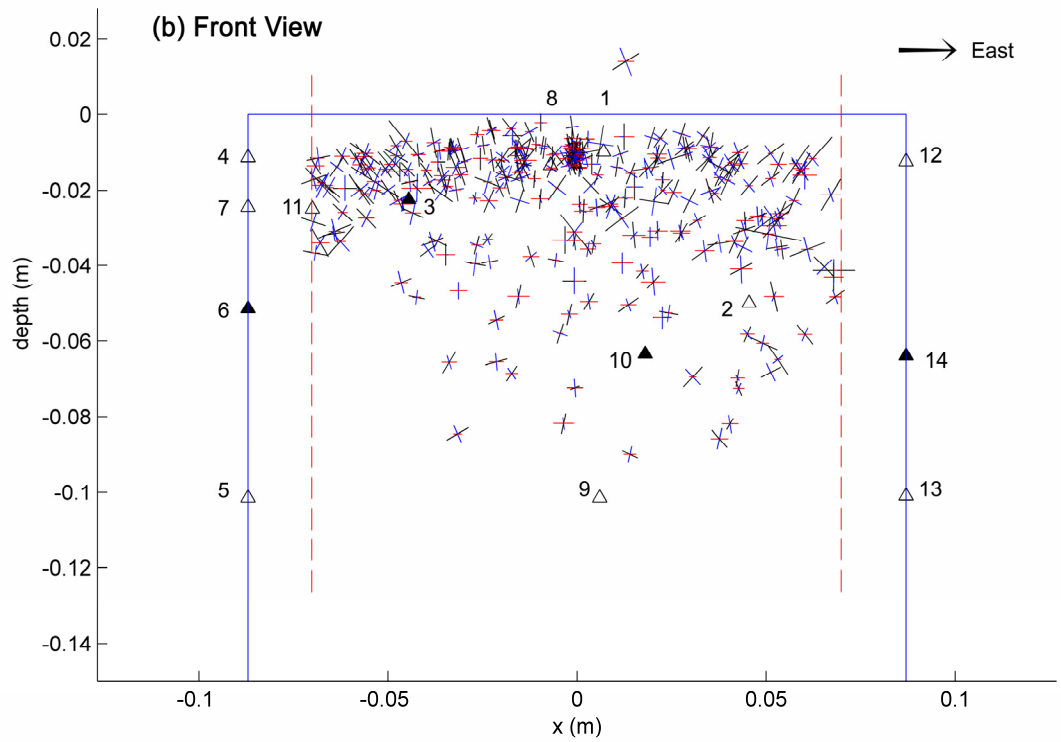

Figure 4.4. Front view of the same source location estimates shown in Figures 4.3 and 4.5.

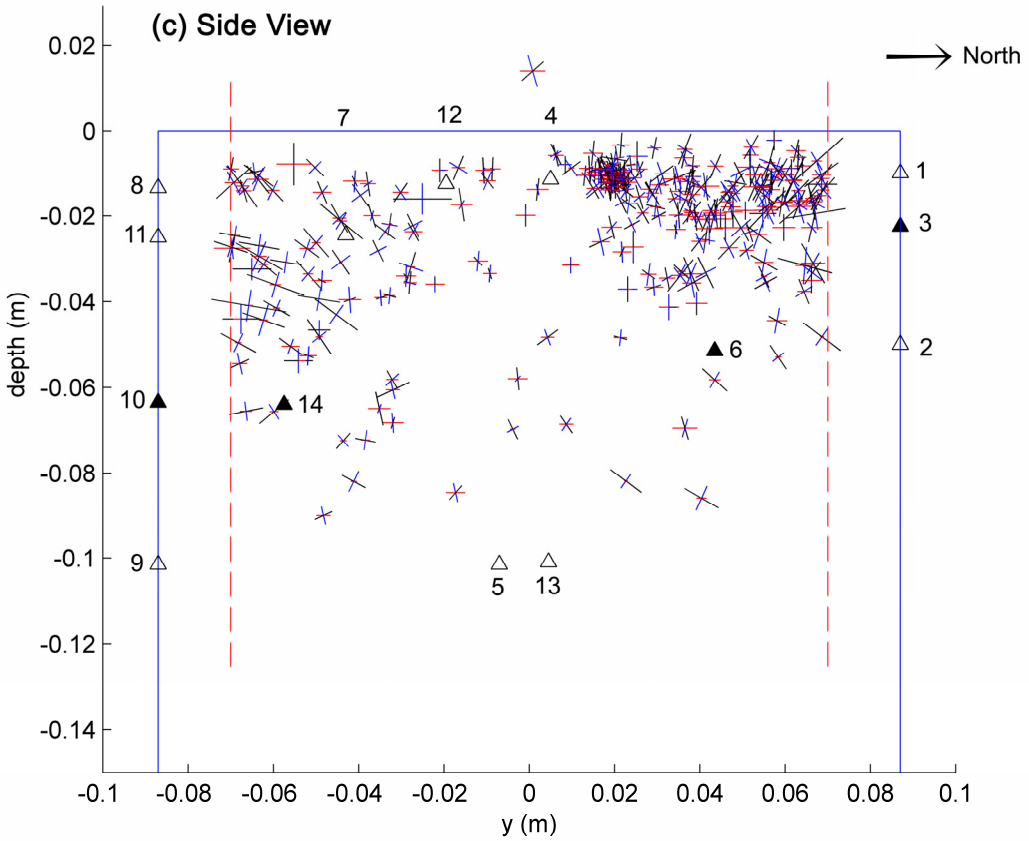

Figure 4.5. Side view of the same source location estimates shown in Figures 4.3 and 4.4.

The evolution of depth over the seventeen day monitoring period (for the same 340 events shown in Figure 4.3-4.5) is shown in Figure 4.6. The bars represent 95% confidence intervals calculated via the same method as those shown in Figure 4.3-4.5. The upper graph shows the locations found using a constant velocity model while the lower graph shows the results using a time varying velocity model. To estimate the change in P-wave velocity over time, artificial sources of stress waves, due to the sudden fracture of a mechanical pencil lead, were introduced at two different locations on the surface of the specimen on a daily basis. A velocity model was created based on the evolution of P-wave velocity estimated from the artificial sources and the assumption that the P wave velocity is initially increasing and then leveling off over the seventeen day period.

A very clear trend from surface to interior events can be seen from estimates using the constant velocity model, but the apparent increase in depth was due, in part, to bias induced by an inaccurate velocity model. For example, if the estimated velocity is higher than the true velocity, as was probably the case for the first few days of the monitoring period under the constant velocity model, the estimated source locations will be pushed further from the center of the sensor array. In this case, the inaccurate choice of velocity causes the estimated event locations above the surface of the specimen. The choice of velocity model can have a large effect on source location estimates, yet even with the time-varying velocity model, a trend toward increasing depth is apparent.

Despite the fact that inaccurate velocity assumptions make the absolute accuracy of source locations difficult to calculate, the relative uncertainty of the source locations is well known, and the error bars shown in Figures 4.3 and 4.4 provide a good measure of precision.

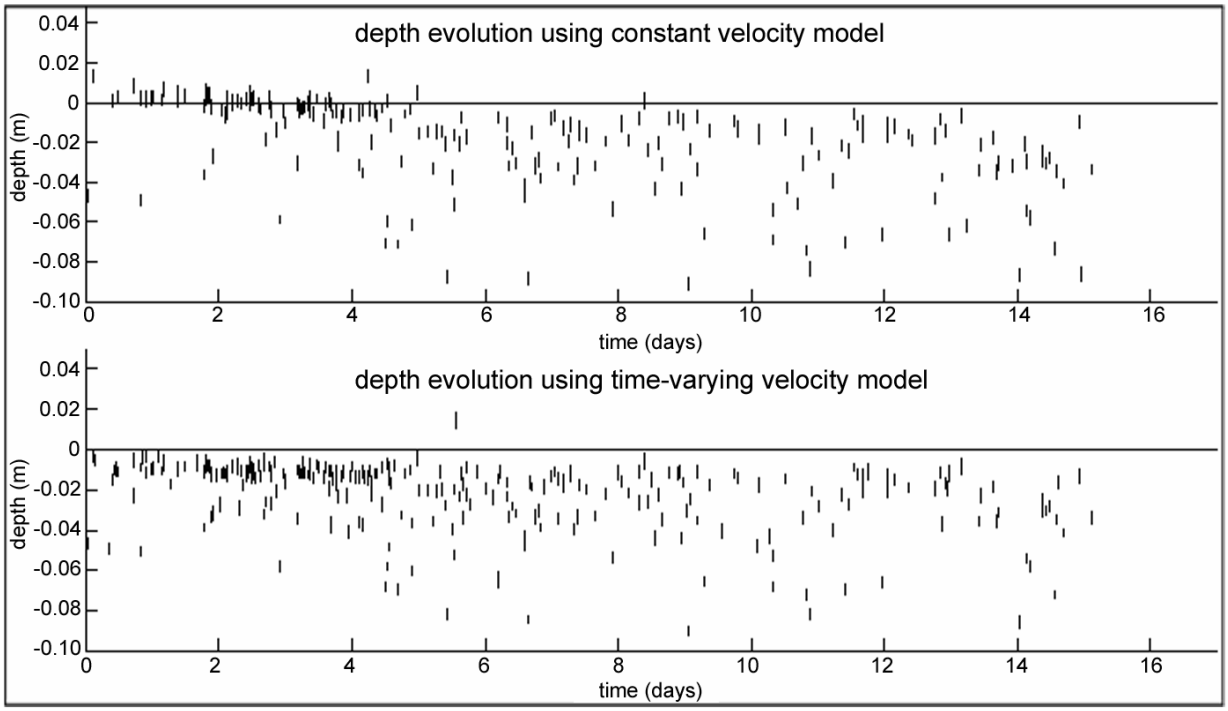

Figure 4.6. Evolution of depth of source location estimates over time using (a) constant velocity model (b) time varying velocity model. The vertical bars represent 95% confidence intervals.

4.4.2 Frequency content of recorded stress waves

The broadband Glaser-type sensors allow the frequency content to be studied. Variations in frequency content can be due to differences in the source or due to the medium through which the stress waves propagate.

Five signals and their corresponding frequency content are shown in Figure 4.7(a) and (b), respectively. These signals correspond to the waveforms recorded by five different sensors from the same stress wave source. The signal from the sensor closest to the source, shown as the top trace, has the largest amplitude and highest frequency content, while the signal recorded from the sensor furthest from the source (bottom trace) shows small amplitude signals and in a much lower frequency band. This variation in frequency content is due to frequency-dependent nature of scattering and intrinsic attenuation (often referred to as internal friction). A initially sharp stress pulse propagating through concrete will be smoothed and broadened by these effects (Landis and Shaw, 1995). Similar effects are seen for seismic waves propagating through the earth. Effectively, the concrete acts as a low-pass filter. Many of these stress wave sources contain frequencies of significant amplitude well above 500 kHz, but concrete strongly attenuates these high frequencies.

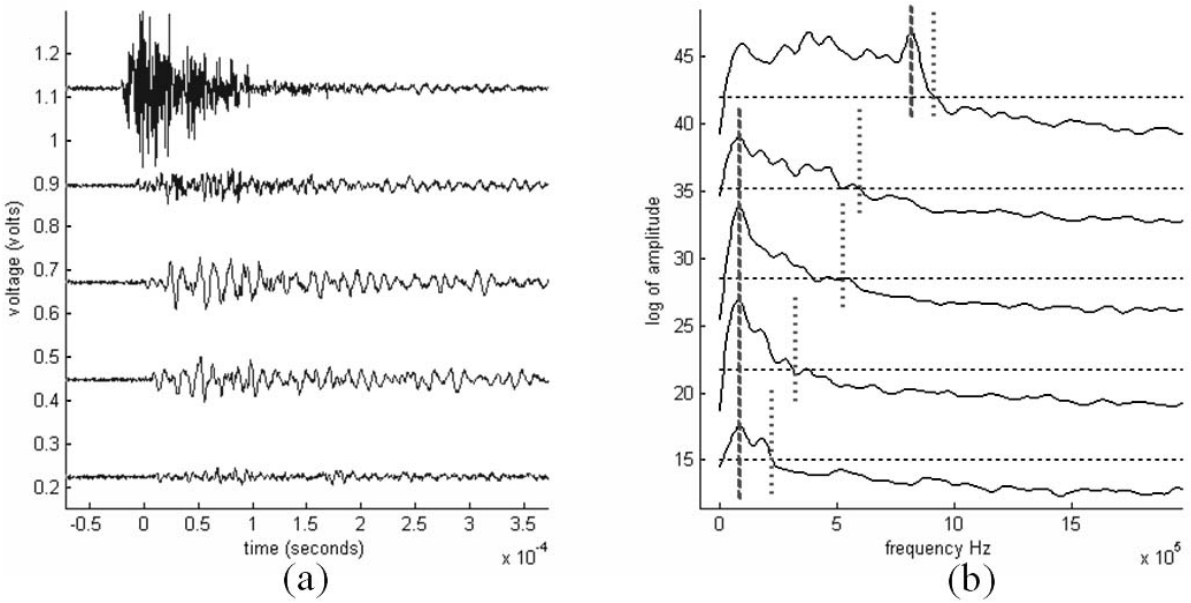

Figure 4.7. Signals recorded with five sensors at varying ranges from the location of the source. (a) signal amplitudes are proportional to surface normal displacement, and (b) corresponding frequency spectra, show that sensors close to the source see much more high frequency waves than those far from the source

4.4.3 Source characteristics

As described in Chapter 2, a Green's function is required for the precise determination of source characteristics. The inhomogeneous nature of concrete causes the stress waves to propagate somewhat differently than they would if concrete were a perfect linear elastic material. These deviations from linear elasticity include the scattering and attenuation described in Section 4.4.2. Because of this difficulty and the complicated set of reflections from the edges of the small specimens, Green's functions were not calculated for the concrete specimens. Consequently,

detailed studies of the focal mechanisms and time-histories of these stress wave sources were not carried out. Instead, general estimates of source mechanisms were made based on the direction and amplitude of first motion of the various phases of the stress waves propagating outward from the source. For example, nearly all recorded signals showed the first motions of the P-waves directed outward from the center of the specimen, indicating a compression first arrival, hence a crack-opening source.

Using forward modeling, it is possible to hypothesize the general characteristics of displacements which might be produced by a tensile crack source. Figure 4.8 shows qualitative estimates derived from very basic finite element model. The figure shows an illustration of particle displacements (highly exaggerated), in a cross section of the prismatic specimen, which would be expected to arise from an idealized surface crack source. In the figure, the P wave is outlined by the white dashed semicircle and the source location is depicted as a white star. Based on a number of different drying shrinkage tests, with different sensor geometries, some of the general characteristics of particle displacement described by this model were qualitatively confirmed. Firstly, sensors on the top surface of the specimen, shown as Sensor 1 in the figure, typically felt very small amplitude P-waves and very distinct and large amplitude Rayleigh (surface) waves. While P-waves of large amplitude exist at this location, the particle motion is almost entirely perpendicular to the surface of the specimen and normal to the direction of the sensor's sensitivity. In contrast, sensors located on the side faces of the specimen, shown as Sensors 2 and 3 in the figure, felt relatively large amplitude P waves and no sharply defined surface waves. Finally, sensors located closer to the bottom of the specimen, typically felt very little motion at all, due to the radiation patterns of P and S waves. This model was used to design the current experiment, particularly the sensor placement, so that large amplitude P-wave arrivals could be recorded, and robust source location estimates could be attained.

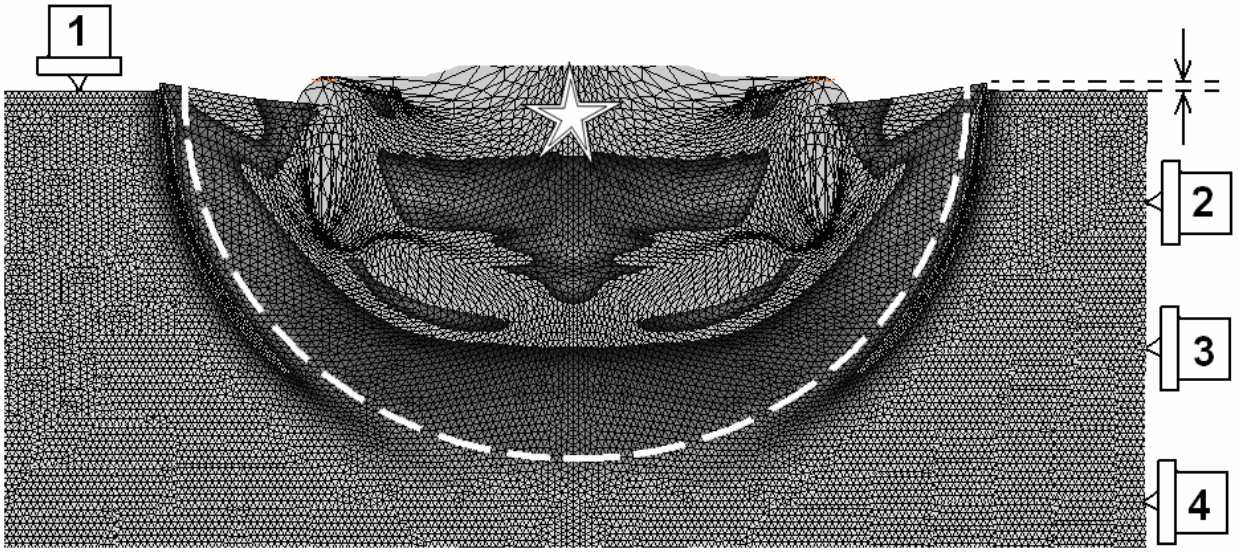

Figure 4.8. Schematic diagram of particle motions arising from a surface crack. Sensor 1 sees a small amplitude P wave because the direction of P-wave polarity is normal to the direction of sensor sensitivity, but it sees a large amplitude Rayleigh wave. Sensors 2 and 3 see large amplitude P waves. Sensors located below the source, which is marked by a white star, will see very small amplitude P and S waves. Array geometry for the current test was designed using this model.

4.5 Conclusion

An experiment was designed to record stress waves radiated from cracking due to the drying shrinkage of concrete. Consequently, sensors were located on the sides of the specimen near the top surface, so that large amplitude P waves would be aligned with the direction of sensitivity of the Glaser-type sensors. Concrete was shown to strongly attenuate high frequency stress waves >150, even for propagation distances of only a hundred mm. The 3D locations of hundreds of events recorded over a seventeen day drying period were estimated. Imprecision in P-wave picking and the inhomogeneous nature of P-wave velocity of concrete were estimated to be the leading sources of error, but these picking errors were then shown to be amplified by the array geometry errors. By making use of equivalent picking errors, uncertainty in the source location estimates was modeled, and the propagation of this uncertainty via array geometry effects and minimization errors was tracked. The relative precision of the source location estimates was quantified and a clear trend from surface events to interior events can be seen over the seventeen day drying period.

Chapter 5.

Nanoseismic Study of Sliding Friction

5.1 Introduction and background

Slip between two nominally flat surfaces is usually characterized as steady sliding, stick-slip, or a combination of the two types of motion. Similar behavior is also exhibited on faults. For example, some parts of the San Andreas fault are known to creep steadily and produce no large earthquakes, while other sections remain relatively locked and periodically (every ~200 years) rupture to produce large earthquakes (i.e. San Francisco, 1906). While stick-slip frictional behavior is widely observed, the physical mechanisms responsible are still poorly understood.

A great deal of laboratory friction research has lead to the development of empirical laws for frictional behavior during steady sliding (e.g. Dieterich, 1979; Rice and Ruina, 1983; Marone 1998). These laboratory-based models, known as the rate- and state-dependent friction laws, can successfully predict general friction behavior, but the physical meaning of the various rate-state parameters remains poorly understood (Dieterich and Kilgore, 1994; Berthoud et al., 1999; Putelat et al., 2011). The lack of a physics-based model makes it difficult to extrapolate rate-state parameters derived in the laboratory to the slip rates and length scales most relevant to earthquake mechanics.

The reported research illuminates the physical mechanisms of friction, particularly those responsible for the sudden transition from stick to slip. This topic is of great interest to scientists and engineers who would like to better understand or forecast when, how, and under what conditions fault slip will initiate. During the transition from stick to slip, the force of friction between the two surfaces is suddenly released or reduced. If this reorganization of force occurs very rapidly, it will cause stress waves to radiate away from the interface and propagate throughout the bulk of the material. When the frictional interface is a km-sized fault in the earth, this phenomena is known as an earthquake, but stress waves are also radiated from laboratory-sized faults, and this is termed nanoseismicity. In this work, stress wave source characterization (also termed nanoseismic analysis) is used to better understand the micro mechanisms responsible for observed stick-slip behavior. This study provides a better understanding of how particular rupture mechanisms generate different types of stress wave radiation patterns (i.e. different types of earthquakes), and how insights gained in the laboratory might be scaled up to advance our understanding fault rupture and earthquake generation.

This chapter first describes how two macroscopically smooth but microscopically rough surfaces interact, how these interactions can be studied, and how proposed stress wave analysis methods overcome many of the challenges inherent to the study of friction mechanisms. Next, the experimental apparatus and procedures are described along with some typical results. The results show that when an interface transitions from stick to slip a burst of high frequency stress waves are released. Buried within this burst are tiny discrete events, which are interpreted to be the discrete rupture of micrometer sized contacts known as asperities. Point-source forward modeling is used to identify the time history and focal mechanisms of individual asperity rupture events. By comparing and contrasting the results of experiments on PMMA/PMMA and rock/rock interfaces, systematic differences between asperity rupture on the two materials are linked to differences in material behavior on the micro scale. Finally, the effects of specimen

roughness and fault healing are explored. These observations highlight areas for future research.

5.1.1 The true area of contact

Modern studies of surface topography have shown that a surface which appears nominally flat on the mm and cm scale is, in almost all cases, quite rough at smaller scales (Brown and Scholz, 1985; Renard et al., 2006; Candella et al., 2009). Due to this micro-scale roughness, two surfaces pressed together only interact where the highest peaks of their topography meet, so "true" contact consists of an ensemble of μm-scale contacts. A cartoon of a slider block and a base plate in a typical experimental arrangement is shown in Figure 5.1. As shown, the slider block is pressed onto a base plate with a normal force F_n and pushed in the x direction with a shear force F_s through a spring of stiffness k. Figure 5.1(b) depicts the interaction of the nominally flat but microscopically rough surfaces. Note that the scale of the surface roughness in the z direction is greatly exaggerated.

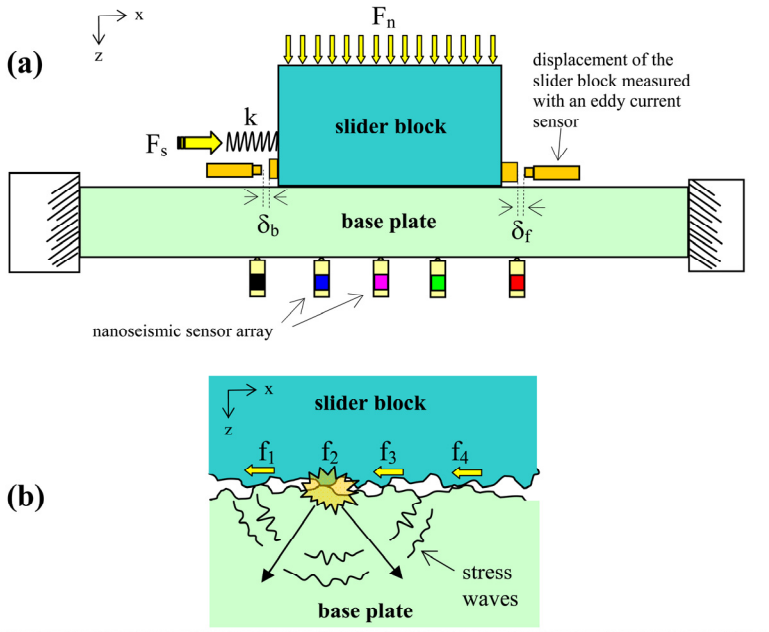

Figure 5.1: **a**, the basic experimental configuration for the sliding block experiment. In typical experiments of this type, a normal load F_n and a shear load F_s are applied, and the global displacement of the block is measured. **b**, due to micro-scale roughness of the surfaces, the slider and base plate only interact at tiny contacts. The current experimental setup employs an array of very sensitive nanoseismic sensors that can detect high frequency displacements which are the result of stress waves radiated from the frictional interface (similar to earthquakes).

A normal force applied to the slider block will initially be carried by a population of relatively few contacts, each with a small area of contact (only the highest peaks will be in contact). Often, the stress on these few contacts will exceed the yield stress of the material and cause the peaks of the topography to deform plastically, or fracture. This, as well as accompanying elastic deformation, will cause the highest peaks of the surface to be flattened, broken, and/or compressed, which will allow the next-highest peaks to begin to interact and carry some of the normal force. Eventually, the total area of all contacts will be large enough to carry F_n without any further yielding. The total area of all contacts is known as the true area of contact, Σ_t, which is typically much smaller than the nominal area of contact, Σ_n.

With optical techniques, Dieterich and Kilgore (1994, 1996) imaged these micro-scale contacts on a number of transparent materials. When viewed through the interface, they form what look like islands of contact surrounded by a sea of non-contacting area. This island view of the contacts is shown schematically in Figure 5.2 at increasing magnification. At the lowest magnification, the entire block appears to be in contact, but at a higher magnification, contact islands become apparent. Because of smaller length-scale roughness, it has been suggested (Persson et al., 2005) that at increasing magnification, what appears to be a single contact a lower magnification is composed of a cluster of smaller contacts.

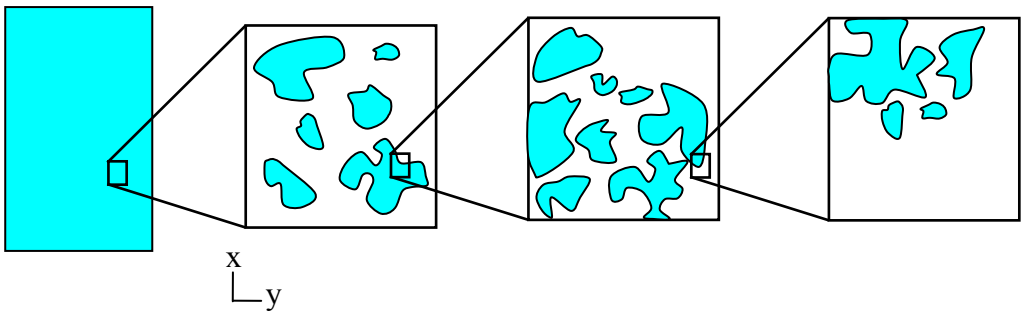

Figure 5.2. The true area of contact at increasing magnification. What appears to be a single contact at low magnification, may be a cluster of many smaller contacts, when viewed at higher magnification.

Dieterich and Kilgore (1994, 1996) also imaged contact population behavior in response to increased normal stress and time. They showed that when the normal force on the interface is increased, existing contact islands grow and merge and new contact islands form. The observed increase in contact population area with increased normal stress corroborates with previous theories (Bowden and Tabor, 1964; Rabinowicz, 1965) which explain Amontons's first and second laws, which state that the maximum shear force an interface is able to carry $F^{max}_s = \mu F_n$ (where μ is a constant) and is independent on the nominal area of contact, Σ_n. This is due to the proportionality between F^{max}_s and Σ_t, which is in turn proportional to F_n. These laws have been shown to be roughly correct for a wide variety of materials (rock, metal, ceramics, polymers, paper, etc.) and variations in surface roughness, therefore the evolution of contact islands is dependent on a relatively universal feature of natural surfaces (such as multi-scale roughness) rather than a case-specific deformation mechanism such as plastic yielding.

Dieterich and Kilgore (1994, 1996) also observed a similar increase in total contact area (and thus an increase in interface strength) with increasing time of contact. As a result, the contacts should be thought of as a dynamic population that evolves over time and changes in the stress state. An increase in frictional strength with passing time (healing) has been widely observed in laboratory stick slip friction experiments (see, e.g. Marone, 1998) and is an essential part of the rate-state friction laws. In the field, similar behavior has been inferred for faults based on observed seismic velocity changes within the shallow rupture zone after the Landers earthquake (Vidale and Li, 2003), and observations of small repeating earthquake sequences (Vidale et al., 1994; Peng et al 2003). Seismological studies based on small repeating earthquakes (e.g. Nadeau and McEvilly, 1999; Schaff and Beroza, 2004; Dreger et al., 2007), suggest the repeated failure of stick-slipping asperities surrounded by aseismically creeping fault. These seismic observations have motivated earthquake models which paint a qualitatively similar picture for faults (Johnson and Nadeau 2002, 2005; Noda et al., 2009; Johnson, 2010). In

these models, all fault strength is supplied by a sparse population of contacts, known as asperities. In this chapter, the terms asperity and contact will be used interchangeably.

5.1.2 Asperity rupture and detection

Asperities not only carry normal forces, the total shear force, F_s, is held by the same population of asperities. Each asperity has a different strength and stress state, therefore when F_s is increased, some asperities will rupture before the others. Let us assume that an individual asperity is initially carrying the shear force f^1_i, and that after it ruptures, the asperity carries shear force f^2_i, where $f^1_i > f^2_i$. Two possible states of force release are depicted in Figure 5.3. In both cases, the force-time function includes a step with a rise time (or drop time, in this case) equal to t_{rise} and amplitude $\Delta f = f^1_i - f^2_i$. The force-time function for Case 2 can be modeled as the superposition of a step and a pulse (step+pulse). These source functions are similar to those of the glass capillary fracture, described in Chapters 2 and 3, but for asperity rupture, the direction of the force is expected to be in the plane of the plate, instead of in the plate-normal direction.

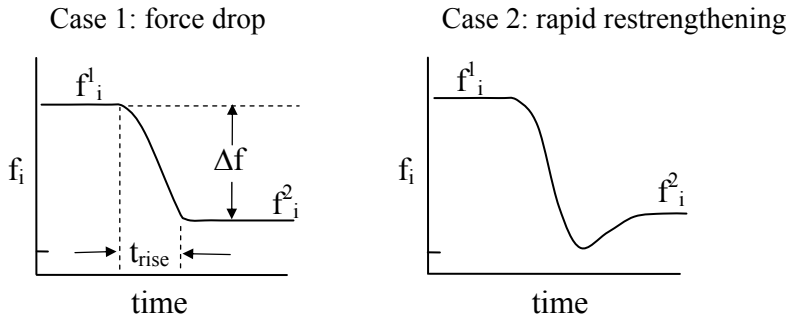

Figure 5.3 The force time histories of two possible states of individual asperity force release.

When one asperity slips or breaks, Δf will be redistributed to the other asperities. The redistribution of force does not happen instantaneously, but is the result of stress waves radiated from the location of asperity rupture, as depicted in Figure 5.1. If a neighboring asperity was close to failure, the redistribution of force could be enough to cause the second asperity to rupture, which could cause other asperities to fail, which may eventually cascade into gross sliding of the whole block.

Stress waves radiating from a rupturing asperity can be detected with the nano-seismic techniques described in this dissertation, but certain contact rupture characteristics are required for detection with the Glaser-type sensors. First, the rupture must occur rapidly. The Glaser-type sensors (as well as most other sensors with comparable sensitivity) lose sensitivity at very low frequencies, i.e. below ~8 kHz, so if force redistributions occur very slowly (t_{rise} >100 μs) they will not be well resolved or will go undetected. Additionally, high frequency/short wavelength information provides spatial resolution, so analysis capabilities (source location and characterization) are considerably improved when considering higher frequencies (>100 kHz). There is no upper bound on how fast the rupture can occur and still be detected because step-shaped source functions contain low frequency components which can be detected even with a band-limited recording system. Although, the 10 MHz sampling frequency of the experimental equipment does not provide any resolution to t_{rise} estimates for source rise times less than about 500 ns.

Next, the source must have a minimum amplitude--it must release enough force, or redistribute enough stress, that displacements produced by the radiated stress waves can be detected above the level of background noise. When determining the minimum detectable source, the frequency content and radiation pattern of the source must be considered, as well as the distance from source to sensor and host material. For the experiments to be described, the minimum detectable force drop is approximately 1 mN. For an asperity with a strength of 1-20 MPa, this would equate to a contact patch on the order of 10-40 μm in diameter.

Finally, it is possible to detect clusters of asperity ruptures of lower amplitude if they occur in close spatial and temporal proximity to each other (<5mm, <5 μs). The coherent rupture of many small and closely spaced asperities will produce stress waves which sum constructively and appear equivalent to the stress waves produced by a single, larger asperity. If the small asperities are more widely spaced and/or do not rupture coherently, the high frequency components of the radiated stress waves will either destructively interfere or will be too small in amplitude to be individually detected, but the lower frequency components will constructively interfere and will be detectable.

5.1.3 Prior research

The mechanisms of friction are particularly difficult to study due to the extremely broad range of scales involved, both in space and time. Temporally, events take place both very rapidly and very slowly. For example, crack-like shear ruptures may propagate close to the seismic velocity (around 1-10 km/s), while typical loading rates for laboratory shear experiments are on the order of μm/s, and contact populations may evolve over hours, days, or weeks. Spatially, a frictional interface may extend many cm while micro-scale roughness interacts to form contacts on the μm scale. This wide range of scales presents serious challenges for modeling and experimental observations.

Classic laboratory friction research (e.g. Dieterich, 1979; Marone, 1998; Scholz, 2002) uses specimen-averaged measurements of the forces and displacements of a sliding block (i.e. Figure 5.1), cylinder, or annulus. But because measurements are specimen-averaged, information about the micromechanics of the contacts which comprise the interface must be inferred from the gross behavior of the entire specimen.

Optical methods have contributed some insights into micro-scale interactions. In addition to Dieterich and Kilgore (1994, 1996), Rubinstein et al. (2005) and Ben-David et al. (2010) mapped dynamic changes in contact statistics that occur during and preceding the transition from stick to slip on PMMA. Other researchers (Rosakis et al. 1999; Xia et al. 2004, Lykotrafitis et al., 2006) used photo elasticity to study dynamic shear rupture propagation in homolite. These experiments offer insights into material behavior, but are limited to studies of transparent materials. Other constraints include low image acquisition rates (100 kHz), and a difficult tradeoff between high spatial resolution and a large field of view.

Stress wave methods (also commonly known as acoustic methods or the method of acoustic emission) are commonly applied to friction research (e.g. Sammonds and Ohnaka, 1998; Yabe et al., 2003; Thompson et al., 2005; Mair et al., 2007; Yabe, 2008; Zigone et al., 2011). The principle advantage of stress wave analysis over optical methods is that since stress wave sources radiate waves in every direction, each acoustic sensor is not limited in field of view. For stress wave methods, data interpretation is more challenging than data acquisition. Difficulties in interpretation typically stem from (1) the low quality of the sensors used (as compared to broad

band instruments used in global seismic networks, for example) and (2) the extremely complicated set of reflections that interact within a small-sized laboratory specimen. The sensors commonly used in stress wave methods are typically resonant in nature, such as the PAC R15 sensor analyzed in Chapter 2. As described in the sensor calibration study, these sensors introduce severe distortion to the signal both because of sensor resonance and aperture effects. Consequently, stress wave data recorded from friction tests is typically not amenable to rigorous and quantitative analyses similar those performed on regional and global seismic records, and few important insights into underlying physical processes have been made.

In the present work, these difficulties are overcome by (1) using the absolutely calibrated, wideband Glaser-type piezoelectric displacement sensors with well characterized instrument response functions $I(\omega)$, and (2) using a large plate as a test sample and propagation medium for which theoretical Green's functions can be readily calculated and validated. The base plate is large enough to insure that stress wave information propagating directly from the source is recorded for more than 100 μs before being contaminated by reflections from the specimen sides. The same plate specimen is used for both absolute sensor calibration and the friction experiments.

5.2 Methods

5.2.1 Description of the apparatus

A schematic drawing of the friction apparatus used for these experiments is shown in Figure 5.4. The apparatus can accommodate a large (915 mm) base plate and can apply a normal force of up to 4000 N via two balanced hydraulic cylinders. Shear force, measured with a Measurement Specialties ELPF load cell, is applied by turning a micrometer-threaded screw which presses against the trailing edge of the slider block at a height h (typically 15 mm) above the interface. A thrust bearing decouples torque from the specimen. The normal force is calculated from the hydraulic fluid pressure which is measured with a digital pressure gage. Eddy currant sensors (Shinkawa VC-202N) are used to measure the displacement of the block relative to the base plate. Sensitive to up to about 20 kHz, these instruments are extremely stable at low frequencies and have a resolution of <3 μm. Typically, displacement measurements are taken at both the leading edge and trailing edge of the slider block, as shown in Figure 5.1.

Two different materials were tested: rock and PMMA. The rock slider block (180 x 77 x 55 mm) and base plate (613 x 460 x 77 mm) are composed of Academy Black granite, a Jurassic hornblende diorite (from Clovis, California), cut to size, polished government specification GGG-P-463c-AA flatness tolerance, and then roughened by surface grinding with 36 grit silicon carbide. The surfaces of the PMMA specimens, slider block, typically 180 x 60 x 17 mm, and base plate 460 x 305 x 36 mm, were milled flat and then roughened with either 600 grit or 40 grit silicon carbide.

The current experimental system contains an array of 13 Glaser-type sensors, labeled S1-S13, and referred to here as the nanoseismic sensor array. This array is located underneath the base plate (see Figure 5.4d and Table 5.1 for locations) and detects high frequency stress waves from a near-rupture vantage point. Sensors S1-S13 are connected to a high-speed digitizer (10 MHz sampling rate, 16 bit dynamic range). The trigger threshold for data captured in multi block mode was set at 3.5 pm (on PMMA) and 0.6 pm (rock), reached for a duration of > 600 ns, on any of the sensors. The difference in trigger threshold levels accounts for the different

thicknesses and elastic properties of the two base plate materials, so that the smallest amplitude signals recorded on both materials will be from sources of equal strength (in N). Record length is 12.8 ms, with a pre-trigger length of 6.4 ms. Because of this long length, blocks of data often contained multiple discrete stress wave sources which are analyzed separately.

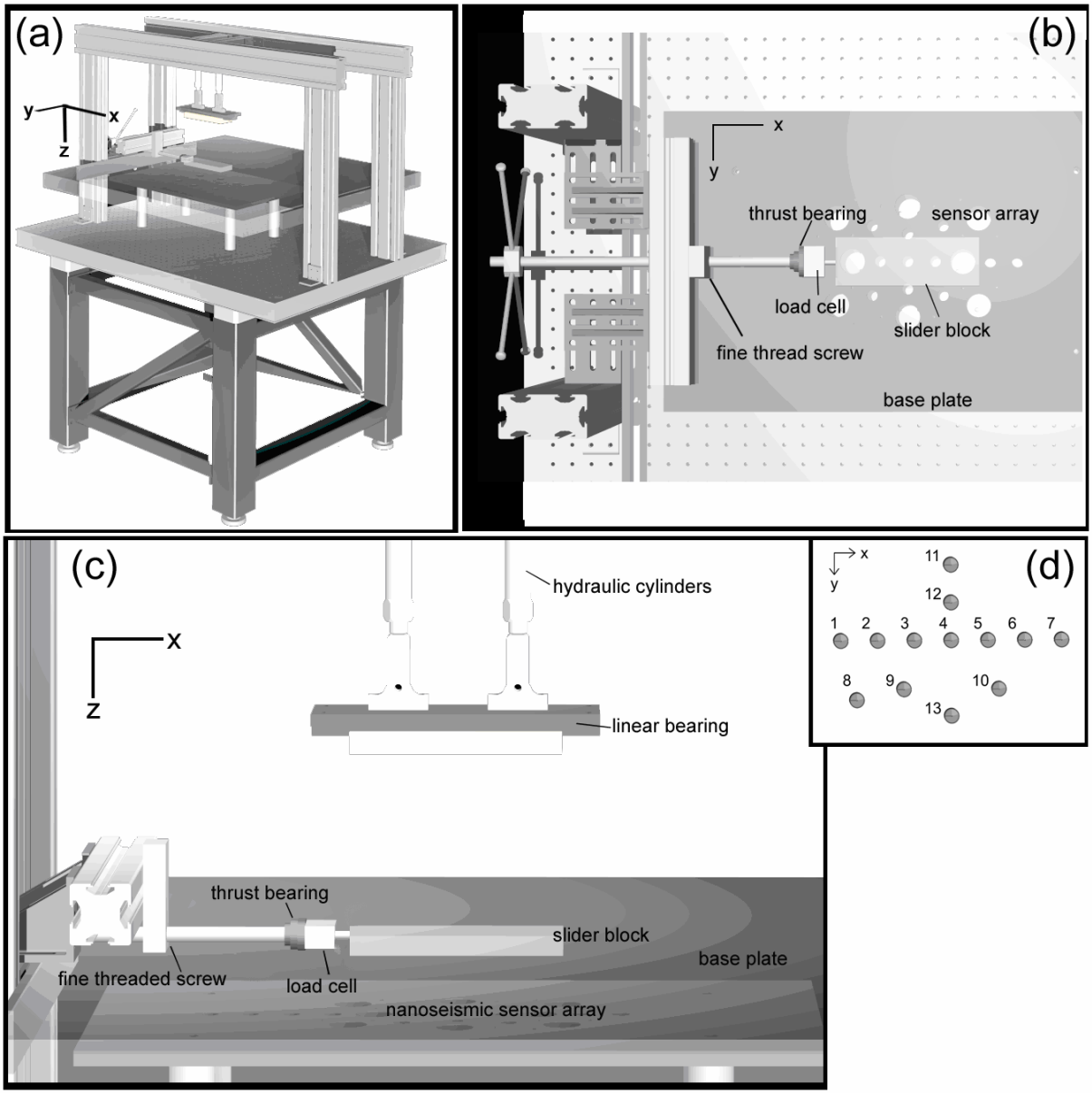

Figure 5.4 A sketch of the friction apparatus used for the current experiments on rock and PMMA. a, an isometric view of the whole apparatus. b, top view of the shear loading device without the linear bearing or hydraulic cylinders. c, side view closeup of the shear loading device. The hydraulic cylinders extend so the linear bearing moves down to apply the normal force on the slider block. d, the locations and numbering of the 13 nanoseismic sensors.

5.2.2 Stress wave analysis

The large base plate delays and dampens the reflections from the plate perimeter. During the ~100 μs time period preceding the arrival of the side reflections, wave propagation in the base plate is fully characterized by theoretical Green's functions for an infinite plate, which were calculated using a generalized ray theory code (Hsu, 1985) and verified by finite element models (McLaskey and Glaser, 2009) and analytical solutions (Pekeris, 1955; Knopoff 1958; Johnson, 1974). The base plates used in the friction experiments were also used for calibration experiments, so that the entire experimental system (the sensors and sensor coupling, wave propagation effects, and data acquisition system) was calibrated in-situ, just before and after each experiment, following the procedures outlined in Chapter 2. The high fidelity sensors, large base plate, and the Green's functions which have been validated with calibration sources, allow study of the full waveform of the recorded signals.

	X Location (m)	Y Location (m)
Sensor S1	-0.105	0.000
Sensor S2	-0.070	0.000
Sensor S3	-0.035	0.000
Sensor S4	0.000	0.000
Sensor S5	0.035	0.000
Sensor S6	0.070	0.000
Sensor S7	0.105	0.000
Sensor S8	-0.090	0.055
Sensor S9	-0.045	0.045
Sensor S10	0.045	0.045
Sensor S11	0.000	-0.070
Sensor S12	0.000	-0.035
Sensor S13	0.000	0.070
Rock/Rock event	-0.005	0.022
Plastic/Plastic event	-0.035	0.026
Capillary calibration	0.023	-0.048
Ball drop calibration	0.001	-0.060

Table 5.1 The X and Y locations of sensors and the sources shown in Figures 5.8 and 5.10

While PMMA and rock are expected to have different frictional properties, they also have different wave propagation properties, which must be taken into account when analyzing recorded signals. Firstly, the wave speed in PMMA is lower (c_p = 2800, c_s = 1400,) than in the rock (c_p = 6550 m/s, c_s = 3700 m/s). A lower wave speed yields a longer P-S-wave separation time and allows the source location to be determined at a higher resolution.

The most important differences between wave propagation in PMMA and rock are deviations from perfect linear elasticity. PMMA attenuates stress waves. As described in Chapter 3, a quality factor Q=80 was found for this material. In the rock, some scattering was observed, presumably because of grain boundaries, but attenuation was negligible for the frequencies and propagation distances considered. A consequence of the low Q in PMMA was that it sapped most of the energy from high frequency waves reflected from the edges of the base plate and simplified analysis in the high frequency band. In the rock, reflections persisted for a longer time, and muddied the wave field, making analysis somewhat more challenging.

Finally, the sensor sensitivity is different when coupled to the two materials. It was shown in Chapter 3 that the sensor is about 15 dB less sensitive when coupled to PMMA than when coupled to steel, glass, or aluminum. On rock, the sensor had approximately the same sensitivity as when coupled to steel, aluminum, or glass.

5.2.3 Basic description of the experiments and results

During a typical experiment, the shear force, F_S, is increased until the block transitions from stick to slip. During each slip instability, an intense burst of waveforms are recorded with the nanoseismic sensor array. Examples of measurements of shear force, block displacement (from the eddy current sensors), and the waveform captured from one channel of the nanoseismic array are shown in Figure 5.5. To give an indication of the frequency content of the nanoseismic signal, a filtered version of the same signal (100 kHz high-pass filter) is also shown.

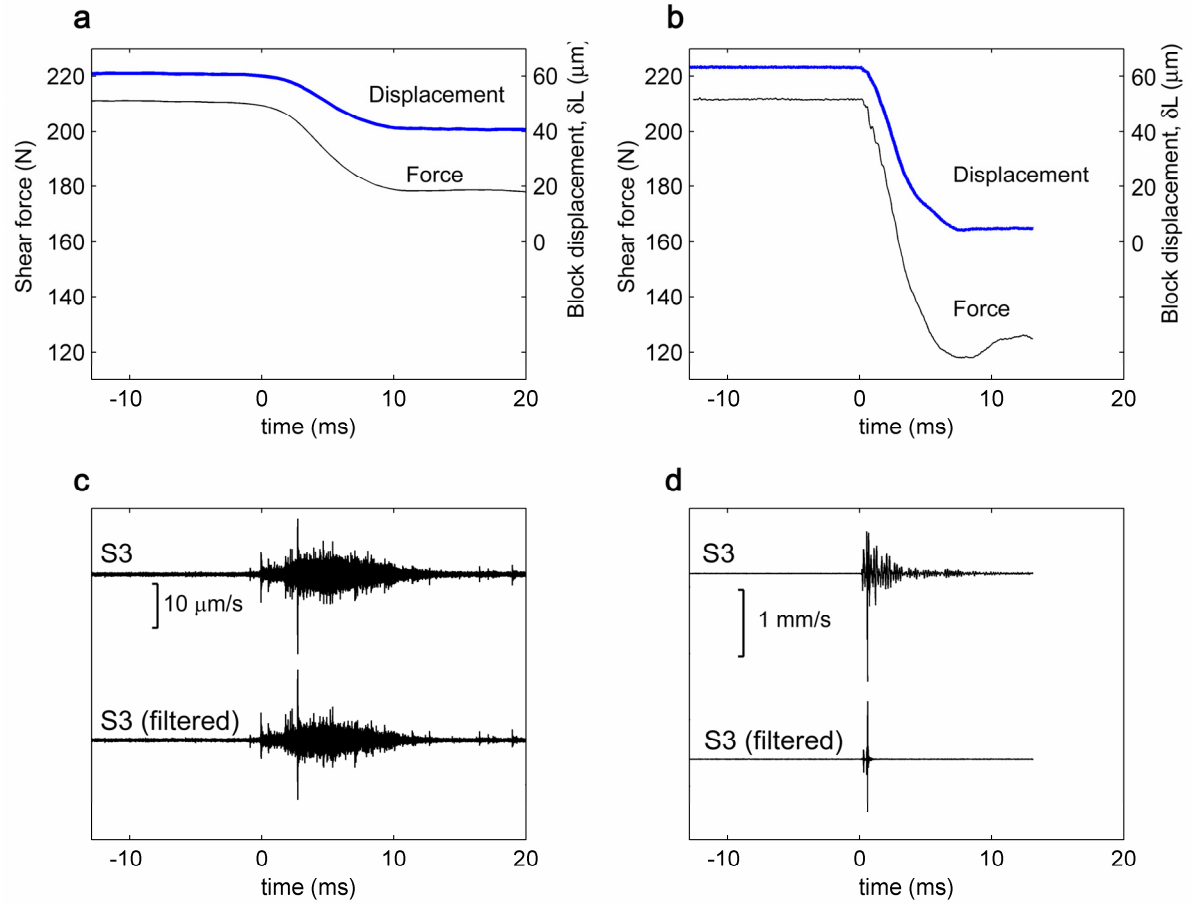

Figure 5.5. Comparison between rock and PMMA experiments performed on the same apparatus under similar conditions. Both instabilities occurred at similar shear and normal force conditions, but the total slip was much greater for the PMMA and the nanoseismic characteristics of the two materials are vastly different. **a,** Details of a slip instability for the rock/rock interface. **c**, burst of seismicity associated with **a**. **b**, Details of a PMMA/PMMA slip instability. **d**, sesimicity associated with **b.** The lower traces of **c** and **d** have been high pass filtered at 100 kHz. The signals recorded on the rock are almost entirely above 100 kHz, while the PMMA signals have a significant lower frequency component and are mostly coincident with the initiation of slip. Note that **a** and **b** are plotted on the same scale, but **c** and **d** are not.

When the rock slider block slips, it accelerates and decelerates (relative to the rock base plate) as a rigid body, and the stress waves were radiated from the interface as many discrete and sporadic bursts originating from all over the block interface. The PMMA, however, had a much more complicated behavior. It was often observed, particularly for long, narrow samples, that the slip initiation times at the leading and trailing edge of the slider block would differ by up to 1 ms. This implies that for a short time period during the initiation of rupture, part of the block would remain pinned while another part would start to slip.

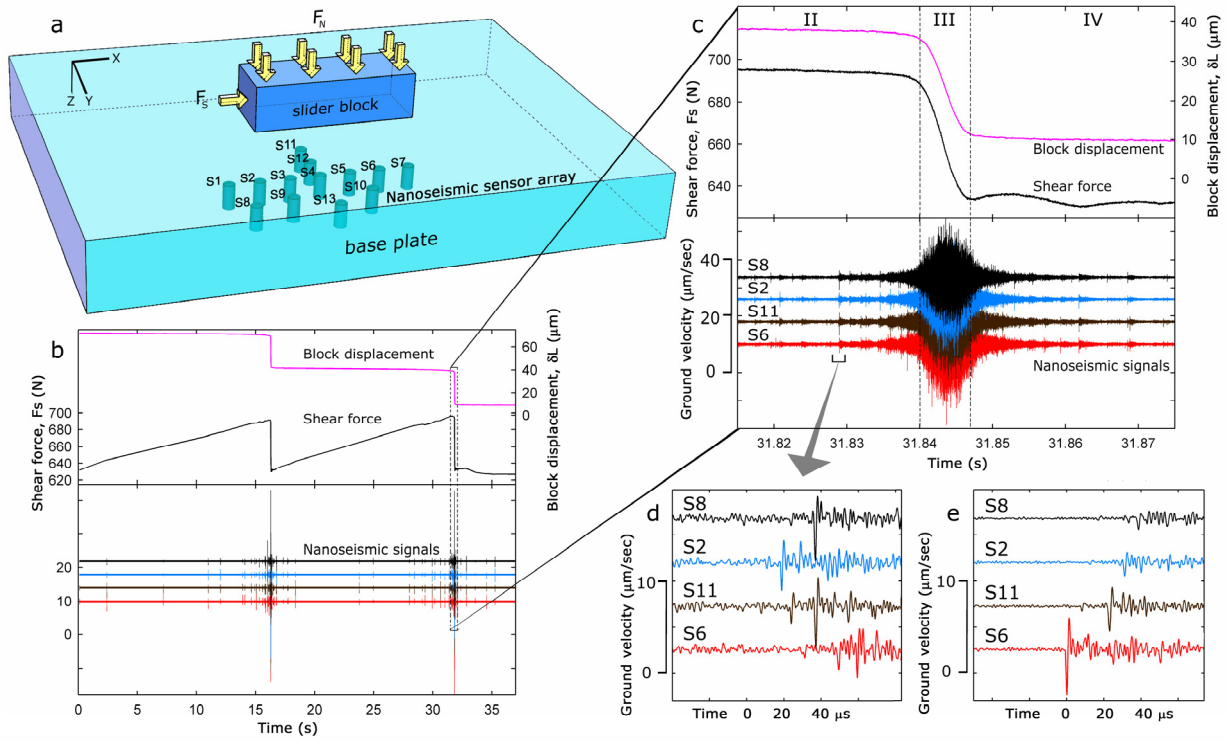

Figure 5.6 Schematic diagram of experimental configuration and typical results for a rock/rock interface. **a**, A constant normal force, F_N, loads the slider block onto the base plate. An array of 13 sensors is located directly underneath the base plate. Shear force, F_S, applied to the trailing edge of the slider block, is slowly increased until the block slides in repeated stick-slip fashion. **b**, Shear force and slider block displacement relative to the base plate, δ_L, are shown for two full stick-slip cycles along with simultaneous measurements of the radiated elastic waves, denoted 'nanoseismic signals'. **c**, Details of one stick-slip instability show that the recorded signals consist of a multitude of discrete events. **d, e,** Single events shown in more detail illustrating rapid (~μs) P- and S-wave arrivals. In **b-e**, recorded displacement signals have been differentiated to produce velocity. The event shown in **e** is from an 'aftershock' occurring 0.2 seconds after the macroscopic slip instability shown in **c**.

Detailed results from another typical rock/rock test are shown in Figure 5.6. As illustrated, even the rapid stick-slip instability of the rock/rock interface is characterized by a smooth (on the ms time scale) acceleration and deceleration of the block. A stick-slip instability of the rock/rock interface always produced a tremor-like burst of exclusively high frequency (>100 kHz) signals. This burst was typically ~5-40 ms in duration. Close inspection of this burst reveals that it is composed of a multitude of discrete events on the order of 1 μs in duration (Figure 5.6d), many of which can be located and rigorously analyzed by their clearly identifiable P and S waves. By hand-picking unmistakable waveforms, about fifty discrete events can usually

be identified from amid the tremor-like signal; the rest were too small in amplitude relative to the noise of reflections from previous events to be evaluated with the current methods. In general, events were well distributed over a large portion of the nominal contact area, suggesting the sporadic rupture of discrete contacts. The locations, timing and amplitude of 53 events located in a 300 ms time window surrounding the rock/rock slip instability of Figure 5.6 are shown in Figure 5.7. These discrete, high frequency events are interpreted to be the rapid rupture of micrometer sized asperities.

In contrast, the stick-slip of the PMMA was more variable and produced a more complicated seismic response. In general, slip on the PMMA block occurs more abruptly and releases more shear force than the rock (see Figure 5.5). The rupture of the PMMA typically produces large amplitude lower frequency (<20 kHz) seismic waves with a few high frequency (>100 kHz) events (discrete asperity ruptures) riding on top of the lower frequency signal. Given the point source assumption inherent in the analysis methodology, only the high frequency events could be precisely located and rigorously analyzed via the methods described in this thesis. Additionally, as shown in Figure 5.5, all high frequency events, and the majority of all seismic energy recorded in PMMA, is coincident with the initiation of sliding. This is in contrast to the rock which continued to produce high frequency events throughout slip.

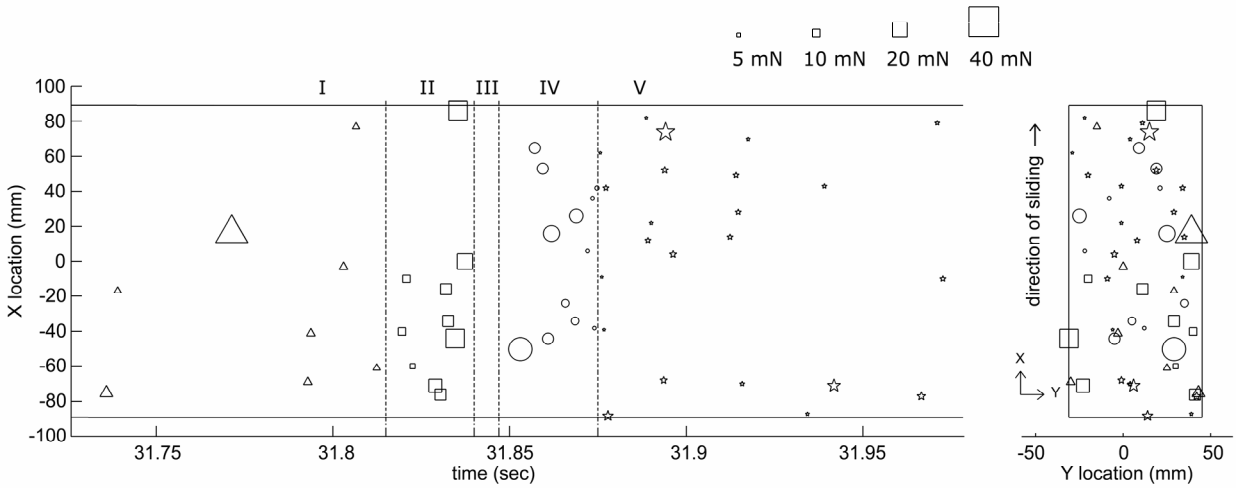

Figure 5.7. The locations, timing, and amplitude of 53 events located in a 300 ms time window surrounding the rock/rock slip instability shown in Figure 1. Time period III coincides with the most rapid sliding. Periods II, III, and IV correspond to the time window shown in Figure 5.6c.

5.2.4 Point source modeling and calibration

When analyzing high frequency (<100 kHz) events from both plastic and rock tests, it is assumed, as it has throughout this dissertation, that the stress wave source can be treated as a point source. First, the location of the source, ξ, is determined from the relative timing of various wave phases. The wide-band sensors detect sharp wave arrivals from both P and S waves, and this permits the location of each event to be found with ~mm spatial and ~μs temporal resolution.

Though the slider block and base plate appear to be in intimate contact, both the PMMA/PMMA and rock/rock interfaces were found to be acoustically highly reflective, and this affects the way in which the events must be modeled. While low frequency waves (<1 kHz) are

transmitted across the fault, stress waves in the detection range (~8 kHz - 2 MHz) are largely reflected. This is evidenced by multiple reflections through the thickness of the base plate (Figures 5.8 and 5.10). By assuming that most asperity contacts are close to the material yield stress, it is estimated that for plastic, micro contacts comprise much less than 0.1% of the nominal contact area at the ~100 kPa applied normal stress. If the interface between the slider block and base plate were fully transparent, as is typically assumed in earthquake studies (Aki and Richards, 1980), the source should be modeled as a set of force couples, each with some time history f(t), acting within the interior of a body composed of both the base plate and slider block. Because the fault is reflective, it is effectively a free surface at high frequencies. Consequently, it was found that the wave field in the base plate is best modeled as resulting from a single force f(t) acting on the interface, similar to the way landslides are modeled (Kawakatsu, 1989). For a reflective fault, ground displacements from far field P and S waves are proportional to f(t), instead of df(t)/dt for an acoustically transparent fault.

When forward modeling point sources, a full waveform synthetic seismogram,

$$s^{synth}(\mathbf{x},t) = f_j(\boldsymbol{\xi},\tau) \otimes g_{kj}(\mathbf{x},t;\boldsymbol{\xi},\tau) \otimes i_k(t),$$

is constructed from the theoretical Green's function, $g_{kj}(\mathbf{x},t;\boldsymbol{\xi},\tau)$, a postulated source-time function, $f_j(\boldsymbol{\xi},\tau)$, and the calculated instrument response function $i_k(t)$. This synthetic seismogram allows a direct comparison to be made between recorded signals, and the waveforms one would expected to record from a postulated stress wave source, $f_j(\boldsymbol{\xi},\tau)$.

The suitability of the chosen theoretical Green's functions is verified by means of known calibration sources (i.e. the ball impact and glass capillary fracture sources) which are applied in situ, just before and after each experiment. The instrument response function is determined via the methods outlined in Chapter 2. An example of the excellent fit between recorded signals and synthetic seismograms for calibrations on the rock plate are shown in Figure 5.8. As shown, the synthetic seismograms correctly model P waves, S waves, mode converted waves, wave reflections through the thickness of the base plate, and lower frequency motions which result from nearfield terms in the wave propagation solutions. The high frequency noise which gives the experimental signals "roughness" when compared to the smoother synthetic waveforms is due to scattering of high frequency waves in the rock, which is not accounted for in the Green's functions. This scattering is especially apparent for the signals recorded from the capillary fracture source (Figure 5.8a) because this source delivers more high frequency content in to the rock than the band-limited ball impact (Figure 5.8b). The excellent quality of fit between recorded signals and synthetic signals validates the theoretical Greens functions, and increases constraint for and confidence in estimates of stress wave source properties.

Source properties are estimated by parametrizing the source, $f_j(\boldsymbol{\xi},\tau)$, and varying those source parameters (directionality, amplitude, and shape of $f_j(\boldsymbol{\xi},\tau)$) so that the full waveform of the synthetic seismograms matches the shape and absolute amplitude of the recorded signals. More emphasis is placed on matching the initial wave arrivals (the initial P-wave, mode converted waves, and S-wave) than later arriving reflections. The directionality of the source (the direction i of $f_i(\xi,t)$) was found by varying azimuth and dip angles of the force vector. The general shape of the source-time function was chosen from the following options: pulse, step+pulse, step, step+ramp, and ramp. Finally, the source rise time and amplitude were varied to match the wave arrival shape and amplitudes, respectively. Examples of the match between recorded signals and synthetic signals are shown in Figures 5.8 and 5.10.

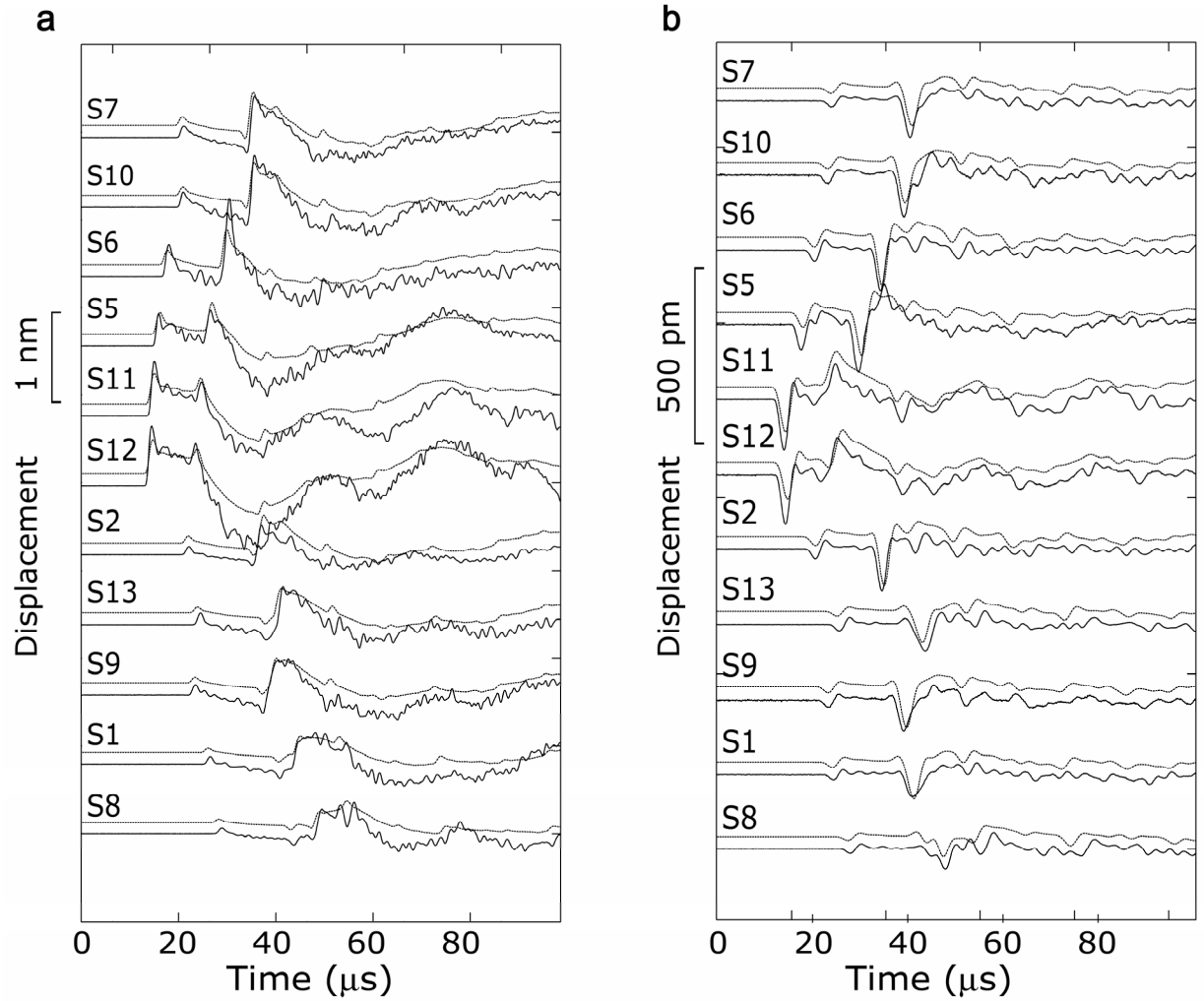

Figure 5.8. Comparison between recorded signals and synthetic seismograms (thin, dashed lines) for two different calibration sources on the rock base plate. **a**, Glass capillary fracture. **b**, A 1.00 mm diameter glass ball dropped 200 mm onto the rock base plate. Both the ball and capillary sources are modeled as a point force acting normal to the plate surface. The capillary source is well modeled as a step force which suddenly unloads the plate with a rise time of 100 ns, while the ball source is modeled as an impulse of 3.2 μs duration. The amplitude of the step is equal to the independently measured force (9 N) on the capillary at the time of fracture. Sensor and source locations are listed in Table 5.1.

5.3 Results and discussion

Over fifty slip experiments, on both the PMMA/PMMA and rock/rock interfaces, were performed, with varied normal stress, shear loading rate, interfacial age, surface roughness, and sample geometry. The results are divided up into three main sections. The first section describes a detailed study of the high frequency (>100 kHz) events observed on both materials. In this section, point-source modeling is used to identify the focal mechanisms, source time history (f(t)), and absolute amplitude of the force redistribution required to generate these high frequency stress waves. The next two sections describe more general observations of changes in recorded seismicity with respect to varying fault roughness and healing time.

5.3.1 Source characteristics of high frequency events.

The most ubiquitous and consistent result from the suite of experiments is that for *all* of the high frequency (<100 kHz) events analyzed, focal mechanisms of PMMA/PMMA events are consistently different from those of rock/rock events. This implies a systematic and material dependent difference in the micro-mechanisms of asperity rupture. Using forward modeling techniques, a pair of source models was determined which provide the best fit between synthetic seismograms and the recorded signals. The source models for the events are shown in Figure 5.9. In these models, the source function, f(t), is modeled as a step. The amplitude of the step, Δf, is equal to the force that is rapidly released during the asperity rupture. White arrows in Figure 5.9 inset, show the direction of the force release, which is the most important difference between the two source models.

5.3.1.1 Rock/rock

For the rock, asperity failure releases both shear force and normal force. This radiation pattern indicates a unidirectional implosion, with the direction of implosion oriented at an angle of ϕ = 0-60° from the fault normal (Figure 5.9b inset). The pattern is inconsistent with both sliding and tensile crack opening mechanisms. All rock events had rise times of less than 1 μs. This very sudden release of normal force suggests that asperities do not simply slide past each other but fail in a brittle and catastrophic manner such as grain cataclasis during the formation of fault gouge. While consistent with some studies of mining-induced tremor, which found a significant implosive component to the source (McGarr, 1992), the focal mechanism results for the rock samples differ from earlier laboratory friction studies (Yabe et al., 2003; Thompson et al. 2005) that have suggested double-couple type sources. This difference might be due to the low normal stress of the current experiments (~100 kPa) relative to previous studies (typically ~10 MPa), which leads to a reduced spatial density of contacting asperities. Note that the quality of the current recorded signals and the precise modeling of wave propagation effects and instrument response allows the time history and focal mechanism of these sources to be constrained with previously unachievable detail. The implosive sources described here may be due the fracture of individual asperities while the mechanisms described in previous studies are due to the coherent failure of many neighboring asperities.

5.3.1.2 PMMA/PMMA

Asperity rupture on the PMMA/PMMA interface releases only shear force and produces a stress wave radiation pattern which is consistent with the double couple source commonly found in seismic studies. It is at first surprising to find that the plastic events are more reminiscent of natural earthquakes than the rock. While the specimens of both materials were roughened in similar ways and subjected to similar stresses, the plastic has a significantly lower indentation hardness than the rock (see Table 5.2), which affects asperity size and distribution. When normalized to the hardness of the material, even the low normal stress of the current experiments can produce an asperity population similar to that of many MPa in rock. Events studied from the PMMA/PMMA interface could be due to the coherent rupture of many micrometer-sized asperities, all located within the ~1 mm spatial resolution of the point source analysis. The coherent rupture of asperity populations spanning larger areas could be the source of the lower frequency signals observed only for the PMMA.

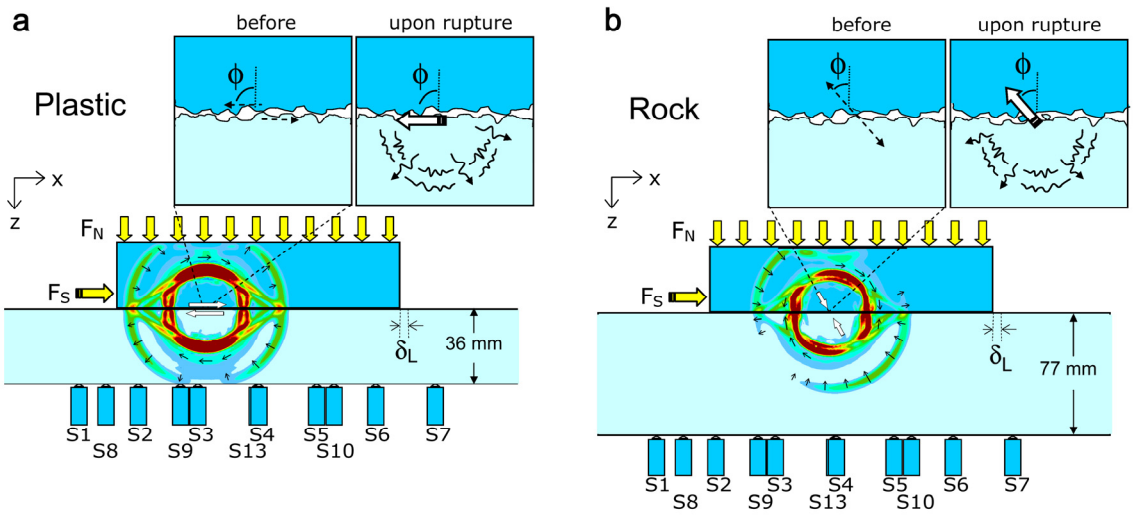

Figure 5.9. Schematic diagrams of source radiation patterns and associated micromechanical models of asperity failure. Dashed arrows represent the effectively static resisting forces which prevent the block from sliding. When the asperity ruptures, a very rapid reorganization of stress occurs. The white arrow represents the force felt by the base plate when the asperity ruptures which results in the high frequency stress wave radiation pattern shown in Figure 5.10. **a**, On the plastic, asperity rupture causes a rapid release of shear force, but the total normal force carried by the asperity is not rapidly changed. **b**, For rock, asperity rupture relieves both shear and normal force in a unidirectional implosion indicative of brittle failure of the asperity.

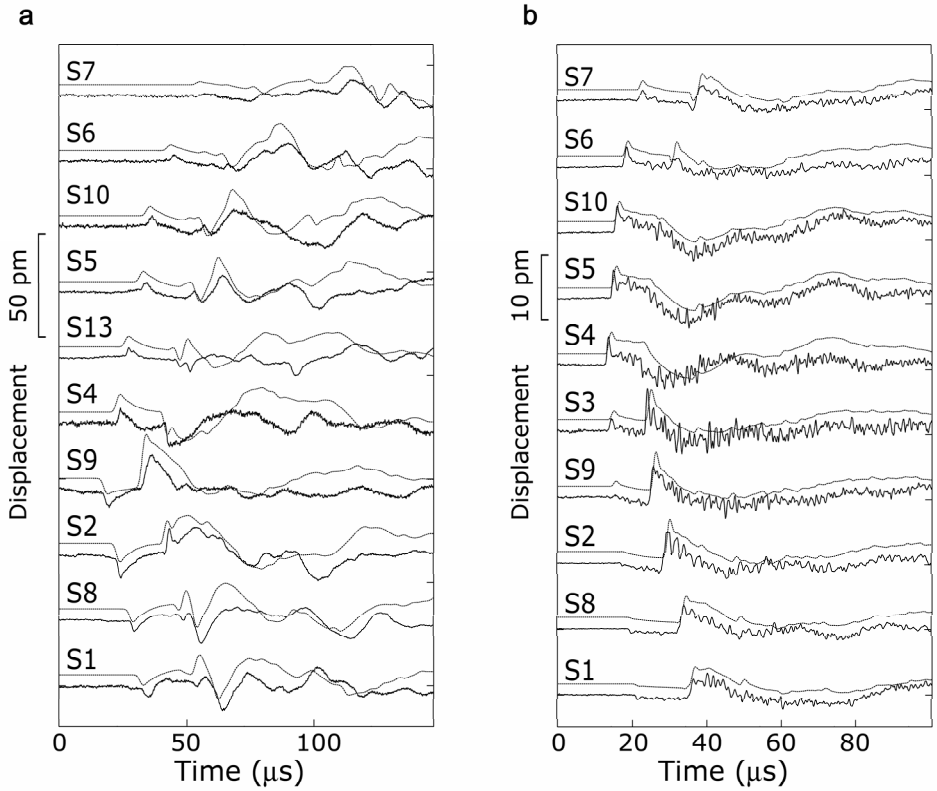

Figure 5.10. Comparison between recorded signals and synthetic seismograms (thin, dashed lines) calculated from models and sensor/source locations shown in Figure 5.9. **a**, A typical event on PMMA/PMMA interface. **b**, A typical event on rock/rock interface.

5.3.1.3 Comparison between rock and plastic focal mechanisms

In Figure 5.10, synthetic seismograms (thin lines) calculated from the models described above, and depicted in Figure 5.9, are shown alongside recorded signals. The recorded signals shown in Figure 5.10 are from well constrained example events with good signal-to-noise ratio, but their mechanisms are representative of *all* of the high frequency (>100 kHz) events analyzed under the variety of conditions tested. The differences in the focal mechanisms are believed to be material dependent rather than due to variation in experimental technique.

For both the plastic and rock, recorded P- and S-wave arrivals are step shaped (though the 20 kHz high-pass filtering causes them to appear somewhat like pulses in Figure 5.10), therefore f(t) is a step. This time history means that, for both materials, the events are due to a sudden release of force (~1-100 mN). For the events described in Figure 5.10, the source time function, f(t), is modeled as a step function of amplitude 90 mN and rise time 500 ns for the rock event and 50 mN/3 μs for PMMA event.

Material	μ (GPa)	H_I (GPa)	T_m (˚C)
Academy Black granite	27[a]	4-6[b]	750-1400[b]
PMMA	2.3[a]	0.3-0.5[c]	160[d]

Table 5.2. Shear modulus, indentation hardness, and melting temperature of the two materials tested.
[a]Estimated from measurements of shear wave velocity
[b]Spray (2010)
[c]Dieterich and Kilgore (1994)
[d]Smith and Hashemi (2006)

There is a substantial difference in melting temperature between rock and PMMA. Flash heating of asperity contacts has been suggested as a mechanism for dynamic fault weakening behavior (Rice, 2006; Beeler et al., 2008). It has recently been suggested that PMMA asperities melt, or at least thermally weaken, during shear (Ben-David, 2010), and this weakening could be responsible for the similarity between the fault mechanisms observed from the plastic and fault behavior commonly observed in the field.

The rock samples produced high frequency asperity rupture events throughout slip. No differences were observed between in asperity rupture events occurring at the initiation of slip and the cessation of slip. All events studied had the same "unidirectional implosion" signature indicative of brittle failure. This suggests that under the current temperatures and pressures, rock asperities did not melt.

In contrast, on the PMMA/PMMA interface, all of the high frequency events are produced during the initiation of sliding. In fact, as shown in Figure 5.5, the majority of all seismic energy recorded (both high frequency and low frequency) was coincident with initiation and not with peak sliding velocity. This suggests that high frequency seismic radiation is primarily produced during the initial rupture of asperities, and that the fault continues to slide, perhaps with melt as a lubricant, without releasing additional high frequency seismic energy.

While it is rarely feasible to perform laboratory tests at confining pressures, loading rates, and temperatures common to natural, seismogenic, faults, this study suggests that informed material selection may be an effective substitute, to reproduce certain aspects of earthquake behavior.

5.3.2 Fault roughness

Measurements of the roughness of exhumed faults indicates that fault roughness evolves, becoming smoother with increasing slip (Sagy et al., 2007; Brodsky et al. 2011). An immature fault may begin its life very rough, but the repeated grinding of the fault during stick-slip cycles can cause the tallest peaks of the surface topography to be worn down. Consequently, an immature fault is thought to be rougher than a mature fault. An open question in earthquake studies is how the seismicity of a fault is affected by its maturity or roughness.

5.3.2.1 Rock

In order to analyze the effects of fault maturity, two sets of tests were performed. For the first set, the rock samples were surface roughened with 36 grit silicon carbide, and a series of stick-slip tests were performed on the samples in this "rough" condition. Next, to create a more mature surface, the sample was forced to slide back and forth hundreds of mm under constant normal load. Given that the typical block displacement from stick-slip instability during testing is 20-50 um, this "wear down" process was equivalent to thousands of stick-slip cycles. Some finely comminuted wear particles (gouge) were produced by this sustained sliding. A second set of tests were then performed on the resulting mature (smoother) interface after the blocks had been worn.

An observable change in the seismicity was identified between the immature and mature interfaces. The largest amplitude events recorded from the mature interface were both smaller and more uniform in amplitude than the largest amplitude events produced by the immature interface. The results shown in Figure 5.5 are from the immature (rough) interface while those of Figure 5.6 are from the mature (smooth) interface (also note a different applied normal force between these two experiments: 400 N for Figure 5.5 and 1200 N for Figure 5.6). It was found that the ratio of signal energy (the area under the voltage-time curve squared) to peak signal amplitude increased for the mature interface relative to the immature one. This statistic, as well as deterministic studies of event distributions, such as that shown in Figure 5.7, indicate that the rupture of the immature interface included a few large amplitude asperity ruptures (> 100 mN) while the rupture of the mature interface consisted of larger numbers of smaller amplitude ruptures (1-40 mN). Despite the changes in the event-size distribution, the focal mechanisms of the individual events (of the hundreds analyzed) did not change. These results are consistent with the conclusion that the events on rock are due to the catastrophic failure of asperities and the formation of fault gauge. Sliding of the immature (rough) interface is resisted by a smaller number of strong asperities, while sliding of the mature (smoothed) interface is resisted by a larger number of weaker asperities.

5.3.2.2 PMMA

The PMMA/PMMA interface produced a much more complicated behavior. For PMMA, the seismic release was not solely composed of a cacophony of high frequency (<100 kHz) events, but also contained low frequency signals. Some evolution of roughness from rough to smooth as a function of slip was observed for the PMMA samples. This was evidenced by visible signs of wear on the interface (slip tended to polish the interface in certain spots). Sometimes, a decrease in the high frequency events was observed, but the effect of surface roughness

evolution on recorded signals was minimal compared to other factors such as loading rate and healing times, as described below. Generally, the rupture of rough samples (roughened with 40 grit sandpaper) tended to produce a number of distinct high frequency events which were riding on top of the low frequency signals, while the rupture of interfaces composed of more smooth samples (600 grit) often showed a complete lack of high frequency events and only produced low frequency signals, but these effects warrant further study.

5.3.3 Fault healing

The static frictional strength of the interface was observed to increase with increasing healing time (time in stationary contact) for both PMMA and rock. The general effect of increased shear strength with increasing healing time is shown in Figure 5.11.

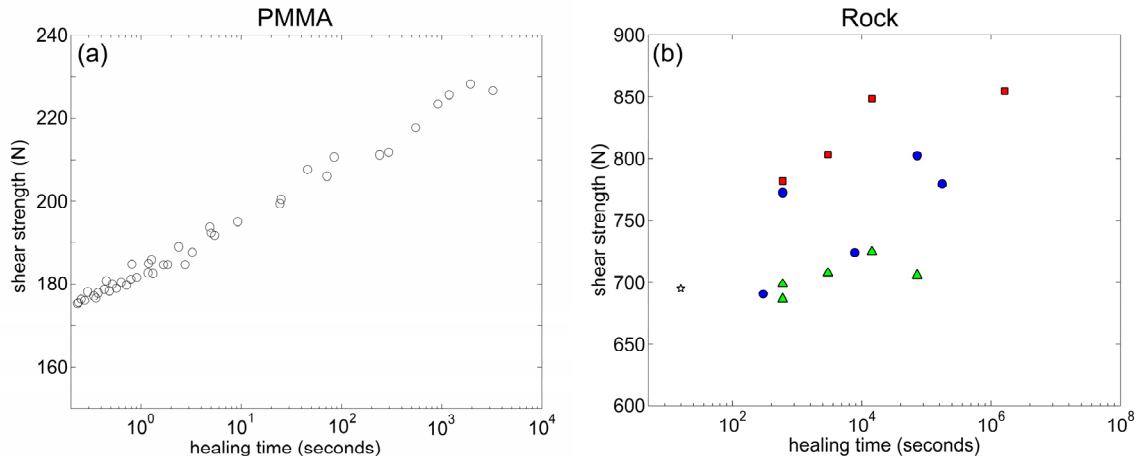

Figure 5.11 The general increase in shear strength with increasing healing time. Each symbol corresponds to one stick-slip instability. The shear force at which the instability occurred is plotted against the time since the previous stick slip instability. For the PMMA, a rapid strengthening with healing time is observed even for healing times less than 1 second. For the rock, The results are a bit more scattered, but still show a general increase in strength with increased healing time.

For the rock, an increase in healing time increased sliding velocity, but had no other effect on the characteristics of recorded signals.

For the PMMA, healing time had a marked effect on the recorded signals. It was found that the rupture of an interface which has healed produces more high frequency stress waves upon rupture than one which has had less time to heal. A particularly illustrative example of this phenomenon is shown through a discussion or Figures 5.12 to 5.14. For this case study, the PMMA slider block (181 mm by 60 mm by 17 mm in the x, y, and z directions) was pressed into a PMMA base plate (450 mm by 300 mm by 36 mm) with a normal stress of 18 kPa. The slider block was loaded in shear at a rate of ~1-4 N/s and allowed to slip in a sequence of five stick-slip instabilities, denoted D1-D5. The five slips occurred at times t = 9.77, 21.12, 32.62, and 45.53, and 79.32 sec, thus the healing times of slips S2-S5 were 11.35, 11.50, 12.91, and 33.79 sec. Measurements of the shear force and slip, for 80 ms surrounding slips S2-S5, are shown in Figure 5.12. The duration of sliding (found to be largely dependent on the compliance of the loading apparatus) is about 5 ms for all five events. As expected, D5, which was allowed to age close to three times as much as the previous three slips, shows a higher frictional strength, larger stress drop, and larger total slip.

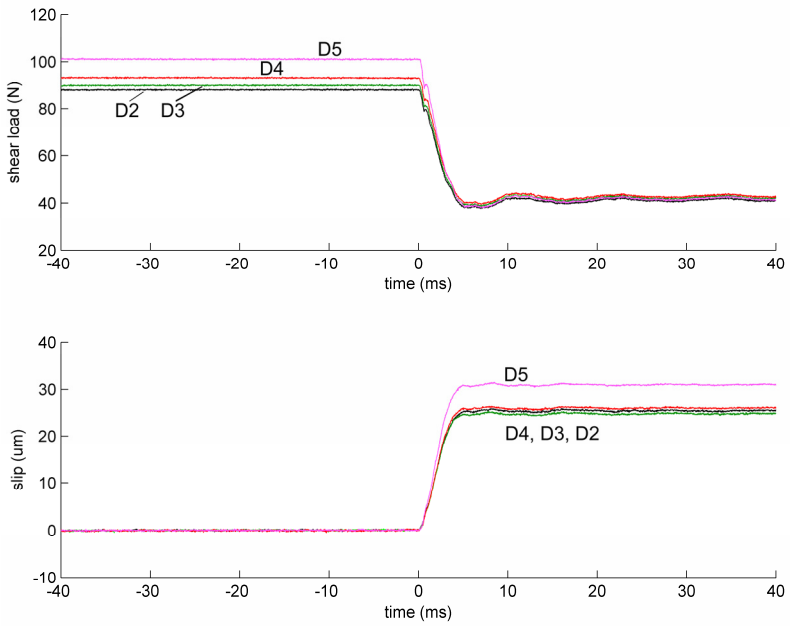

Figure 5.12 Shear load F_s and slip recorded for 80 ms surrounding slip events S2-S5.

Radiated stress waves, recorded with the nanoseismic sensor array located underneath the frictional interface are shown in Figures 5.13 and 5.14. Figure 5.13 shows recordings obtained from sensor S2 in a 3 ms time window surrounding slip instabilities D2-D5. The same four signals are shown in Figure 5.13b high-passed at 250 kHz, in order to highlight the high frequency components of each signal. All four slip instabilities D2-D5 produced similar waveforms, but when the interface was aged, more high frequencies were produced.

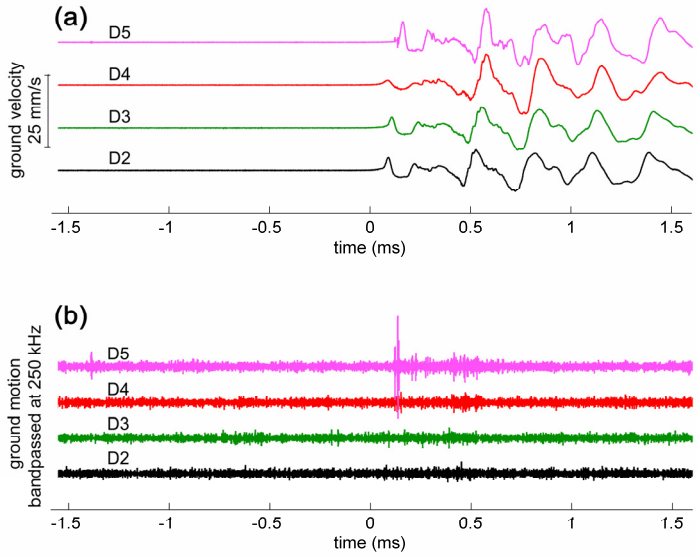

Figure 5.13 (a) Ground velocity recorded by sensor S2 produced by slip events D2-D5. (b) the same signals, high-passed at 250 kHz, highlight differences in high frequency content. [flip the sign of these signsl]

A more detailed examination of the effects of aging on stress wave recordings is made by examining the output of many sensors in the nanoseismic array. Figure 5.14 compares

waveforms recorded by six different sensors in the array during 300 μs time windows surrounding the initiation of sliding for slip instabilities D3 (aged 11.50 s) and D5 (aged 33.79 s). For both slip instabilities, the source of the stress waves is located between sensors S2 and S3. The low frequency components of the waveforms recorded from slip instabilities D3 and D5 are remarkably similar, but the tiny high frequency bursts riding on top of the low frequency signal are much stronger for the rupture of the aged fault (D5) compared to the rupture of the unaged fault (D3).

To facilitate the study of the small-amplitude, high-frequency stress wave arrivals riding on top of the large amplitude low frequency signals, the sensor outputs were split prior to digitization, and one copy of each channel was sent through 20 kHz high-pass analogue filters and amplified 42 dB. The high pass filtering reduces the large amplitude low frequency part of the signal which allows the remaining high frequency signal to be amplified. This more efficiently utilizes the 16 bit dynamic rage of the digitizer, so that the small amplitude high frequency portions of the signals will be better resolved. Figures 5.14c and 5.14d show filtered, pre-amplified, versions of the same signals shown in Figures 5.14a and 5.14b. (Only the waveforms captured prior to signal clipping are shown.) The filtered, pre-amplified signals show that the smooth-looking waveforms of Figure 5.14a are in fact peppered with discrete high frequency wave arrivals, as shown in Figure 5.14c.

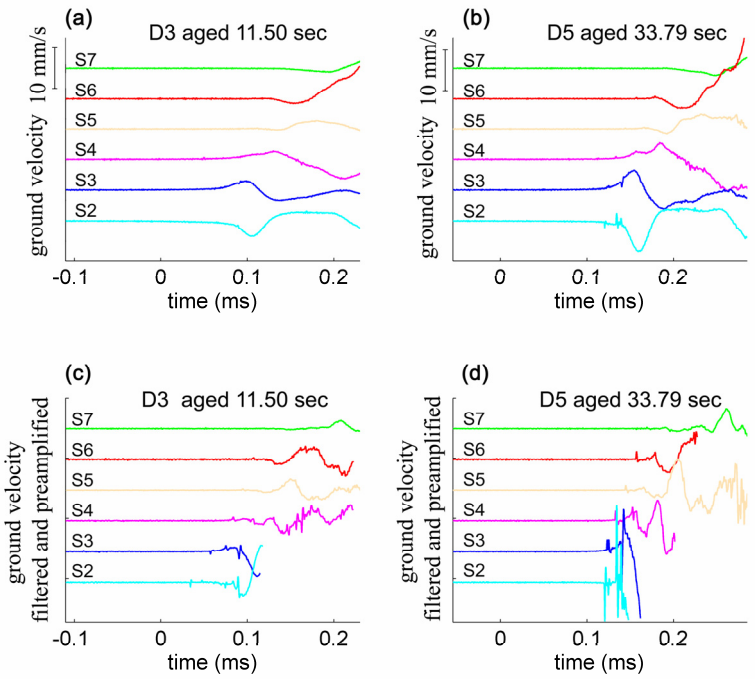

Figure 5.14. (a) Details of rupture initiation recorded by sensors S2-S7 for slip events D3 (aged 11.50 sec) and D5 (aged 33.79 sec). (b) same signals high-pass filtered at 20 kHz and amplified 42 dB.

Seismic radiation recorded from the rupture on the PMMA/PMMA interface often consists of large amplitude low frequency (<100 kHz) waves sometimes punctuated with small amplitude, high frequency (>100kHz) wave arrivals. The high frequency components have rapid wave arrivals, indicative of discrete events, but are often difficult to detect because they are small in amplitude compared to the large low frequency components of the broadband signals. The high frequency signals can be analyzed as point sources via the methods of Section 5.2.4.

When present, the high frequency events recorded from the plastic always had the "release shear force only" focal mechanism described above. This mechanism is distinct from the "unidirectional implosion" focal mechanism which was ubiquitous with the rock samples.

Whereas the low frequency components of the waveforms are very similar between all of the stick-slip instabilities (D2-D5), the high frequency components show larger variations in both amplitude and timing. Under otherwise identical conditions, an aged fault will, in general, produce more discrete high frequency events, but these high frequency events are nearly always preceded by the lower frequency signals. The increase in high frequency events and more modest increase in static shear strength exemplified above was widely observed in the tests on PMMA, but the observation was also complicated by loading rate, surface roughness, and possibly other factors. For example, it was found that the effect of fault healing was quite different if the interface was aged while carrying ~75% critical shear load, (stressed aging) versus those aged while carrying ~20% of critical shear load (non-stressed aging).

5.4 Conclusion

This study illustrates how high fidelity sensing and a calibrated experimental system allow us to better understand the relationship between elastic waves and the underlying mechanics. The quality of the waveforms recorded with this apparatus allows us to confidently image the complex dynamics of frictional sliding. This allows links to be made between measurable material behaviors--e.g. hardness, roughness, healing, etc.--and the generation of (nano)earthquakes.

It is concluded that the rock interface slides as a sustained burst of implosive events with shear components. When the rock samples were worn down to produce a smoother and more mature interface, there was a marked reduction in the peak force held by individual asperities, indicating that that largest (and strongest) asperities were permanently destroyed. This observation, as well as the rapid (<1 μs) release of both shear and normal force during the implosive events, indicates that rock asperities fail in a brittle and catastrophic manner. Finally, the rock continues to produce high frequency events throughout slip, and this produces a remarkably tremor-like signal.

In contrast, the PMMA produces a very rapid burst of seismicity at the initiation of slip, but then continues to slide without radiating high frequency stress waves. Melting of the PMMA asperities may act as a lubricant during this process. Individual high frequency events release only shear force upon rupture and produce seismic signatures more consistent with typical earthquakes. When normalized to the hardness of the material, even the low normal stress of the current experiments will produce a PMMA asperity population similar to that of many MPa in rock, and this could offer an explanation for the similarity between the PMMA events and typical earthquakes.

This comparison suggests that tremor-like signals are produced by the sporadic and incoherent failure of widely-spaced asperities, while earthquakes are typically produced by a more coherent rupture of closely spaced asperities at a high effective stress.

In PMMA, the relationship between surface roughness, fault healing, and the occurrence of high frequency signals riding on top of low frequency signals, suggests that only the asperities which rupture most rapidly and violently produce discrete bursts of seismic energy, while the vast majority of the asperities rupture either more slowly or in a more distributed and incoherent way. Because high frequency events were, in almost all cases, accompanied with or preceded by

low frequency signals, it is unlikely that the rapid rupture of a single, strong asperity triggers the failure of the entire interface. Rather, it is the other way around. The diffuse and incoherent rupture of many weak asperities is what drives discrete and strong asperities to fail rapidly and produce detectable high frequency signals.

High frequency signals, characteristic of discrete sources, were often found buried within a low frequency signal all the way down to the detection limit of the current system, which implies that many rapid events occur but are too small to be detectable. This suggests that the observed low frequency signals are due to the cumulative sum of many small amplitude and rapidly occurring (<1 μs) events. This collection of events collectively releases shear force in what must be a somewhat localized zone (~40 mm)--because the low frequency components of their stress waves all sum up to produce the detectable and somewhat spatially localized low frequency signal--but the collective release of shear force does not typically occur rapidly enough or coherently enough to generate high frequency signals. When the surfaces are rougher and/or the interface has aged longer, the amplitude of high frequency waves is increased, indicating that, under those conditions, some localized patches--perhaps the largest islands with the most uniform strength distribution within the island--fail rapidly enough to produce detectable high frequency signals emanating from discrete (~1 mm) locations.

Chapter 6

Conclusion

The goal of this dissertation has been to obtain a better understanding of stress wave sources. These sources are studied by analyzing recorded signals, but the signals are influenced not only by source characteristics, but also by wave propagation effects and sensor-induced distortions. So that each of those effects could be isolated and characterized, a great deal of work was been spent modeling and implementing known stress wave sources to be used for calibration experiments. Numerous studies were undertaken on six different propagation media: steel, aluminum, glass, concrete, PMMA, and Academy Black granite, and the relative merits of four different types of sensors were analyzed. The sources studied in this work include: ball impact, glass capillary fracture, micro cracking in concrete, and asperity rupture in rock and PMMA.

The foundations of stress wave analysis, including the transfer function approach and underlying assumptions, are established in Chapter 2. In order to validate ball impact as a quantitative source of stress waves, the limits of Hertzian theory are explored in Chapter 3. The study of microcracking in concrete, described in Chapter four, demonstrates the challenges associated with stress wave source characterization in a complicated and imhomogeneous medium. The capstone of this research was the friction study of Chapter 5. Friction remains one of the least understood yet most widely observed physical phenomena. This work showed how the quantitative stress wave methods outlined in the first chapters could be used to enhance our understanding of asperity behavior during stick slip friction, how this information can be used to link material behavior to stress wave production, and how the results may have some direct connections to the generation of earthquakes and seismic tremor. It is hoped that the foundations established in this dissertation will facilitate future research on this topic.

References

Aki, K., Richards, P. G. (1980) *Quantitative Seismology: Theory and Methods* (Freeman, San Francisco), Chapter 2, pp. 9-36.

Baise, L., Glaser, S., Sugano, T. (2001) Consistency of dynamic site response at port island, *Earthq. Eng Struct. Dyn.* 2001; 30: 803-818.

Banerjee, S., Ricci, F., Monaco, E., Mal, A. (2007) Autonomous impact damage monitoring in a stiffened composite panel, *Journal of Intelligent Material Systems and Structures* 18:623–633.

Beeler, N., T. Tullis, and D. Goldsby (2008) Constitutive relationships and physical basis of fault strength due to flash heating, *J. Geophys. Res.* 113, B01401.

Ben-David, O., Rubinstein, S., and Fineberg, J. (2010) Slip-stick and the evolution of frictional strength, *Nature* 463, 76-79.

Bernstein, A. (1977) Listening to the coefficient of restitution, *Am. J. Phys.* 45 (1) 41-44.

Berthoud, P., Baumberger, T., G'Sell, C., and Hiver, J.-M. (1999) Physical analysis of the state- and rate-dependent friction law: Static friction, *Physical Rev. B* 59, 14313-14327.

Bisschop, J. (2002) *Drying Shrinkage Microcracking in Cement-Based Materials*, Delft University Press, 2002.

Bisschop, J., and van Mier, J. (2002) Effect of Aggregates on Drying Shrinkage Microcracking in Cement-Based Composites, *Materials and Structures*, 35, pp. 453-461.

Blum, F., Jarzynski, J., and Jacobs, L. (2005), A focused two-dimensional air-coupled ultrasonic array for non-contact generation. *NDT&E International* 38:634–642.

Boltz, E. S. and Fortunko, C. M., (1995) Absolute sensitivity limits of various ultrasonic transducers, in: McAvoy, B. R. (Ed) *Proc. IEEE Ultrasonics Symp. IEEE*, New York. pp. 951-954.

Bowden, F., and Tabor, D. (1964) *The Friction and Lubrication of Solids,* v. 2 (Clarendon, Oxford).

Boyd, A. and Ferraro, C., (2005) Effect of curing and deterioration on stress wave velocities in concrete, *ASCE J. of Materials in Civil Engineering*, 17, 153-158.

Breckenridge, F., Greenspan, M. (1981) Surface-wave displacement: absolute measurements using a capacitive transducer, *J. Acoust. Soc. Am.* 69(4) 1177-1185.

Breckenridge, F., Proctor, T., Hsu, N., Fick, S., Eitzen, D. (1990) Transient sources for acoustic emission work, in: Yamaguchi, K., Takahashi, H., and Niitsuma, H.(Eds.), *Progress in Acoustic Emission V*. The Japanese Society for NDI, Sendai, Japan,. pp. 20-37.

Breckenridge, F., Tscheigg, C., and Greenspan, M. (1975) Acoustic emission: some applications of Lamb's Problem, *J. Acoust. Soc. Am.* 57(3) 626-631.

Brodsky. E., Gilchrist, J., Sagy, A., Collettini, C. (2011) Faults smooth gradually as a function of slip. *Earth Plan. Sci. Lett* 302, 185–193.

Brown, S.R., Scholz, C.H. (1985) Broad bandwidth study of the topography of natural rock surfaces. *J. Geophys. Res.* 90, 12575–12582.

Buttle, D. J., Scruby, C. B. (1990) Characterization of particle impact by quantitative acoustic emission, *Wear* 137, 63-90.

Candela, T., Renard, F., Bouchon, M., Brouste, A., Marsan, D., Schmittbuhl, J., Voisin, C. (2009) Characterization of fault roughness at various scales: implications of three-dimensional high resolution topography measurements. *Pure Appl. Geophys.* 166, 1817–1851.

Ceranoglu, A., Pao, Y. (1981) Propagation of elastic pulses and acoustic emission in a plate, *J. Appl. Mech.: Trans. ASME* 48 125-147.

Chang, C., and Sun, C. T. (1989) Determining transverse impact force on a composite laminate by signal deconvolution, *Exp. Mech.* 29(4) 414-419.

Ching, J., To, A., Glaser, S. (2004) Microseismic source deconvolution: Wiener filter versus minimax, Fourier versus wavelets, and linear versus nonlinear, *J. Acoust. Soc. Am.* 115 (6) 3048-3058.
Crook, A. W. (1952) A study of some impacts between metal bodies by a piezoelectric method, *Proc. R. Soc*. A212 377-390.
Davies, R. M. (1949) The determination of static and dynamic yield stresses using a steel ball, *Proc. R. Soc. A* 197 416-432.
Dieterich, J.H. (1979) Modeling of Rock Friction 1. Experimental Results and Constitutive Equations, *J. Geophys. Res.* 84, 2161-2168.
Dieterich, J., and Kilgore, B. (1994) Direct observations of frictional contacts—new insights for state-dependent properties, *Pure appl. Geophys* 143, 283–302.
Dieterich, J., and Kilgore, B. (1996) Imaging surface contacts: power law contact distributions and contact stresses in quartz, calcite, glass and acrylic plastic, *Tectonophysics* 256, 219-239
Dreger, D., Nadeau, R., Chung, A. (2007), Repeating earthquake finite source models: Strong asperities revealed on the San Andreas Fault, *Geophys. Res. Lett.* 34, L23302.
Eitzen, D., Breckenridge, F. (1987) Acoustic emission sensors and their calibration, in: Miller R, McIntire P, (editors). *Nondestructive Testing Handbook Second Edition Vol. 5: Acoustic Emission Testing.* Columbus, OH: American Society for Nondestructive Testing, pp. 121–132.
Ersen, A., Smith, A., Chotard, T. (2006) Effect of malic and citric acid on the crystallisation of gypsum investigated by coupled acoustic emission and electrical conductivity techniques. *J Mater Sci* 41:7210–7217.
Falcon, E., Laroche, C., Fauve, S., Coste, C. (1998) Behavior of one inelastic ball bouncing repeatedly off the ground, *Eur. Phys. J. B* 3 45-57.
Ge, M., and Hardy, H. R. (1991) *Fifth Conference on Acoustic Emission/Microseismic Activity in Geologic Structures and Materials*, Pennsylvania State University, June 11-13.
Glaser, S., Weiss, G., and Johnson, L., (1998) Body waves recorded inside an elastic half-space by an embedded, wideband velocity sensor, *J. Acoust. Soc. Am.* 104 1404-1412.
Goldsmith, W., (2001). *Impact.* (Dover Publications, New York).
Goldsmith, W., Lyman, P. T. (1960) The penetration of hard-steel spheres into plane metal surfaces, *J. Appl. Mech.* 27 E (4) 717-725.
Graff, K. (1975). *Wave Motion in Elastic Solids* (Oxford University Press, Mineola, NY), Chapter 5 pp. 273-310.
Greenspan, M. (1987). The NBS conical transducer: analysis, *J. Acoust. Soc. Am.* 81(1) 173-183.
Hertz, H. (1882) Über die Berührung fester elastischer Körper (On the vibration of solid elastic bodies), *J. Reine Angew. Mat.* 92, 156–171.
Hsu, N. (1985). "Dynamic Green's functions of an infinite plate – a computer program," Tech. rep., NBSIR 85–3234. National Bureau of Standards. Center for Mfg. Engineering., Gaithersburg, MD. (available through NTIS PB 86-143856/AS)
Hsu, N. (1977) Acoustic Emission Simulator. US Patent No. 4018084 1977.
Hsu, N., and Breckenridge, F. (1981) Characterization of acoustic emission sensors, *Materials Evaluation* 39 60-68.
Hsu N, Simmons J, Hardy S. (1977) An approach to acoustic emission signal analysis--theory and experiment, *Materials Evaluation* 35:100-106.
Hunter, S. C. (1957) Energy absorbed by elastic waves during impact, *J. Mech. Phys. Solids.*, 5, pp.162-171.

Hutchings, I. M. (1977) Strain rate effects in microparticle impact, *J. Phys. D: Appl. Phys.* 10, L179-L184.
Hutchings, I. M. (1979) Energy absorbed by elastic waves during plastic impact, *J. Phys. D: Appl. Phys*. 12, 1819-1824.
Idrissi H., Limam A. (2003) Study and characterization by acoustic emission and electrochemical measurements of concrete deterioration caused by reinforcement steel corrosion, *NDT&E Int.* 36:563–569.
Johnson, K. (1985) *Contact Mechanics* (Cambridge University Press, Cambridge), pp. 351-369.
Johnson, K. and Greenwood, J. (1997) An adhesion map for the contact of elastic spheres, *J. of Colloid and Interface Sci.* 192 326-333.
Johnson, L. R. (1974) Green's Function for Lamb's Problem," Geophys. J. R. astro. Soc. 37 99-131.
Johnson, L. R. (2010) An earthquake model with interacting asperities *Geophys. J. Int.* 182, 1339–1373.
Johnson, L. R., and Nadeau, R. M. (2002), Asperity model of an earthquake: Static problem, *Bull. Seismol. Soc. Am.*, 92, 672–686.
Johnson, L. R., and Nadeau, R. M. (2005), Asperity model of an earthquake: Dynamic problem, *Bull. Seismol. Soc. Am.* 95, 75-108.
Kappatos V., Dermata E. (2009) Feature selection for robust classification of crack and drop signals. *Structural Health Monitoring* 8:59-70.
Karner, S. L., and C. Marone (2000), Effects of loading rate and normal stress on stress drop and stick-slip recurrence interval, in: *Geocomplexity and the Physics of Earthquakes*, Geophys. Monogr. Ser., vol. 120, edited by J. B. Rundle, D. Turcotte, and W. Klein, pp. 187 – 198, AGU, Washington, D. C.
Kawakatsu, H. (1989) Centroid single force inversion of seismic waves generated by landslides. *J. Geophys. Res.* 94 12,363-12,374.
Knopoff, L. (1958) Surface motions of a thick plate, *J. Appl. Phys.* 29(4) 661-670.
Kim, K. Y., and Sachse, W. (1986) Characteristics of an acoustic emission source from a thermal crack in glass, *Int. J. Fracture,* 31, pp. 211-231.
Landis, E., and Shah, S. (1995) Frequency-dependent stress wave attenuation in cement-based materials, *Journal of Engineering Mechanics* 121 737–743.
Lange, Y., and Ustinov, E. (1983) Acoustic pulses excited by impacts on objects – their analytical representation and spectra, *Soviet J. Nondest. Test.* 105(3) 825-830.
Lifshitz, J. M., Kolsky, H. (1964) Some experiments on anelastic rebound, *J. Mech. Phys. Solids.* 12 (1) 35-43.
Ljung L. (1987) *System Identification: Theory for the User*. (Prentice-Hall, Englewood Cliffs, New Jersey)
Ljung L. (2006) *System identification toolbox, for use with Matlab.* (The Mathworks Inc. Natick, MA)
Love, A. E. H. (1927) *A treatise on the mathematical theory of elasticity* (Cambridge Univeristy Press, London) Chapter 8 pp. 184-203.
Lykotrafitis, G., Rosakis, A. J., and Ravichandran, G. (2006) Self-healing pulse-like shear ruptures in the laboratory, *Science* 313, 1765–1768.
Mahajan, A., and Walworth, M., (2001) 3-D position sensing using the differences in the time-of-flights from a wave source to various receivers, *IEEE Transactions on Robotics and Automation*, 17 91-94.

Mair, K., Marone, C, and Young, P. (2007) Rate Dependence of Acoustic Emissions Generated during Shear of Simulated Fault Gouge. *Bull. Seismol. Soc. Am*. 97, 1841–1849.
Marone, C. (1998) Laboratory-derived friction laws and their application to seismic faulting, *Annual Review of Earth and Planetary Sciences* 26, 643–696.
Marple, S., and Lawrence, S. (1987) *Digital Spectral Analysis with Applications*. (Prentice-Hall, Englewood Cliffs, New Jersey).
McGarr, A. (1992) An implosive component in the seismic moment tensor of a mining induced tremor, *Geophys. Res. Lett*. 19 1579-11582.
McLaskey, G., Glaser, S., (2009). High-fidelity conical piezoelectric transducers and finite element models utilized to quantify elastic waves generated from ball collisions, in: M. Tomizuka, C. Yun, V. Giurgiutiu (Eds.), *Proc. SPIE, Sensors and Smart Structures Technologies for Civil, Mechanical, and Aerospace Systems,* vol. 7292, 72920S-1 - 72920S-18.
McLaskey, G., Glaser, S., and Grosse, C. (2010) Beamforming array techniques for acoustic emission monitoring of large concrete structures, *J. Sound Vib.*, 329, 2384-2394.
Michaels, J., (1982) *Fundamentals of deconvolution with applications to ultrasonics and acoustic emission*, M.S. Thesis, Cornell University.
Michaels, J., Michaels, T. E., and Sachse, W. (1981) Applications of deconvolution to acoustic emission signal analysis, *Materials Evaluation.* 39 1032-1036.
Nadeau, R., and McEvilly, T. (1999), Fault slip rates at depth from recurrence intervals of repeating microearthquakes, *Science* 285, 718-721.
Noda, H., Dunham, E., Rice, J. (2009) Earthquake ruptures with thermal weakening and the operation of major faults at low overall stress levels. *J. Geophys. Res.* 114, B07302.
Ohtsu, M., and Ono, K., (1988) AE source location and orientation determination of tensile cracks from surface observation, *NDT International*, 21, 143-150.
Oppenheim A, Schafer R. (1999) *Discrete time signal processing, 2nd edition*. (Prentice Hall, New Jersey)
Pekeris, C. L. (1955) The seismic surface pulse, *Proc. Natl. Acad. Sci.* 41 469-480.
Peng, Z., Vidale, J. E., Marone, C., and Rubin, A. (2005), Systematic variations in recurrence interval and moment of repeating aftershocks, *Geophys. Res. Lett.* 32, L15301.
Persson, B (1998), Sliding Friction. Springer: Berlin.
Persson, B., Albohr, O., Tartaglino, U., Volokitin, A., and Tosatti, E. (2005) On the nature of surface roughness with application to contact mechanics, sealing, rubber friction and adhesion, *J. Phys.: Condens. Matter.* 17, R1.
Proctor, T. M. (1982) An improved piezoelectric acoustic emission transducer, *J. Acoust. Soc. Am.* 71 1163-1168.
Prosser, W., Gorman, M., Humes, D. (1999) Acoustic emission signals in thin plates produced by impact damage. *J. Acoustic Emission*, 17:29-36.
Putelat, T., Dawes, J., Willis, J., (2011) On the microphysical foundations of rate-and-state friction, *J. Mech. Phys. Sol.* 59, 1062–1075.
Rabinowicz, E., (1965). *Friction and Wear of Materials* (John Wiley, New York).
Reed, J. (1985). Energy losses due to elastic wave propagation during an elastic impact, *J. Phys. D: Appl. Phys.* 18, 2329-2337.
Renard, F., Voisin, C., Marsan, D., Schmittbuhl, J. (2006) High resolution 3D laser scanner measurements of a strike–slip fault quantify its morphological anisotropy at all scales. *Geophys. Res. Lett.* 33, L04305.

Rice, J. (2006), Heating and weakening of faults during earthquake slip. *J. Geophys. Res.* 111, B05311.
Rice, J. and Ruina, A. (1983) Stability of Steady-state Frictional Slipping*, J. Appl. Mech*. 50, 343-349.
Rosakis, A., Samudrala, O., Coker D. (1999) Cracks faster than the shear wave speed *Science* 21, 1337-1340.
Rubinstien, S. M., Cohen, G., and Fineberg, J. (2004) Detachment fronts and the onset of dynamic friction, *Nature* 430, 1005–1006.
Sagy, A., Brodsky, E., Axen, G., (2007). Evolution of fault-surface roughness with slip. *Geology* 35, 283–286.
Salamon, M., and Wiebols, G. (1974) Digital Location of Seismic Events by an Underground Network of Seismometers using the Arrival Times of Compressional Waves, *Rock Mechanics*, 6 141-166.
Sammonds, P., and Ohnaka, M. (1998) Evolution of microseismicity during frictional sliding, *Geophys. Res. Lett*. 25(5) 699–702.
Sansalone, M. J., Street, W. B. (1997) *Impact echo: nondestructive evaluation of concrete and masonry* (Bulbrier Press, Ithaca, NY), Chapter 3, pp. 29-46.
Schaff, D., and Beroza, G. (2004) Coseismic and postseismic velocity changes measured by repeating earthquakes, *J. of Geophs. Res.* 109, B10302.
Schlichting, H. (1979). *Boundary-Layer Theory* seventh edition, McGraw-Hill, USA.
Scholz, C. H. (1990), The mechanics of earthquakes and faulting, (Cambridge University Press, New York).
Shumway R., Stoffer D. (2006) *Time series analysis and its applications*. (Springer, New York).
Scruby, C., Stacey, K., Baldwin, K. G. (1986) Defect characterization in three dimensions by acoustic emission, *J. Phys. D* 19 1986, 1597-1612.
Scruby, C., and Drain, L. (1990) Laser ultrasonics: techniques and applications (Taylor & Francis Group, Great Britain).
Shiotani, T., Bisschop, J., and van Mier, J. (2003) Temporal and spatial development of drying shrinkage cracking in cement-based materials, *Engineering Fracture Mechanics*, 70 1509-1525.
Smith, W., Hashemi, J. (2006) *Foundations of Materials Science and Engineering 4th Edition*, (McGraw Hill, New York).
Spray, J. (2010) Frictional melting processes in planetary materials: from hypervelocity impact to earthquakes. *Annu. Rev. Earth Planet. Sci*. 38:221–54.
Stump, B., and Johnson, L. (1977) The determination of source properties by the linear inversion of seismograms, *Bull. Seis. Soc. A.* 67 1489-1502.
Surgeon. M., Wevers. M. (1999) Modal analysis of acoustic emission signals from CFRP laminates. *NDT&E Int.* 32:311–322.
Thompson, B., Young, P. and Lockner. D. (2005), Observations of premonitory acoustic emission and slip nucleation during stick slip experiment in smooth faulted westerly granite, *Geophys. Res. Lett*. 32, L10304.
Tillet, J. P. A. (1954) A study of the impact of spheres on plates, *Proc. R. Soc. B* 69 677-688.
To, A., Glaser, S. (2005) Full waveform inversion of a 3-D source inside an artificial rock, *J. Sound Vib.* 285, 835-857.
Uomoto, T., Kato, H., (1990) Drying Shrinkage of Concrete and Acoustic Emission, in: *Progress in Acoustic Emission V*, Eds: Yamaguchi, K., Takahashi, H., and Niitsuma, H., The Japanese Society for NDI, Sendai, Japan, pp. 325-330.

Vidale, J. E., Ellsworth, W. L., Cole, A., and Marone, C. (1994) Variations in rupture process with recurrence interval in a repeated small earthquake, *Nature*, 368, 624–626.
Vidale, J. E., and Li, Y.-G. (2003) Damage to the shallow Landers fault from the nearby Hector Mine earthquake, *Nature*, 421, 524– 526.
Weaver R, Lobkis O. (2003) Elastic wave thermal fluctuations, ultrasonic waveforms by correlation of thermal phonons. *J. Acoust. Soc. Am.* 113:2611-2621
White J. (1965) *Seismic Waves: Radiation, Transmission, and Attenuation*. (McGraw-Hill, New York).
Xia, K, Rosakis, A., and Kanamori, H. (2004) Laboratory earthquakes: the sub-Rayleigh-to-supershear rupture transition, *Science* 303, 1859.
Yabe, Y. (2008) Evolution of source characteristics of AE events during frictional sliding, *Earth Planets Space* 60, e5–e8.
Yabe, Y., Kato, N., Yamamoto, K., and Hirasawa, T. (2003) Effect of sliding rate on the activity of acoustic emission during stable sliding, *Pure appl. Geophys* 160, 1163–1189.
Yilmaz, O. (1987) *Seismic data processing* (Society of Exploration Geophysicists, Tulsa, OK), Chapter 2, pp. 82-153.
Zener, C. (1941) The intrinsic inelasticity of large plates, *Phys. Rev. L.* 59, 669-673.
Zigone, D., Voisin, C., Larose, E., Renard, F., Campillo, M. (2011) Slip acceleration generates seismic tremor like signals in friction experiments, *Geophys. Res. Lett*. 38, L01315.